

NUMERICAL SIMULATION OF HYDRO-THERMO-MECHANICAL BEHAVIOR  
OF CONCRETE STRUCTURES EXPOSED TO ELEVATED TEMPERATURES

By

JAE HYEON CHUNG

A DISSERTATION PRESENTED TO THE GRADUATE SCHOOL  
OF THE UNIVERSITY OF FLORIDA IN PARTIAL FULFILLMENT OF THE  
REQUIREMENTS FOR THE DEGREE OF  
DOCTOR OF PHILOSOPHY

UNIVERSITY OF FLORIDA

2003

Copyright 2003

By

Jae Hyeon Chung

## ACKNOWLEDGEMENTS

Praise be to God who endowed me with circumstances to begin and end this work.

I would like to thank to my adviser, Dr. Gary R. Consolazio for his sincere guidance during the course of this work. Without his conscientious advice and hearty help, completion of this work would not have been accomplished. Most of all, I sincerely appreciate his mentorship and friendship that enabled me to stand up throughout every difficult moment of the last five years.

Also, I would like to express my gratitude to the members of the supervisory committee; Dr. Kurtis R. Gurley for his cheerful encouragement, Dr. Michael C. McVay for his academic advice and suggestions, Dr. Marc I. Hoit for his friendly assistance, and Dr. Loc Vu-Quoc for his creative suggestions.

The assistance and guidance of Dr. Joseph W. Tedesco are sincerely appreciated.

Others deserving of thanks are Mr. Anthony J. Murphy and Mr. William A. Yanko. Their constant friendship and encouragement helped in aiding the successful completion of this research from many aspects.

Finally, I would like to dedicate this dissertation to my mother for her patience, moral support, and endless love without which this work would not have been successful.

## TABLE OF CONTENTS

	<u>Page</u>
ACKNOWLEDGEMENTS .....	iii
ABSTRACT .....	vii
CHAPTER	
1 INTRODUCTION .....	1
1.1 Material Response of Concrete to Heating .....	3
1.2 Failure Mechanisms of Concrete at Elevated Temperatures .....	4
1.3 Two Hypotheses in Analysis of Spalling .....	5
1.4 Moisture Clog Spalling .....	7
1.5 Overview of the Dissertation .....	8
2 LITERATURE REVIEW .....	11
2.1 Relevant Flow Parameters .....	12
2.2 Material Characteristics of High Strength vs. Normal Strength Concrete .....	16
2.3 Material Properties of Heated Concrete .....	18
2.4 Heat and Mass Transport Phenomena in Heated Concrete .....	19
2.5 Stress Analysis of Concrete Exposed to Fire .....	20
3. MACROSCOPIC DESCRIPTION OF TRANSPORT PHENOMENA IN HEATED CONCRETE .....	21
3.1 Concrete as a Porous Medium .....	21
3.2 Averaging Principles .....	23
3.2.1 Volume averaging process .....	24
3.2.2 The size of an REV .....	26
3.2.3 Mathematical representation of the averaged porosity .....	29
3.3 Balance Laws for Continua .....	31
3.3.1 Governing differential equations for microscopic conserved quantities .....	33
3.3.2 Governing differential equations for multi-phase continua .....	36
3.4 Macroscopic Mass Balance Law for a Multiphase Mixture .....	38
3.4.1 The mass balance law for the solid phase .....	38
3.4.2 The mass balance law for the fluid phases .....	39
3.4.4 Species mass balance in the gaseous phase .....	40

3.5 Macroscopic Linear Momentum Balance Law for a Multiphase Mixture .....	43
3.5.1 The linear momentum balance law for the solid phase.....	43
3.5.2 The linear momentum balance law for the fluid phases .....	44
3.5.3 The linear momentum balance law for the multiphase medium.....	45
3.6 Macroscopic Energy Balance Law for a Multiphase Mixture .....	46
3.7 Constitutive Equations .....	48
3.7.1 Flow equations in porous media .....	50
3.7.2 Deviation from Darcy' law .....	51
3.7.3 Liquid permeability.....	53
3.7.4 Multi-fluid flow equation.....	55
3.7.5 Mass density of water .....	57
3.7.6 The ideal gas law .....	58
3.7.7 Fick's law for diffusion.....	59
3.7.8 Fourier's law .....	61
3.7.9 Sorption isotherms .....	61
3.7.10 Total stress and effective stress in the solid phase.....	63
3.8 Physical Approximations and Field Equations.....	64
3.8.1 Continuity equation for the fluid phases .....	64
3.8.2 Enthalpy balance equation for the multiphase medium.....	69
3.9 Initial and Boundary Conditions.....	73
 4. NUMERICAL MODELING OF TRANSPORT PHENOMENA IN REINFORCED CONCRETE EXPOSED TO ELEVATED TEMPERATURES.....	 77
4.1 Overview .....	77
4.2 Governing Equations .....	79
4.3 Discretization of Integrated Finite Difference Method.....	82
4.4 Key Parameters of Fluid and Heat Flow in Concrete .....	85
4.4.1 Relative permeability of concrete .....	85
4.4.2 Slip flow constant of concrete.....	91
4.4.3 Volume-averaged quantities for thermal properties of concrete.....	93
4.5 Calculation of Initial Conditions.....	95
4.6 Comparison of Numerical Results with Experimental Data.....	97
4.7 Finite Difference Simulation.....	101
4.7.1 Modeling boundary conditions .....	101
4.7.2 2-D simulation results .....	102
4.7.3 Comparison of 2-D simulations modeled by various fire conditions .....	105
4.7.4 3-D simulation results .....	107

5. FINITE ELEMENT STRESS ANALYSIS OF A REINFORCED HIGH-STRENGTH CONCRETE COLUMN IN SEVERE FIRES.....	113
5.1 Goals and Scope.....	113
5.2 Governing Differential Equations for the Mass and Energy Balance.....	115
5.3 The Coupled Heat Conduction Equation.....	116
5.4 The Principle of Stress Superposition.....	117
5.5 2-D Axisymmetric Finite Element Stress Analysis.....	121
5.5.1 Initial and boundary conditions.....	121
5.5.2 Axisymmetric finite element modeling.....	122
5.5.3 Simulation results.....	125
5.6 3-D Finite Displacement/Temperature Mixed Formulations.....	127
5.7 Discretization of the Transient Heat Conduction Equation.....	134
5.8 27/8 Finite Element.....	139
5.9 Solution Approach.....	141
5.10 3-D Finite Element Thermoelastic Stress Analysis.....	145
5.10.1 Model description.....	145
5.10.2 Modeling of the transient thermal loading condition.....	148
5.10.3 Simulation results.....	149
5.10.4 Summary.....	156
6. CONTRIBUTION OF PORE PRESSURE AND THERMAL GRADIENT STRESS TO SPALLING.....	163
6.1 Factors Influencing Spalling at Early Stages of Heating.....	163
6.2 Contribution of Pore Pressure at a Later Stage of Heating.....	165
7. CONCLUSION.....	171
7.1 Thermal Spalling of Concrete.....	172
7.2 Future Research Work.....	175
LIST OF REFERENCES.....	177
BIOGRAPHICAL SKETCH.....	185

Abstract of Dissertation Presented to the Graduate School  
Of the University of Florida in Partial Fulfillment of the  
Requirements for the Degree of Doctor of Philosophy

NUMERICAL SIMULATION OF HYDRO-THERMO-MECHANICAL BEHAVIOR  
OF CONCRETE STRUCTURES EXPOSED TO ELEVATED TEMPERATURES

By

Jae Hyeon Chung

August 2003

Chair: Dr. Gary R. Consolazio

Cochair: Dr. Kurtis R. Gurley

Major Department: Civil and Coastal Engineering

In this study, thermal spalling of high-strength concrete structural elements has been investigated by developing numerical models capable of analyzing the combined effects of mass and heat transfer phenomena on thermally induced stresses. Through the use of finite difference simulations, this study investigates moisture effects on thermodynamic states of concrete at elevated temperatures and the influence of pore pressure on development of thermal stress induced by temperature gradients. A finite element stress analysis model is combined with finite difference simulations to predict stress states capable of inducing spalling of the type that has been observed both in the field and in laboratory fire testing of concrete structural elements. The combined hydro-thermo-mechanical analysis procedure presented here may eventually serve as a critical

component of stress analysis used for evaluating the fire resistance of high-strength concrete structural systems.

The model of concrete exposed to fire that is developed herein involves mass and heat transport phenomena in a multi-phase continuum. Simultaneous flow of multiple fluid phases (i.e., liquid and gaseous) is modeled using newly proposed constitutive relationships that are considered more accurate than those previously available in terms of assessment of thermodynamic state variables of concrete system. In addition, numerical simulations are used to explore the effects that steel reinforcing bars have on internal temperature and pressure within concrete members.

Pore pressure and temperature time histories from hydro-thermal finite difference simulations are presented and discussed. Results from the simulations yield an improved understanding of the thermodynamic state variables such as pore pressure, temperature, and degree of liquid water saturation. Selection of constitutive models to describe the flow characteristics of concrete and the procedures implemented for the creation of the concrete models are also discussed. Modeling aspects such as meshing techniques, selection of initial conditions, and definition of boundary conditions are discussed. The modeling techniques used to represent radiant heat flux boundary conditions and volume-averaging processes are explained in detail.

Finally, a theory of stress superposition is developed and subsequently used to evaluate stress states so as to determine the controlling contributor to thermal spalling of



high-strength concrete, e.g., hydrostatic pore-pressures and thermal gradient stresses, under extreme thermal loading conditions.

## CHAPTER 1 INTRODUCTION

The thermo-mechanical behavior of concrete structures exposed to high temperature environments has become very important for many engineering problems in recent years. Assessment of the fire resistance of buildings, bridges and tunnels, and assessment of fire damage in structures represent a few example situations. In these areas, many engineers consider understanding the fire resistant characteristics of concrete to be a critical component of accurate structural analysis and thus safe yet economical designs.

Economically, concrete has better fire-resistant properties than other building materials and thus, it provides effective shielding to materials such as steel against serious damage during fires. However, in an extremely rapid heating condition resulting from an elevated temperature environment, sudden explosive material failure of concrete, i.e., spalling, may occur, rendering it incapable of protecting steel reinforcement and structurally unable to carry load.

If a reinforced concrete column in an extreme fire environment undergoes spalling at its surface, then the steel reinforcement can be directly exposed to fire. Strength of the steel at higher temperatures will be progressively reduced. Sudden loss of gross sectional area in the concrete column due to spalling can also result in a reduction of column stiffness. As spalling progresses into deeper regions of the structural member's core, the concrete column may become incapable of carrying the acting loads as severe loss of strength occurs.

The protection of steel beams and girders by a concrete slab is also important in assessing the fire safety of structures. With a fire above the slab, the structural strength of beams can be significantly changed by the fire proofing capability of the slab that provides shielding of the beams against heat.

Fire in a tunnel may cause serious safety problems of structural integrity and thus, economic loss and loss of life. One example case involved a fire in the Eurotunnel. During a fire incidence in the channel tunnel (Ulm et al. 1999a), severe spalling occurred in the tunnel lining. Almost 200 mm deep surface was delaminated and the steel reinforcement lost its 40% yield strength due to heat reaching 1100 °C. Concerned with the possibility of large scale structural damage, the necessity of understanding a potential structural failure mechanism in combination with the material behavior of concrete at high temperatures has been emphasized in the study of tunnel fire incidents.

Thus, the focus of this dissertation is the development of more reliable solution methods to study thermo-mechanical behavior of concrete. The development of an analytical model including the formulation and the application of the finite element method to calculate stress distribution is developed so that the composition of stress produced in concrete structures exposed to fire may be determined. Once such a model has been developed and validated for a reasonable range of applications, it would be used to determine fire safety assessment in existing buildings and develop design guidelines and specifications for the use of concrete in regard to fire safety. Therefore, a numerical tool including material models capable of representing the relevant physical phenomena that occur in heated concrete needs to be developed.

### 1.1 Material Response of Concrete to Heating

Concrete is physically a three-phase material as shown in Figure 1-1. The first phase considered in this study is the solid phase. It consists of the cementitious matrix made of aggregates, hydrated cement, and a bonding interface between the hydrated cement and the aggregates. The second phase includes the liquid phase either in the form of adsorbed water within the solid phase (e.g. chemically bound water in the hydrated cement) or in the form of pore water (e.g. free water or evaporable water in the pores). The gaseous phase (i.e., the mixture of dry air and water vapor) occupying the pores makes up the third phase.

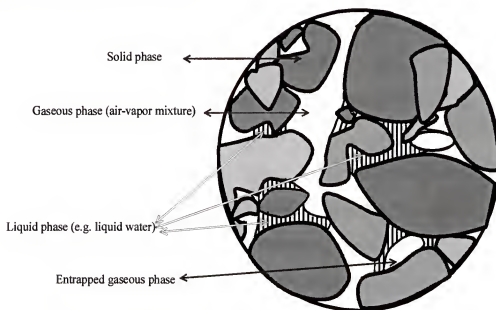


Figure 1-1. A schematic drawing of constituents of concrete

When concrete is exposed to fire, capillary water content evaporates. The generated water vapor migrates along pressure gradients within the concrete matrix toward both the surface of the matrix and deeper into the matrix. As the temperature keeps rising on the exposed surface, desaturation inside the concrete intensifies with

high heat flow, and then, a major portion of the released vapor is driven by a large pressure gradient toward cooler regions. The vapor condenses in the pores of the cooler regions as the pressure buildup levels off. The coupled moisture and heat flow resistance along the flow path increases (i.e., permeability decreases) and the temperature redistribution inside the concrete is affected by the flow (i.e., macroscopic conductivity changes). The multiphase transport and phase change mechanisms of the water content generate a coupled heat and mass transfer phenomenon in the porous medium.

Despite the significant involvement of mass transport phenomena in the temperature distributions that arise, the multi-phase characteristics of concrete have not been emphasized in the literature dealing with heat transfer analysis in concrete. As a result, the coupled heat and mass transport has generally been neglected or simply assumed to be negligible in assessing the temperature gradients and thus computation of thermal gradient stresses.

In this study, the moisture contents and their transport mechanisms occurring in heated concrete are studied and the coupling effects are considered. Thus, thermal gradients stresses, which are suspected as one of the major causes of eventual material failure, are quantified based on the thermal gradients computed by coupled moisture and heat transfer.

## **1.2 Failure Mechanisms of Concrete at Elevated Temperatures**

When concrete structures are exposed to high temperature sources such as fire, material failure associated with rapid heating can occur. The term “spalling” is used to describe the separation of concrete from the surface of a concrete element—such as

columns, beams, slabs and walls—when concrete structural elements are rapidly heated. This material failure can seriously affect fire resistance of a structure and thus structural performance. The separation process can be classified into the following categories:

**Spalling.** This is defined as a violent form of material failure that occurs at an early stage of heating and may result in extensive damage or complete failure of the concrete element.

**Sloughing off.** This is defined as a progressive form of breakdown, which involves gradual separation over longer periods of time of material from the concrete element. It may continue slowly through the later stage of heating.

The severity and sudden failure mechanism of spalling is regarded as being more serious in the assessment of structural safety and thus requires additional attention.

### 1.3 Two Hypotheses in Analysis of Spalling

The causes of spalling have been studied for several decades. Two hypotheses have been proposed to explain explosive spalling. The first hypothesis is that heating produces very high water vapor pressure in the concrete pores (Harmathy 1964), which results in large tensile stresses and consequent tensile failure. In many numerical approaches based on this hypothesis (Sahota and Pagni 1979, Kodres 1996, Tenchev et al. 2001), a microscopic pore pressure buildup was treated as a macroscopic stress component of the heated concrete. With a macroscopically averaging process, contribution of the microscopic thermodynamic pressure can be substantially reduced to an actual stress state that should be used in the determination of potential macroscopic material failure. It has previously been unknown as to

whether pore pressure is a major contributor to spalling. The key material parameters such as *permeability* and *conductivity* of concrete, which determine flows of the fluid phases and which can be determining factors in the coupling effects between heat and moisture flows, have to be carefully chosen in computational analyses.

The second is that sudden localized heating causes thermal expansion, which is restrained by the adjacent cool concrete. This phenomenon produces a large compressive stress, which is suspected to cause crushing of the concrete and buckling of the surface layer. Although high pore pressure develops inside concrete, it only serves to create cracks. Nevertheless, once crack opening starts, the pore pressure is assumed to be dissipated and drop nearly to zero. Furthermore, on the basis of *fracture mechanics*, brittle fracture due to sudden release of the potential energy of the thermal stress has been explained as a major cause to explosive spalling (Bažant 1997) where concrete flaws may act as fracture nuclei. The medium was assumed to be a homogeneous continuum in the sense that the size of a dominant flaw is large in comparison with the characteristic microstructural dimensions of the material constituents. Initiation and the process of material failure of concrete then occur in the influence of applied loads, flaw geometry, size of the structural element and material behavior in crack propagation from the dominant flaw in concrete.

One thing, however, has been unclear as to whether thermal expansion is more dominant a mechanism than thermal gradient effects when coupling effects between heat flow and steam induced by evaporation of the free water affect the temperature distribution. Temperature rise can be significantly different if fluid phases (i.e., liquid and gaseous phases) in concrete pores are included in the analysis of heat transfer. The

role of the fluid phases in development of the stress field, which is possibly interrelated with crack propagation at elevated temperatures, needs to be included. Thus, influence of pore pressure and its effects in cracking of heated concrete should be considered for the relevant thermodynamic state in heated concrete. In this dissertation, pore pressure is examined to determine whether it is a significant contributor to the stress state and to material failure.

#### **1.4 Moisture Clog Spalling**

Spalling has generally been found to be more severe (as observed in actual fires and during laboratory testing of specimens) in high strength concrete (HSC) than in normal strength concrete (NSC) (Sullivan 2001). To investigate a process known as moisture clog spalling (Harmathy 1964), flow of both fluid phases (i.e., liquid and gaseous phases) needs to be studied. The process of vaporization and condensation continues during heating and eventually a “moisture clog”, i.e. a region of significantly increased pore liquid saturation, has the effect of significantly reducing the permeability of the porous matrix to gas (steam) flow. Consequently, the process results in a sharp rise in pore pressure at that location, and induces large differentials of the temperature field of the matrix, which consequentially causes a significant change of the development of temperature gradients. If the resistance of the pore network to moisture flow is overcome by the pressure gradient, the condensed moisture layer begins to move deeper.

In this study, attention is given to this phenomenon that generally has been suspected to be responsible for severe spalling in HSC. Because of the lower permeability of HSC, pore pressure induced by water vaporization is unable to



dissipate quickly. Several factors that affect moisture flow including the permeability, conductivity, porosity, and initial liquid saturation level of concrete will be studied in this dissertation. A more detailed explanation and prediction of pore pressure buildup will be addressed by investigating multi-phase mass flow that nonlinearly couples with heat transfer mechanisms such as internal convection and conduction.

### 1.5 Overview of the Dissertation

The need for more reliable solution methods to study the behavior of the concrete structures exposed to fire has prompted the development of a coupled multi-phase analytical model in the present study. Capable of analyzing the thermally induced stress state under consideration of heat and mass transfer, a computational model forms the basis for this research.

As a parametric study, the first part of this study focuses on the use and modification of an existing finite difference based heat and mass transport simulation code in order to examine pore pressures quantitatively and determine temperature distributions in concrete exposed to fire. In the modeling of moisture movement through concrete, most important among the issues are the development of a new *relative permeability* function for concrete (presented herein) and consideration of the *slippage effect* in gas flow through heated concrete. Because heat and mass transfer in concrete has significant dependence on the relevant material characteristics, particularly on *permeability*, the phenomena such as *relative permeability* and gas slip flow effects need to be considered in determination of thermodynamic state variables such as pore pressure and temperature. In consideration of the fundamental

relationships among these parameters, a numerical solution is sought and compared to experimental tests. Using a finite difference analysis (FDA) model, key field parameters for the modeling are identified.

In the second part of the dissertation, multi-dimensional finite element stress analysis models are developed, which utilize the results obtained from the finite difference analysis. Using the theory of thermodynamics, practical assumptions used in the study are discussed and are validated. Prediction of a combined stress state developed in the heated concrete structural members requires simulation of the structural boundary and thermal loading conditions. Thus, modeling techniques are developed that take into account realistic structural boundary and initial conditions. A mathematical model, which can be applied to a wide variety of three-dimensional configurations of concrete structures such as reinforced concrete walls, slabs, columns and beams under different boundary conditions, will be presented in detail. Further mathematical discussion is made regarding energy balance in a non-isothermal partially saturated porous medium as a starting point for future research activities.

Finally, thermal spalling of structural concrete elements is studied and analyzed by making use of the newly proposed models. Effects of the coupled heat and mass transfer mechanism on the prediction of combined stress states are studied quantitatively. With a better knowledge of the thermodynamic state, thermally induced stresses are then investigated using the theory of elasticity. Therefore, the contribution of the pore pressure buildup to spalling can be identified. In addition, the rate of penetration of the “moisture clog” and the locations of thermodynamic pore-

pressure peaks under different thermal loading conditions are discussed, which can be crucial to understanding material failure mechanisms such as spalling.

## CHAPTER 2 LITERATURE REVIEW

For many years, heat and mass transfer in heated concrete has been investigated both theoretically and experimentally as numerous engineers and scientists have studied material behaviors of porous media at elevated temperatures. Generally, three different approaches to the problem can be observed (Lewis and Schrefler 2000):

**Microscopic level.** “The scale of nonhomogeneity is of the same order of magnitude as the dimensions of a pore or a grain. Therefore, a mathematical point within a single phase and the field variables describing the status of a phase are defined only at the points occupied by that phase” (pp. 10).

**Macroscopic level.** “The real multiphase system that occupies the porous medium domain is replaced by a model at the level of interest of continuum mechanics where a continuous distribution of the constituents through a macroscopic control space is treated using an averaging process” (pp. 10).

**Megascopic level.** “Selected macroscopic nonhomogeneities are eliminated by averaging and/or by using a mathematical model that is stated in a domain, which has fewer dimensions than the real domain (e.g., a two dimensional problem with field-values averaged over the thickness)” (pp.10).

In theory, the governing equations that describe heat and mass transport phenomena in concrete can be written at the microscopic level where only a mathematical point within a considered phase present in the domain is focused on. However, the surface

boundaries of the phases in this type of system description are too complex to be described. The pore structure of concrete has an extremely complicated geometry so that a mechanical description of the problem at the microscopic level is difficult. The state variables (e.g., velocity, pore-pressure in the fluid phase, temperature and stress in the solid skeleton) within a phase vary from point to point.

For engineering purposes, a model at the macroscopic level or above is of interest, where measurable, continuous and differentiable extensive quantities (quantities that can be additive over volumes with mass, momentum and energy) can be determined and boundary value problems can be stated and solved. Such models describe interacting constituents such as the solid, liquid and gaseous phases that occupy the entire control space of the porous medium. The description of concrete as a multiphase system made of those continuous bodies is based on averaging theories of field variables that dictate the state of the system. By using the averaging theory based on spatial averaging processes, macroscopic variables that correspond to real laboratory measurable quantities are used for developing the governing equations.

The main goals of this chapter are to review the continuum approaches used in the past and to lead the readers to the macroscopic level of describing phenomena in mass and heat transfer in porous media. The governing equations of a partially saturated concrete porous medium at elevated temperature are then derived and discussed in the following chapter.

## **2.1 Relevant Flow Properties**

In modeling simultaneous multiphase fluid flows in heated concrete, differences between permeability to gaseous phase and permeability to liquid phase of the

concrete have been overlooked in many past numerical studies (Huang et al. 1979, Sahota and Pagni 1979, Hurst and Ahmed 1998). Significant changes in gas permeability of concrete—when moisture is vaporized and redistributed in elevated temperatures—were not considered in the numerical predictions of pore pressure buildup. Furthermore, gas permeability of concrete was arbitrarily chosen in a few cases of numerical simulations.

*Relative permeability* is a concept that is very important for the simulations considered in this study. It includes macroscopic mathematical measurement describing the multiphase flow of fluids in porous media (Corey et al. 1956, Burdine 1953) and represents the fluid-fluid interactions during multiphase flow (Li and Horne 2001). The relative permeability of a porous network can be thought of as a fraction of the intrinsic permeability for the phase of interest. When two or more phases flow simultaneously inside concrete, each phase will develop its own flow network to which a permeability can be assigned in much the same way as for single-phase flow.

A new relative permeability function for high strength concrete (concrete that has a low water-cement ratio and contains silica fume (or fly ash) and superplasticizer) as well as normal strength concrete (concrete that has a relatively higher water-cement ratio and a compressive strength,  $f'_c$ , of 6000 psi or below) is developed and then implemented as a new function into the TOUGH2 code (Pruess 1991). Reflecting the manner in which flowing fluid phases are distributed within concrete, the idea of relative permeability was adapted to account for the wetting state, pore structure and saturation history of concrete structures during mass and heat

transfer. Due to *moisture clog* formation during mass and heat transfer, flow of the gaseous phase is affected and inhibited. Relative permeability functions written as functions of degree of phase saturation were thus developed. This is a new application for hysteretic constitutive relations governing multiphase flow inside concrete exposed to rapid heating. In a recent literature search, the concept of relative permeability was verified by experimental measurements of gas permeability of partially saturated concrete (Jacobs 1998). Chung and Consolazio (2003) showed that numerical computation of mass flow rate in consideration of fluids' relative interaction inside heated concrete was significantly changed by the relative permeability implementation. Changes in prediction of mass transport and temperature gradient development indicated the importance of the relative permeability concept in modeling coupled mass and heat transfer phenomena in heated concrete. In addition to phase interference modeling, gas phase slip-flow effects are also important in the present context.

The slip flow phenomenon that arises during gas movement in concrete can be quite substantial for low permeability materials (Klinkenberg 1941) such as high strength concrete (HSC). Gas permeability of concrete may vary approximately two orders of magnitude due to the slip effects. Thus, when interpreting data from gas permeability testing of concrete, one must be able to isolate and "remove" the Klinkenberg (slip flow) effects in order to determine the fundamental intrinsic permeability of the concrete.

Experimental studies by McVay and Rish (1995) revealed that slip flow, not laminar flow, occurs when superheated steam and nitrogen gas are passed through

cement mortar. They demonstrated a procedure involving testing at various levels of gas pressure that quantifies the slip flow effect with  $b$  (Klinkenberg's constant) data and evaluates  $K_g$  (the fundamental intrinsic permeability) data for the tested material. For numerical modeling purposes, the parameters  $K_g$  and  $b$  are used for gas flow calculations and the liquid flow parameter  $K_\ell$  (the water permeability) is used to compute liquid flow rates (Bamforth 1987a).

However,  $K_\ell$  has often been treated as being equivalent to  $K_g$ , the fundamental intrinsic permeability of the concrete (Bamforth 1987b). This results in an overestimation of the slip flow phenomenon in gas permeability of concrete. Dhir et al. (1989) conducted experimental tests to identify the relationship between air and water permeability of concrete. They demonstrated that even when the gas slippage and temperature effects are considered in the calculation of the fundamental intrinsic permeability of concrete, the derived intrinsic permeability of concrete could still vary with respect to whether air or water was used in the measurement process. The difference in experimental results from gas and liquid permeability of concrete was also reported by Whiting (1988). The departure from the concept of a single absolute value of concrete permeability is believed to be caused by physical (e.g., dilation of cement hydrates in contact with water) and chemical (e.g., hydration of cement paste) interactions during the long testing periods used in water permeability testing of concrete.

Chung and Consolazio (2003) developed an interpretation method for using experimental data from gas permeability testing of concrete to determine the Klinkenberg constant  $b$  that quantifies just how sensitive the "apparent" gas



permeability of the material is to pressure changes. Emphasis was on properly accounting for slip flow in numerical modeling of mass transport inside heated concrete, particularly HSC (because its lower permeability is more affected by pressure changes than normal strength concrete (NSC)).

## **2.2 Material Characteristics of High Strength vs. Normal Strength Concrete**

Pore structural network characteristics of concrete have generally been suspected to result in the risk of explosive thermal spalling, especially for structural members made of high performance or strength concrete. For example, permeability in HSC is more severely affected by changes of the degree of saturation as the evaporation-condensation process forms *moisture clog*.

Huang et al. (1979) pointed out that the distribution of pore size might be considered the most important parameter affecting moisture transfer in a porous medium. The characteristics of concrete related to the distribution of pore size were identified later by Baroghel-Bouny and Chaussadent (1996). They experimentally verified that classical pore structure investigation methods such as mercury intrusion or nitrogen adsorption were not able to provide accurate pore network characteristics of cement-based materials, particularly for high-performance concrete.

Additional efforts to understand pore structures have focused on using sorption curves to calculate the local equilibrium moisture content (Hansen 1989). Water vapor desorption and adsorption isotherm tests have been conducted for both NSC and HSC. The experimental water vapor sorption isotherms (hydrometrical equilibrium at a constant temperature) showed that more severe material hysteresis in isotherms was observed in HSC. Kjellsen and Atlassi (1999) also investigated

influence of silica fume on the pore structure of mortar, using water vapor sorption isotherms. It was concluded that the characteristics of pore size distribution and the ratio of pore volume to total volume of the concrete specimen were the key to cause such a significant hysteresis in isotherms of HSC. The test results proved that the initial degree of saturation at ambient temperatures and the structural pore-network (i.e., permeability and porosity) of HSC are different from NSC.

These differences are thought to be related to the fact that behavior of saturated HSC subjected to intensive heating has been reported as prone to explosive spalling (Sanjayan and Stocks 1993, Chan et al. 1999). Chan et al. (1999) also showed that moisture content had a dominant influence on spalling, which was concluded to be related to vapor pressure buildup. The dependence of spalling on moisture content and strength of concrete at elevated temperatures was confirmed. However, the effects of the two factors on thermally induced stress, and thus, material failure in a concrete system remained unexplained.

### **2.3 Material Properties of Heated Concrete**

Generally, strength of concrete at elevated temperatures is known to diminish. Many studies have been conducted to determine thermal and mechanical properties of concrete at elevated temperatures for use in fire resistance calculations (Castillo and Durrani 1999, Lie and Kodur 1996, Phan and Carino 1998, Reis et al. 2001, and Janotka and Bágel 2002).

The influence of temperature on the mechanical properties such as compressive strength and modulus of elasticity was claimed to be greater than the influence on thermal properties of thermal conductivity, specific heat and thermal expansion (Lie

and Kodur 1996). Phan and Carino (1998) summarized experimentally tested elastic moduli and compressive strengths of HSC and NSC exposed to rapid heating. In their report, HSC and NSC exhibited differences in the mechanical properties in the temperature range between room temperature and 450 °C and a higher potential of HSC to fail by explosive spalling was noted. Reis et al. (2001) endeavored to measure the reduction of fire resistance of HSC. HSC was found to be more severely affected in its mechanical behavior when exposed to fire. For a remedy to explosive spalling, they suggested that using steel fiber reinforcement could improve the performance of HSC and NSC elements in fire. Janotka and Bágel (2002) conducted experimental tests of thermo-mechanical properties of HSC at temperatures up to 800 °C. The pore structure of HSC was found to change significantly and resulted in strength reduction and permeability increase.

## **2.4 Heat and Mass Transport Phenomena in Heated Concrete**

In a *macroscopic* viewpoint, the theory of irreversible process (*the second law of thermodynamics*) can be used to identify the driving forces, based upon relating the entropy of the porous system to the heat transfer rate, the rate of mass flow and the distribution of temperature and pore pressure (Luikov 1966).

Elevated temperature in the porous system will induce a temperature gradient that causes a pressure gradient (Sahota and Pagni 1979, Huang 1979, Wang and Yu. 1988). Sahota and Pagni (1979) obtained a quasi-static solution of a two-dimensional transient conduction problem with mixed boundary conditions, assuming that property variations and moisture transfer were negligible. Huang (1979) investigated the effects of mass concentration, temperature and pore pressure gradients on energy

and mass transfer. Moisture migration through porous media was assumed to predominantly occur in the gaseous phase driven by pressure and mass concentration gradients. Liquid phase movement was neglected because of its very small Darcy's coefficient (*coefficient of permeability*, also called *hydraulic conductivity*) compared to that of gases. The evaporation-condensation mechanism was concluded to be a governing factor in the drying process (Huang et al. 1979).

Abdel-Rahman and Ahmed (1996) developed a numerical solution method in order to compute the pore pressure fluctuations and the influence of the pore pressure on spalling of concrete at elevated temperatures. Kodres (1996) hypothesized that high pore pressures and pressure gradients developed by vaporized water content and from air being compressed by liquid water could be sufficient to cause a tensile failure in concrete when water and air were migrating through a heated section of concrete. Thermal expansion of liquid pore water and transport of water were also found to affect the build-up of pore gas pressure by Kalifa et al. (2000). Their experiments demonstrated a correlation between pressure peaks and temperature distributions (e.g., a plateau in temperature curves was found where the peak pore pressures developed). The two hypotheses confirmed that (1) a drying front is preceded by a saturated layer acting as moisture clog and (2) flow of fluids in pores affects temperature re-distribution inside the system

## **2.5 Stress analysis of concrete exposed to fire**

For the fire incident that occurred on November 18, 1996 in the Channel Tunnel connecting England and France, Ulm et al. (1999a and b) studied thermal spalling to evaluate the total stress state that might have developed during the fire. In their

hypothesis, the magnitude of the pore pressure buildup may not be large enough to cause tensile failure of concrete. It was believed that the pore pressure would be quickly dissipated (or reduced) with crack opening that would prevent pressure build up. As a result, the pore pressure buildup was claimed as a secondary factor in determination of the spalling mechanism with expansion of a growing crack.

Moisture movement was not considered in the heat transfer analysis. A finite element model (Ulm et al. 1999a) was developed with their newly proposed constitutive model, such as isotropic chemoplastic softening model (Ulm et al. 1999b), for a heated concrete. Their study in brittle fracture due to restrained thermal dilatation concluded that material changes caused by chemical interactions (e.g., dehydration) in the constituents of concrete were more influential than a coupling effect between heat transfer and fluid transport in the thermal stress analysis. Temperature re-distributions induced by the effects of multi-phase interactions of heat transfer were not considered.

Baggio et al. (1995) conducted a computational analysis of mechanical behavior of concrete structures combined with thermo-hygrometric effects of the drying process in ambient temperatures. They emphasized that a thorough understanding of the heat and moisture transfer phenomena occurring inside heated concrete was required to more accurately evaluate thermal and moisture transmission behavior and the related stresses and strains of the porous building material. With an understanding of the influence of the fluid transport mechanisms on heat transfer phenomena, the efforts are extended in the present study to modeling the coupled effects and

analyzing a combined stress state of the heated concrete, which results from both thermo-mechanical stresses and pore pressure.

## CHAPTER 3 MACROSCOPIC DESCRIPTION OF TRANSPORT PHENOMENA IN HEATED CONCRETE

The objective of this chapter is to develop a mathematical model of a multi-phase continuum that describes heat transfer and mass transport phenomena in heated concrete at the macroscopic level. The model consists of balance equations for each extensive quantity (mass, momentum and energy) that is transported, constitutive relations describing the properties of the particular phases involved, source functions of the extensive quantities, and initial and boundary conditions stated at the macroscopic level.

For descriptions of the hydro-thermal behavior of a multiphase porous medium, constitutive models for the constituents are discussed using macroscopic field variables such as permeability and conductivity. For quantitative solution of the practical engineering problems considered in this study, assumptions made in the mathematical model are discussed. Also, constitutive relations employed within governing field laws and source functions for field variables are presented with mathematical derivation of the governing equations. The nature of boundary conditions relating to transport phenomena of the extensive quantities at the macroscopic level is briefly discussed. In the following chapter when a numerical model is presented, additional details of modeling the boundary conditions will be given.

### **3.1 Concrete as a Porous Medium**

A common characteristic of concrete as a porous medium is that the solid phase is

distributed throughout its domain (and thus, also the fluid phases). That is, if sufficiently large samples of the concrete, which are small enough so as to represent a sufficiently close neighborhood around the point of sampling, are taken at different locations within a domain, a solid phase is found in each of them.

Denoting the volume of a sample that satisfies these conditions as a *representative elementary volume* (REV) (shown in Figure 3-1) of the concrete domain at the given point, Bear (1972) and Bear and Bachmat (1998) defined concrete as a multiphase material characterized by the following features

**Representative Elementary Volume (REV).** A representative elementary volume can be determined such that, regardless of where we place it within a concrete domain, it will always contain all the three phases (i.e., the solid, the liquid, and the gaseous phases shown in Figure 3-1). If such REV cannot be found for a given domain, the domain cannot be qualified as a porous medium domain.

**Size of the REV.** The size of the REV is such that parameters that represent the characteristics of the distributions of the void space occupied by the fluid phases and of the solid matrix within it are statistically meaningful. That is, the macroscopic effects of the microscopic configuration of interphase boundaries and the actual variation of extensive quantities (mass, momentum, and energy) within each phase are still retained in the form of coefficients, whose structure and relationship to the statistical properties of the phase can be determined. The numerical values of these coefficients must be experimentally measurable in the laboratory, or in the field.

Therefore, an REV of concrete involves (1) a solid phase of aggregates, hydrated cement and their bonds, (2) a liquid phase of free water in pores and



chemically bound water in the hydrated cement, and (3) a gaseous phase of a mixture of dry air and water vapor.

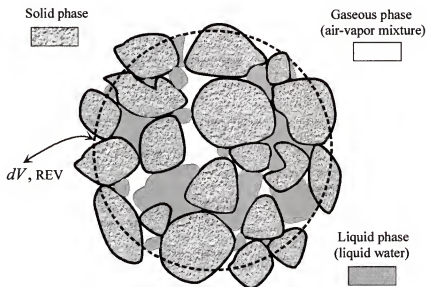


Figure 3-1 An REV occupied by the three phases

As stated earlier, the goal is to describe each phase and its behavior as a continuous body that occupies the entire domain of the system. To achieve this objective, *averaging rules* that transform each of these phases into a continuum are presented in the following section.

### 3.2 Averaging Principles

Having introduced a *representative elementary volume* (REV) as the first step necessary for the process of integrating from the microscopic level to a scale of continuum mechanics, we now review the averaging principles that are crucial for the development.

### 3.2.1 Volume averaging process

First, we choose a point of the concrete system shown in Figure 3-1, assuming that point to be the centroid of averaging volume element denoted by  $dV$  (or an REV). Likewise,  $dV^s$ ,  $dV^w$  and  $dV^g$  will denote the corresponding subdomains and averaging volumes of the solid phase (superscript  $s$ ), the liquid water phase (superscript  $w$ ), and the gaseous phase (superscript  $g$ ), respectively. Thus, the averaging volume  $dV$  is the sum of the volumes occupied by three phases

$$dV = dV^s + dV^w + dV^g \quad (3.1)$$

The position of center of an REV in a global coordinate system is described by position vector  $\mathbf{x}$ . Figure 3-2 shows the position vector denoted by  $\mathbf{x}^{local}$  of a point that is located within a domain  $dV$  centered at  $\mathbf{x}$ . The volume of constituent  $\pi$  within the REV,  $dV^\pi$ , is obtained by introducing a phase distribution function,  $\gamma^\pi$

$$\gamma^\pi(\mathbf{r}) = \begin{cases} 1 & \text{for } \mathbf{r} \in dV^\pi \\ 0 & \text{for } \mathbf{r} \in dV^\zeta \text{ where } \pi \neq \zeta \end{cases} \quad (3.2)$$

Thus

$$dV^\pi(\mathbf{x}) = \int_{dV} \gamma^\pi(\mathbf{r}) dV_m \quad (3.3)$$

where the integration refers to the microscopic volume element  $dV_m$  that its position is described by a vector  $\mathbf{r}$  between the two points where  $\mathbf{r} = \mathbf{x}^{local} - \mathbf{x}$ .

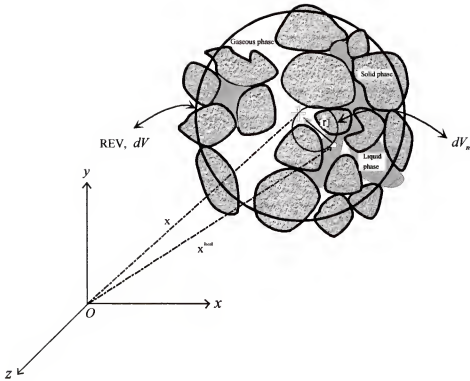


Figure 3-2 Definition of averaging volume element of a porous medium (after Lewis and Schrefler, 2000)

Similarly, the part  $da^\pi$  of area  $da$  of the REV, occupied by the constituent  $\pi$  can be written as

$$da^\pi(x) = \int_{da} \gamma^\pi(r) da_m \quad (3.4)$$

where  $da_m$  is the microscopic area element.

Therefore the *volume fraction* of phase  $\pi$  within the REV becomes

$$\eta^\pi(x) = \frac{dV^\pi}{dV} = \frac{1}{dV} \int_{dV} \gamma^\pi(r) dV_m \quad (3.5)$$

which leads to

$$\sum_{\pi=1}^3 \eta^{\pi} = 1 \quad (3.6)$$

Let us apply the volume fraction concept to an intrinsic microscopic conserved quantity  $\langle \psi \rangle_{\pi}$ , which is averaged over the entire volume  $dV$  of an REV at time  $t$  as

$$\Psi_{\pi}(x,t) = \frac{\langle \psi \rangle_{\pi}(x,t)}{dV} \int_{dV} \gamma^{\pi}(r,t) dV_m \quad (3.7)$$

where  $\Psi_{\pi}$  represents the macroscopically averaged value of the quantity over the entire volume  $dV$  of the REV. Then substituting the volume fraction  $\eta^{\pi}(x,t)$  of a phase  $\pi$  with respect to the entire volume  $dV$  of the REV into Eqn. (3.7), we have

$$\Psi_{\pi}(x,t) = \eta^{\pi}(x,t) \langle \psi \rangle_{\pi}(x,t) \quad (3.8)$$

This is known as *volume averaging process* (Lewis and Schrefler 2000), which will be used in derivation of macroscopic governing equations later.

### 3.2.2 The size of an REV

In general, if an arbitrary elementary volume is selected as an REV, then different volumes will yield different averaged values of each quantity of interest. There is no sense in asking which of them is more ‘correct’ unless the model’s objectives in a particular case are clearly stated. Also, in a field test or laboratory, the measured values should correspond to that of the selected arbitrary elementary volume. The predicted and measured values, then, can be the same within a range of error introduced by the concept of the averaging process. However, this approach has the main drawback that since every averaged value depends on the selected size of the

arbitrary elementary volume, it must be specified by the size of the volume over which it was taken. To eliminate any size dependency of the values of quantities, it is desirable to have a universal criterion, which is based on measurable characteristics of porous media.

Using the criterion for concrete, we can determine a range of averaging volumes within which the characteristics of a concrete remain constant (theoretically). Then, computed and observed values will be close enough to consider an averaged volume in that range as an REV. Average quantities are also to be continuous in space and time. In other words, the REV must be small enough to be thought as infinitesimal (i.e. the partial derivatives in the governing equations must make sense) yet large enough to give average quantities without fluctuation depending on the size of the REV.

Figure 3-3 illustrates the requirements for the range of the REV in variation of void ratios with respect to averaging volumes. For very small values of  $dV(x)$ , the void ratio can be one or zero since  $x$  happens to fall in either the void space or the solid phase. However, as the size of  $dV(x)$  increases, large fluctuations in the porosity can be observed. As the size of  $dV(x)$  continues to increase, we notice that the fluctuations gradually decay. When  $dV(x) = dV^{\min}$ , the void ratio becomes, more or less, constant with only small fluctuations. The REV is the volume within the range of  $dV^{\min} \leq dV \leq dV^{\max}$  that makes the void ratio independent of the volume size and thus, a single valued function of  $x$  only. Then the void ratio represents the *porosity* of the porous medium.

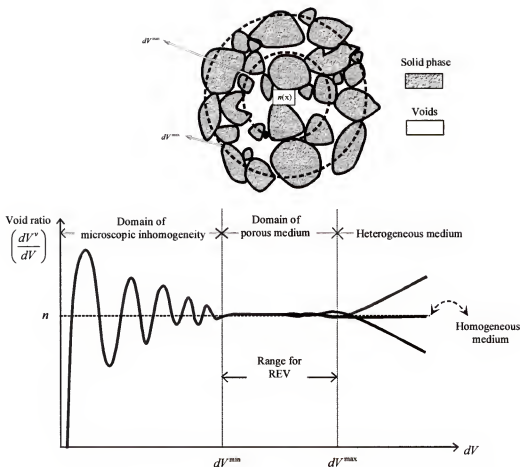


Figure 3-3 Variation of the void ratio as a function of averaging volume (after Bear and Bachmat 1998)

Considering multiphase mass and heat transfer in concrete, where the state of each phase is described by a set of variables (permeability, density, and conductivity, etc.), we undertake a similar approach that associates with the geometrical characteristics of the void space, e.g. the *porosity*, with respect to these variables. A range for REV is found and selected for each variable. Then a common range of REV, which is determined by a characteristic length  $\lambda$  of the average volume that depends on the specific constituent (or phase) of the domain, can be found for all of them. The characteristic length of the REV is required that

$$d_{\max} < \lambda < L$$

where  $d_{\max}$  is the maximum dimension of a pore or a grain of concrete and  $L$  is the characteristic length of the entire domain of the concrete. Therefore, for every parameter and state variable of a phase within a given concrete domain, we are able to define an average quantity. One such parameter is porosity and we now look into a mathematical representation of porosity by the volume fractions of concrete.

### 3.2.3 Mathematical representation of the averaged porosity

The total void space within the REV is defined as the volume of the interconnected void space  $dV^{vc}$  and the total volume of the isolated simply connected voids  $dV^{vi}$  that are occupied by both the fluid phases

$$dV^{vt} = dV^{vc} + dV^{vi} = dV^w + dV^g \quad (3.9)$$

where  $dV^{vt}$  represents the total void space within the REV and  $dV^w$  and  $dV^g$  represent the spaces occupied by the liquid water and the gaseous phases, respectively. The ratio is defined as the *total (volumetric) porosity* of the porous medium at point  $x$ .

$$n(x) \equiv \left. \frac{dV^w + dV^g}{dV} \right|_x = \left. \frac{dV^{vt}}{dV} \right|_x \quad (3.10)$$

From the point of view of fluid flow, only the volume of  $dV^{vc}$  is referred to as the volume of the *effective void space subdomain*. Then the *effective porosity* of the porous medium at  $x$  is defined as

$$n_e(x) \equiv \left. \frac{dV^{vc}}{dV} \right|_x \quad (3.11)$$

However, throughout this study, we assume concrete as a porous medium in which all the void spaces are interconnected. Its volume is referred to as  $dV^v$ , instead of  $dV^{vc}$ , and the symbol  $n$  will be used to denote the *porosity*.

With the volume fraction  $\eta^\pi(x,t)$ , the volume averaging theory is now applied to the geometrical characteristics of the volume fractions of the constituents (i.e., solid, liquid, and gaseous phase)

$$\begin{aligned} \eta^s &= 1 - \frac{(dV^w + dV^g)}{dV} = 1 - n \\ \eta^w &= n \cdot \frac{dV^w}{(dV^w + dV^g)} = n \cdot S_w \\ \eta^g &= n \cdot \frac{dV^g}{(dV^w + dV^g)} = n \cdot S_g \end{aligned} \quad (3.12)$$

with

$$S_w + S_g = 1 \quad (3.13)$$

where  $S_w$  and  $S_g$  are the degree of liquid phase (i.e., water) saturation and the degree of gaseous phase (i.e., a mixture of air and vapor) saturation, respectively.

To summarize the discussion this far, the values of the parameters that describe all averaged geometrical characteristics of the microstructure of the porous medium at any point of the macroscopic domain are required to be single value functions of the location of that point and of time, which is independent of the size of the averaged volume. By using this postulate, particular macroscopic governing equations for



extensive quantities of interest are derived by using the averaging theory that has been established on spatial averaging processes in this section. First, we will develop the generic balance equation of an extensive quantity at the microscopic level in the subsequent section.

### 3.3 Balance Laws for Continua

The formulation of a generic balance equation for an extensive quantity (e.g., energy) in the neighborhood of an arbitrary point within continua for single materials is presented. Consider a point, which is located within a fixed finite domain,  $U$ , referred to as a *control volume* and bounded by a closed surface  $\partial U$  as shown in Figure 3-4.

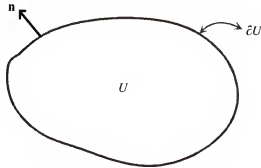


Figure 3-4 A control volume  $U$  bounded by a closed surface  $\partial U$  and outward unit normal vector  $\mathbf{n}$

For a generic conserved variable  $\psi$  defined per unit mass and describing the microscopic situation of the body, the general form of a balance law over  $U$  of the body may be expressed as

$$\underbrace{\left\{ \begin{array}{c} \text{rate change of} \\ \psi \text{ within } U \end{array} \right\}}_{(a)} - \underbrace{\left\{ \begin{array}{c} \text{the flux of } \psi \text{ across } \partial U \end{array} \right\}}_{(b)} - \underbrace{\left\{ \begin{array}{c} \text{external supply} \\ \text{of } \psi \text{ into } U \end{array} \right\}}_{(c)} = 0 \quad (3.14)$$

In mathematical form, the balance components of Eqn. (3.14) can be expressed as

(a) the rate change of the amount of  $\psi$  within  $U$ ,

$$\frac{d}{dt} \int_V \rho \psi \, d\Omega \quad (3.15)$$

(b) the flux,  $\mathbf{i}$ , into  $U$  through  $\partial U$ ,

$$\oint_{\partial U} \mathbf{i} \cdot \mathbf{n} \, dS \quad (3.16)$$

and (c) the external supply,  $\hat{g}$ , of  $\psi$ ,

$$\int_V \rho \hat{g} \, dU \quad (3.17)$$

where  $\rho$  is the mass density of  $\psi$  (i.e., the amount of  $\psi$  per unit volume of the body)

and  $\mathbf{n}$  is outward unit vector normal to  $\partial U$ .

Substituting the mathematical expressions above into Eqn. (3.14), we now have the general form of a balance equation of  $\psi$  within  $U$

$$\frac{d}{dt} \int_V \rho \psi \, d\Omega - \oint_{\partial U} \mathbf{i} \cdot \mathbf{n} \, dS - \int_V \rho \hat{g} \, d\Omega = 0 \quad (3.18)$$

For example, if we set  $\psi = 1$ ,  $\mathbf{i} = 0$ , and  $\hat{g} = 0$ , then Eqn. (3.18) becomes the mass balance equation of a simple continuum

$$\frac{d}{dt} \int_V \rho \, d\Omega = 0 \quad (3.19)$$

which states that the total mass inside a material volume remains constant for a continuum. For the momentum balance, the momentum per unit mass or velocity  $\mathbf{v}(\mathbf{x}, t)$  is taken for  $\psi$  while we set  $\mathbf{i} = \boldsymbol{\sigma}$ , and  $\hat{g} = \mathbf{b}$ . Then, we have

$$\frac{d}{dt} \int_U \rho \mathbf{v} \, d\Omega - \oint_{\partial U} \boldsymbol{\sigma} \cdot \mathbf{n} \, dS - \int_U \rho \mathbf{b} \, d\Omega = 0 \quad (3.20)$$

where the momentum flux is represented by  $\boldsymbol{\sigma}$  (stress) and the body force per unit mass acting on the body is denoted by  $\mathbf{b}$  (the gravitational acceleration).

If  $\psi$  is used to represent the internal energy  $E$  plus the kinetic energy  $\frac{1}{2} \mathbf{v} \cdot \mathbf{v}$  per unit mass,  $\psi = E + \frac{1}{2} \mathbf{v} \cdot \mathbf{v}$ , the energy balance in the body can be expressed

$$\frac{d}{dt} \int_U \rho \left( E + \frac{1}{2} \mathbf{v} \cdot \mathbf{v} \right) d\Omega + \oint_{\partial U} (\mathbf{q} - \boldsymbol{\sigma} \cdot \mathbf{v}) \cdot \mathbf{n} \, dS - \int_U (h + \mathbf{b} \cdot \mathbf{v}) \, d\Omega = 0 \quad (3.21)$$

where the energy flux has two parts  $\mathbf{i} = -\mathbf{q} + \boldsymbol{\sigma} \cdot \mathbf{v}$ , that is,  $-\mathbf{q}$  represents the heat flux and  $\boldsymbol{\sigma} \cdot \mathbf{v}$  accounts for the work done by stress. The external-energy supply term,  $\hat{\mathbf{g}}$ , in Eqn. (3.18) is replaced by the rate of external heating (e.g., radiation),  $h$ , and the work done by body forces,  $\mathbf{b} \cdot \mathbf{v}$ .

### 3.3.1 Governing differential equations for microscopic conserved quantities

Recall the following two theorems (1) Gauss theorem,  $\oint_{\partial U} \mathbf{f} \cdot \mathbf{n} \, dS = \int_U \nabla \cdot \mathbf{f} \, d\Omega$  for a differentiable vector-valued function  $\mathbf{f}(\mathbf{x}, t)$  on a region containing  $U$  and  $\partial U$ , and (2) the Reynolds transport theorem,  $\frac{d}{dt} \int_U f \, d\Omega = \int_U \left[ \frac{\partial f}{\partial t} + \nabla \cdot (\mathbf{v} f) \right] d\Omega$ , where  $\mathbf{v}(\mathbf{x}, t)$  is the velocity of the material.

Applying the Reynolds transport theorem to the first term in Eqn. (3.18) and the Gauss theorem to the second term, we have

$$\int_U \left[ \frac{\partial(\rho\psi)}{\partial t} + \mathbf{v} \cdot \nabla(\rho\psi) + \rho\psi \nabla \cdot \mathbf{v} - \nabla \cdot \mathbf{i} - \rho \hat{g} \right] d\Omega = 0 \quad (3.22)$$

However, if  $f(\mathbf{x},t)$  is a continuous real-valued function defined on a region containing  $U$  and  $\partial U$  and  $\int_U f(\mathbf{x},t) d\Omega = 0$  for every subregion of  $U$ , then  $f(\mathbf{x},t)$  vanishes identically on  $U$ , i.e., the fundamental lemma of calculus of variations. Therefore, the terms in the bracket in Eqn. (3.22) can be written

$$\frac{\partial(\rho\psi)}{\partial t} + \mathbf{v} \cdot \nabla(\rho\psi) + \rho\psi \nabla \cdot \mathbf{v} - \nabla \cdot \mathbf{i} - \rho \hat{g} = 0 \quad (3.23)$$

for any arbitrary subregion of  $U$ . By defining the material derivative operator  $D/Dt = \partial/\partial t + \mathbf{v} \cdot \nabla$ , which measures the time rate of change at a specific material point, the local balance equation can be expressed

$$\frac{D(\rho\psi)}{Dt} + \rho\psi \nabla \cdot \mathbf{v} - \nabla \cdot \mathbf{i} - \rho \hat{g} = 0 \quad (3.24)$$

Therefore, if we set  $\psi = 1$ ,  $\mathbf{i} = 0$ , and  $\hat{g} = 0$ , the local mass balance law defined by Eqn. (3.19) is rewritten as

$$\frac{D\rho}{Dt} + \rho \nabla \cdot \mathbf{v} = 0 \quad (3.25)$$

For the momentum the local balance law is rewritten

$$\frac{D(\rho\mathbf{v})}{Dt} + \rho\mathbf{v} \nabla \cdot \mathbf{v} - \nabla \cdot \boldsymbol{\sigma} - \rho\mathbf{b} = 0 \quad (3.26)$$

Since  $D(\rho\mathbf{v})/Dt = \rho D\mathbf{v}/Dt + \mathbf{v} D\rho/Dt$ ,

$$\rho \frac{Dv}{Dt} + v \left( \frac{D\rho}{Dt} + \rho \nabla \cdot v \right) - \nabla \cdot \sigma - \rho b = 0 \quad (3.27)$$

However, by virtue of the mass balance, the term in parentheses in the last equation vanishes. Thus we have

$$\rho \frac{Dv}{Dt} - \nabla \cdot \sigma - \rho b = 0 \quad (3.28)$$

which is known as the linear momentum balance law or Cauchy's first law of continuum mechanics.

For the local energy balance, Eqn. (3.21) is rewritten in the form of

$$\frac{D}{Dt} \left[ \rho \left( E + \frac{1}{2} v \cdot v \right) \right] + \rho \left( E + \frac{1}{2} v \cdot v \right) \nabla \cdot v + \nabla \cdot (q - \sigma \cdot v) - \rho (h + b \cdot v) = 0 \quad (3.29)$$

If we expand the material derivative and use differential identity such as

$$\nabla \cdot (\sigma \cdot v) = v \cdot (\nabla \cdot \sigma) + \sigma : \nabla v \quad (3.30)$$

then we have

$$\begin{aligned} & \rho \frac{DE}{Dt} + \nabla \cdot q - \sigma : \nabla v - \rho h + \left( \frac{D\rho}{Dt} + \rho \nabla \cdot v \right) \left( E + \frac{1}{2} v \cdot v \right) \\ & + \left\{ \rho \frac{D}{Dt} \left( \frac{1}{2} v \cdot v \right) + v \cdot (\nabla \cdot \sigma) - \rho b \cdot v \right\} = 0 \end{aligned} \quad (3.31)$$

By eliminating the terms that vanish in accordance with the mass balance in the first parenthesis and by forming the dot product of  $v$  with both sides of the momentum balance in the last parenthesis

$$\rho \frac{D}{Dt} \left( \frac{1}{2} \mathbf{v} \cdot \mathbf{v} \right) + \mathbf{v} \cdot (\nabla \cdot \boldsymbol{\sigma}) - \rho \mathbf{b} \cdot \mathbf{v} = 0 \quad (3.32)$$

and the energy balance law can be expressed in the form of

$$\rho \frac{DE}{Dt} + \nabla \cdot \mathbf{q} - \boldsymbol{\sigma} : \nabla \mathbf{v} - \rho h = 0 \quad (3.33)$$

The terms in the equation (3.33) have the following physical interpretations

$\rho DE / Dt$  is the rate of change of internal energy,  $\nabla \cdot \mathbf{q}$  is the rate of heat flow,  $-\boldsymbol{\sigma} : \nabla \mathbf{v}$  represents heating caused by compression and dissipative momentum transfer (e.g., plastic deformation), and  $-\rho h$  is the rate of heating by external supplies.

### 3.3.2 Governing differential equations for multi-phase continua

The balance laws for a multi-phase continuum are analogous to those of a simple continuum, except that global balances apply to the multi-phase mixture as a whole via an averaging process used for a frame work to construct mathematical formulations of governing field equations at the macroscopic level.

To start with, the general balance law for a generic extensive quantity defined in Eqn. (3.24) is rewritten for a multiphase mixture, which is a collection of overlapping continua called phases (or constituents)

$$\sum_{\pi} \left[ \frac{D^{\pi}(\eta^{\pi} \rho^{\pi} \psi^{\pi})}{Dt} + \eta^{\pi} \rho^{\pi} \psi^{\pi} \nabla \cdot \mathbf{v}^{\pi} - \nabla \cdot \eta^{\pi} \mathbf{i}^{\pi} - \eta^{\pi} \rho^{\pi} \hat{g}^{\pi} \right] = 0 \quad (3.34)$$

where each constituent  $\pi$  occupies a fraction of the overall mixture volume defined by a volume fraction  $\eta^{\pi}(\mathbf{x}, t)$ , and has the intrinsic mass density  $\rho^{\pi}$  with its own

velocity  $v^\pi(x, t)$ . Introducing the material time derivative of any differential function  $f^\pi(x, t)$  of the  $\pi$  phase as

$$\frac{D^\pi f^\pi}{Dt} = \frac{\partial f^\pi}{\partial t} + \text{grad } f^\pi \cdot v^\pi \quad (3.35)$$

we can define the time derivative of  $f^\pi(x, t)$  taken with respect to another moving phase  $\alpha$

$$\frac{D^\alpha f^\pi}{Dt} = \frac{\partial f^\pi}{\partial t} + \text{grad } f^\pi \cdot v^{\alpha\pi} \quad (3.36)$$

where

$$v^{\alpha\pi} = v^\alpha - v^\pi \quad (3.37)$$

While the equation (3.34) provides balance laws for the overall mixture, it can be divided for each constituent's balance laws

$$\frac{D^\pi(\eta^\pi \rho^\pi \psi^\pi)}{Dt} + \eta^\pi \rho^\pi \psi^\pi \nabla \cdot v^\pi - \nabla \cdot \eta^\pi i^\pi - \eta^\pi \rho^\pi \hat{g}^\pi = e^\pi \quad (3.38)$$

The term  $e^\pi$  on the right hand side accounts for all exchanges of the conserved quantity  $\psi^\pi$  into constituent  $\pi$  from other constituents. It should be noted that, in order to conserve the balance of the overall multi-phase mixture, we must have

$$\sum_\pi e^\pi = 0 \quad (3.39)$$

### 3.4 Macroscopic Mass Balance Law for a Multiphase Mixture

From Eqn. (3.38), we will derive the macroscopic mass balance law for each individual constituent denoted by  $\pi$  (i.e., the solid, the liquid, and the gaseous phase) in a multiphase mixture.

#### 3.4.1 The mass balance law for the solid phase

As with the mass balance for the solid phase (superscript  $s$ ) as a single continuum, we set  $\psi^\pi = 1$ ,  $i^\pi = 0$ , and  $\hat{g}^\pi = 0$  in Eqn. (3.38)

$$\frac{D^s \eta^s \rho^s}{Dt} + \eta^s \rho^s \operatorname{div}(\mathbf{v}^s) = 0 \quad (3.40)$$

However, since  $\eta^s = 1 - n$  from Eqn. (3.12), the macroscopic mass balance law for the solid phase is rewritten

$$\frac{D^s [(1-n)\rho^s]}{Dt} + (1-n)\rho^s \operatorname{div}(\mathbf{v}^s) = 0 \quad (3.41)$$

or, since  $D/Dt = \partial/\partial t + \mathbf{v} \cdot \nabla$ ,

$$\frac{\partial [(1-n)\rho^s]}{\partial t} + \operatorname{div}[(1-n)\rho^s \mathbf{v}^s] = 0 \quad (3.42)$$

where  $(1-n)\rho^s$  is the macroscopic volume-averaged mass density of the solid phase and  $\mathbf{v}^s$  is its velocity. It is assumed that there is no mass exchange (e.g., chemical interaction) between the solid phase and the other phases, i.e.,  $e^s = 0$ .



By using the vector identity,

$$\operatorname{div}[(1-n)\rho^s \mathbf{v}^s] = (1-n)\rho^s \operatorname{div} \mathbf{v}^s + \operatorname{grad}[(1-n)\rho^s] \cdot \mathbf{v}^s \quad (3.43)$$

and assuming  $\operatorname{grad}[(1-n)\rho^s] = 0$ , Eqn. (3.42) becomes

$$\frac{\partial[(1-n)\rho^s]}{\partial t} + (1-n)\rho^s \operatorname{div} \mathbf{v}^s = 0 \quad (3.44)$$

Expanding and then dividing both sides by  $\rho^s$ , we have another form of the macroscopic mass balance of the solid phase

$$\frac{(1-n)}{\rho^s} \frac{\partial \rho^s}{\partial t} - \frac{\partial n}{\partial t} + (1-n) \operatorname{div} \mathbf{v}^s = 0 \quad (3.45)$$

or

$$\frac{(1-n)}{\rho^s} \frac{D^s \rho^s}{Dt} - \frac{D^s n}{Dt} + (1-n) \operatorname{div} \mathbf{v}^s = 0 \quad (3.46)$$

### 3.4.2 The mass balance law for the fluid phases

Again, as with the mass balance for a fluid phase  $\pi$  (where  $\pi \neq s$ ) as a single continuum, we set  $\psi^\pi = 1$ ,  $i^\pi = 0$ , and  $\hat{g}^\pi = 0$  in Eqn. (3.38)

$$\frac{D^\pi(\eta^\pi \rho^\pi)}{Dt} + \eta^\pi \rho^\pi \operatorname{div} \mathbf{v}^\pi = \pm \eta^\pi \rho^\pi e^\pi \quad (3.47)$$

where  $\eta^\pi \rho^\pi$  is the macroscopic volume-averaged mass density of the fluid phase,

$\mathbf{v}^\pi$  is its velocity, and  $\eta^\pi \rho^\pi e^\pi$  is the rate of mass exchange between the fluid phases

(e.g.,  $-\eta^\pi \rho^\pi e^\pi$  is the quantity of water lost through evaporation per unit time per unit

volume and  $+\eta^\pi \rho^\pi e^\pi$  is the quantity of vapor gained through condensation per unit time per unit volume).

By replacing the volume fraction  $\eta^\pi$  by  $nS_\pi$  (see Eqn. (3.12)) and the rate of mass exchange term  $\eta^\pi \rho^\pi e^\pi$  by  $\dot{m}$ ,

$$\frac{D^\pi(nS_\pi \rho^\pi)}{Dt} + nS_\pi \rho^\pi \text{div } \mathbf{v}^\pi = \pm \dot{m} \quad (3.48)$$

where  $S_\pi$  is the degree of saturation of the fluid phases.

Therefore, the macroscopic mass balance of the liquid phase (i.e. water) is defined

$$\frac{D^w(nS_w \rho^w)}{Dt} + nS_w \rho^w \text{div } \mathbf{v}^w = -\dot{m} \quad (3.49)$$

where  $-\dot{m}$  is the quantity of water lost through evaporation per unit time per unit volume.

#### 3.4.4 Species mass balance in the gaseous phase

Recall that a collection of overlapping continua called phases was defined earlier as a multi-phase mixture. The constituents (or phases) can be segregated at the microscopic level, where the phases behave as continua but their small-scale motions are inaccessible to field measurement. Such mixtures are named multi-phase mixtures.

However, the gaseous phase considered in this study is assumed to be a perfect mixture of two ideal gas species, i.e. dry air and vapor. That is, the single gas phase can be decomposed into two different species where the segregation occurs at a

molecular scale but not at the microscopic scale. It is called a *multi-species* mixture, the species (or components), dry air and vapor, of the gaseous phase (i.e., moist air), are considered to be miscible and they occupy the same volume fraction. That is,

$$\rho^g = \rho^{gw} + \rho^{ga} \quad (3.50)$$

where the mass density of the gas phase is the sum of the mass densities of dry air (superscript *ga*) and vapor (superscript *gw*). Introducing the mass fraction of component  $\alpha = ga, gw$ ,

$$\omega^\alpha = \rho^\alpha / \rho^g \quad (3.51)$$

By using the mass fraction, the velocity of the gas phase  $v^g$  can be expressed

$$v^g = \frac{1}{\rho^g} (\rho^{ga} v^{ga} + \rho^{gw} v^{gw}) = \omega^{ga} v^{ga} + \omega^{gw} v^{gw} \quad (3.52)$$

This is called the *barycentric* velocity, which is the mass-weighted mean velocity.

Furthermore, this implies that a difference between the species' velocities and the mean velocity of the gaseous phase exists. We define the velocity difference as the *diffusion* velocity of component  $\alpha$  with respect for the mean gas flow,  $u^\alpha$

$$u^\alpha = v^\alpha - v^g \quad (3.53)$$

From the macroscopic mass balance of the fluid phases of Eqn. (3.48), we introduce the diffusion velocity into the macroscopic mass balance law for each component of the gaseous phase, first, for dry air,

$$\frac{\partial(nS_g \rho^{ga})}{\partial t} + \text{div}[nS_g \rho^{ga} \mathbf{u}^{ga}] + \text{div}[nS_g \rho^{ga} \mathbf{v}^g] = 0 \quad (3.54)$$

and next for vapor,

$$\frac{\partial(nS_g \rho^{gw})}{\partial t} + \text{div}[nS_g \rho^{gw} \mathbf{u}^{gw}] + \text{div}[nS_g \rho^{gw} \mathbf{v}^g] = \dot{m} \quad (3.55)$$

where the terms  $nS_g \rho^a \mathbf{u}^a$  accounts for the diffusive mass flux of component  $\alpha$ .

By introducing the diffusive mass flux of each component  $\alpha$  as

$$\mathbf{j}_g^a = nS_g \rho^a \mathbf{u}^a \quad (3.56)$$

the macroscopic mass balance law for dry air of the gaseous phase is then rewritten

$$\frac{\partial(nS_g \rho^{ga})}{\partial t} + \text{div} \mathbf{j}_g^{ga} + \text{div}[nS_g \rho^{ga} \mathbf{v}^g] = 0 \quad (3.57)$$

and thus the macroscopic mass balance law for vapor becomes

$$\frac{\partial(nS_g \rho^{gw})}{\partial t} + \text{div} \mathbf{j}_g^{gw} + \text{div}[nS_g \rho^{gw} \mathbf{v}^g] = \dot{m} \quad (3.58)$$

where the first term on the left side accounts for the accumulation of component  $\alpha$  known as the *mass concentration* of  $\alpha$  in the gaseous phase, i.e. moist air, the second term models the diffusion of  $\alpha$  with respect to the mean macroscopic flow of moist air in the porous medium, the third term models the advection of  $\alpha$  with the mean macroscopic flow velocity, and the right hand side of the equation accounts for the exchange of  $\alpha$  to or from the other molecular species in the phase or the other phase,

i.e. the liquid phase in the porous medium. The species mass balance law is later used to obtain general field equations, which will be numerically solved in Chapter 4.

### 3.5 Macroscopic Linear Momentum Balance Law for a Multiphase Mixture

We now look into applications of mixture theory to the equations governing fluid flows through porous media. We will start from the generic balance equation of a single constituent, Eqn. (3.38) to derive the momentum balance for a single fluid phase flowing through a concrete matrix. With the concept of the volume fraction, the macroscopic momentum balance equations of the fluid phases will be extended to Darcy's law, the fundamental field equation for porous-medium flow.

#### 3.5.1 The linear momentum balance law for the solid phase

If we set  $\psi^\pi = \mathbf{v}^\pi$ ,  $\mathbf{i}^\pi = \boldsymbol{\sigma}^\pi$ ,  $\hat{\mathbf{g}}^\pi = \mathbf{b}^\pi$ , and  $e^\pi = r^\pi$  (i.e., the rate of momentum exchange into the phase  $\pi$ ) in Eqn. (3.38), then we have

$$\frac{D^\pi(\eta^\pi \rho^\pi \mathbf{v}^\pi)}{Dt} + \eta^\pi \rho^\pi \mathbf{v}^\pi \cdot \nabla \bullet \mathbf{v}^\pi - \nabla \bullet \eta^\pi \boldsymbol{\sigma}^\pi - \eta^\pi \rho^\pi \mathbf{b}^\pi = r^\pi \quad (3.59)$$

Eliminating terms on the left side of this equation in a manner similar to that used in derivation of the momentum balance law of a simple continuum (see also the derivation of Eqn. (3.28)), we have the macroscopic linear momentum balance law written as

$$\eta^\pi \rho^\pi \frac{D^\pi \mathbf{v}^\pi}{Dt} - \nabla \bullet \eta^\pi \boldsymbol{\sigma}^\pi - \eta^\pi \rho^\pi \mathbf{b}^\pi = r^\pi \quad (3.60)$$

or

$$\eta^\pi \rho^\pi \left( \frac{\partial \mathbf{v}^\pi}{\partial t} + \mathbf{v}^\pi \cdot \text{grad } \mathbf{v}^\pi \right) - \nabla \cdot \eta^\pi \sigma^\pi - \eta^\pi \rho^\pi \mathbf{b}^\pi = \mathbf{r}^\pi \quad (3.61)$$

Let us neglect the acceleration terms as a first approximation for slow flow of a macroscopically averaged fluid phase through a porous medium. Therefore, we simplify Eqn. (3.60) for the macroscopic momentum balance equation

$$-\nabla \cdot \eta^\pi \sigma^\pi - \eta^\pi \rho^\pi \mathbf{g} = \mathbf{r}^\pi \quad (3.62)$$

where  $\mathbf{b}^\pi$  is replaced by  $\eta^\pi \mathbf{g}$ , which accounts for the averaged gravitational effects.

Now we turn to the momentum balance law for the solid phase. Neglecting the velocity of the solid phase,  $\mathbf{v}^s = 0$ , we further simplify Eqn. (3.60) for the linear momentum balance equation of the solid phase

$$\nabla \cdot \eta^s \sigma^s + \eta^s \rho^s \mathbf{g} = -\mathbf{r}^s \quad (3.63)$$

where  $\sigma^s$  represents the stress tensor in the solid phase,  $\mathbf{g}$  represents the gravitational acceleration, and  $\mathbf{r}^s$  represents the momentum exchange to the other fluid phases.

### 3.5.2 The linear momentum balance law for the fluid phases

For the fluid phases, we begin with two assumptions (1) The fluid's inertial effect is assumed to be negligible on its momentum balance

$$\frac{D^\pi \mathbf{v}^\pi}{Dt} = 0 \quad \text{where } \pi = w, g \quad (3.64)$$

and (2) the gravity is the only body force in the form of

$$b^\pi = g \quad \text{where } \pi = w, g \quad (3.65)$$

Therefore, we have the linear momentum balance equation for the fluid phases written as

$$\nabla \cdot \eta^\pi \sigma^\pi + \eta^\pi \rho^\pi g = -r^\pi \quad \text{where } \pi = w, g \quad (3.66)$$

Since  $v^s = 0$ , the momentum exchange  $r^\pi$  of the fluid phases to the solid phase can be expressed by *Stokes' drag* (Allen et al. 1988)

$$r^\pi = \frac{\eta^\pi}{\gamma^\pi} (v^s - v^\pi) = -\frac{\eta^\pi v^\pi}{\gamma^\pi} \quad \text{where } \pi = w, g \quad (3.67)$$

where the constant  $\gamma^\pi$  is called the fluid *mobility*. Then the linear momentum balance equation of the fluid phases becomes

$$\nabla \cdot \eta^\pi \sigma^\pi + \eta^\pi \rho^\pi g = \frac{\eta^\pi v^\pi}{\gamma^\pi} \quad \text{where } \pi = w, g \quad (3.68)$$

In addition, the counterpart of the momentum exchange of the solid phase to the fluid phases in Eqn. (3.63) becomes

$$r^s = \frac{\eta^s v^s}{\gamma^s} \quad \text{where } \pi = w, g \quad (3.69)$$

in order to meet the requirement in Eqn. (3.39).

### 3.5.3 The linear momentum balance law for the multiphase medium

Through summing all the momentum balance equations written for the solid and fluid phases and by assuming continuity of stress field across the solid-fluid interface,

the linear momentum balance equation for the multiphase medium as a whole is obtained as

$$\nabla \cdot (\eta^s \sigma^s + \eta^\pi \sigma^\pi) + (\eta^s \rho^s + \eta^\pi \rho^\pi) g - \eta^\pi \rho^\pi (\mathbf{v}^\pi \cdot \text{grad } \mathbf{v}^\pi) = 0 \quad (3.70)$$

where  $\pi = w, g$ .

Further simplification can be made on the last equation by neglecting the last term on the left hand side that depends on the gradient of the fluid velocity, by defining the *total stress*  $\sigma^{total}$  acting on a unit area of the multiphase medium

$$\sigma^{total} = \eta^s \sigma^s + \eta^w \sigma^w + \eta^g \sigma^g = (1-n) \sigma^s + n(S_w \sigma^w + S_g \sigma^g) \quad (3.71)$$

and by introducing the *averaged mass density* of the multiphase medium

$$\rho^{avg} = \eta^s \rho^s + \eta^w \rho^w + \eta^g \rho^g = (1-n) \rho^s + n(S_w \rho^w + S_g \rho^g) \quad (3.72)$$

Therefore *the linear momentum balance equation of the multiphase medium* becomes

$$\nabla \cdot \sigma^{total} + \rho^{avg} g = 0 \quad (3.73)$$

where  $\sigma^{total}$  is the total stress acting on a unit area of the multiphase medium and  $\rho^{avg}$  is the volume-averaged mass density of the multiphase medium.

### 3.6 Macroscopic Energy Balance Law for a Multiphase Mixture

Again, we shall begin with the generic macroscopic balance equation of Eqn. (3.38) by taking the following components into account in the generic equation. First, if we set  $\psi^\pi = E^\pi + \frac{1}{2} \mathbf{v}^\pi \cdot \mathbf{v}^\pi$ , then the generic extensive quantity  $\psi^\pi$  is considered as



the internal energy per unit mass  $E^\pi$  plus the kinetic energy per unit mass  $\frac{1}{2} \mathbf{v}^\pi \cdot \mathbf{v}^\pi$ .

The flux of energy  $i^\pi$  has also two parts we set  $i^\pi = \eta_\pi(\sigma^\pi \cdot \mathbf{v}^\pi - q^\pi)$  where  $\sigma^\pi \cdot \mathbf{v}^\pi$  accounts for the work done by stress and  $-q^\pi$  represents the heat flux. For external heating supplies, we have the rate of external heating (e.g., attributable to radiation)  $h^\pi$  and work-done by body forces denoted by  $b^\pi \cdot \mathbf{v}^\pi$ . Finally, the exchange of energy between phases due to phase change is substituted for  $e^\pi$ . To summarize, we have the following expressions

$$\begin{aligned}\psi^\pi &= E^\pi + \frac{1}{2} \mathbf{v}^\pi \cdot \mathbf{v}^\pi \\ i^\pi &= \eta_\pi(\sigma^\pi \cdot \mathbf{v}^\pi - q^\pi) \\ \hat{g}^\pi &= h^\pi + b^\pi \cdot \mathbf{v}^\pi \\ e^\pi &= \rho^\pi R^\pi\end{aligned}\tag{3.74}$$

Therefore, substituting these components into Eqn. (3.38), we have

$$\begin{aligned}\frac{D^\pi \left[ \eta^\pi \rho^\pi \left( E^\pi + \frac{1}{2} \mathbf{v}^\pi \cdot \mathbf{v}^\pi \right) \right]}{Dt} &+ \eta^\pi \rho^\pi \left( E^\pi + \frac{1}{2} \mathbf{v}^\pi \cdot \mathbf{v}^\pi \right) \nabla \cdot \mathbf{v}^\pi \\ &- \nabla \cdot \eta_\pi(\sigma^\pi \cdot \mathbf{v}^\pi - q^\pi) - \eta^\pi \rho^\pi (h^\pi + b^\pi \cdot \mathbf{v}^\pi) = \eta^\pi \rho^\pi R^\pi\end{aligned}\tag{3.75}$$

By a similar approach to simplify the formulation of Eqn. (3.33)—the generic local energy balance equation—Eqn. (3.75) can be written in a simplified form as

$$\eta^\pi \rho^\pi \frac{D^\pi E^\pi}{Dt} + \eta^\pi \nabla \cdot q^\pi - \eta^\pi \sigma^\pi : \nabla \mathbf{v}^\pi - \eta^\pi \rho^\pi (h^\pi + g \cdot \mathbf{v}^\pi) = \eta^\pi \rho^\pi R^\pi\tag{3.76}$$

or

$$\begin{aligned} \eta^\pi \frac{\partial}{\partial t}(\rho^\pi E^\pi) + \eta^\pi \nabla \cdot (\rho^\pi E^\pi \mathbf{q}^\pi) + \eta^\pi \nabla \cdot \mathbf{q}^\pi \\ - \eta^\pi \boldsymbol{\sigma}^\pi : \nabla \mathbf{v}^\pi - \eta^\pi \rho^\pi (h^\pi + \mathbf{g} \cdot \mathbf{v}^\pi) = \eta^\pi \rho^\pi R^\pi \end{aligned} \quad (3.77)$$

where  $E^\pi$  is the intrinsic specific energy of a control volume of a phase  $\pi$ ,  $\mathbf{q}^\pi$  is the internal heat flux in the phase,  $h^\pi$  is the heat source, and  $R^\pi$  is the exchange of internal energy (e.g. latent heat) between phases due to phase change. A physical interpretation of the last equation can be given in that the first term on the left represents the rate of change of internal energy,  $\nabla \cdot \mathbf{q}^\pi$  represents the rate of heat flow,  $-\boldsymbol{\sigma}^\pi : \nabla \mathbf{v}^\pi$  accounts for heating by mechanical deformation (e.g., plastic deformation or viscous friction),  $-\eta^\pi \rho^\pi (h^\pi + \mathbf{g} \cdot \mathbf{v}^\pi)$  accounts for external heating supplies plus external work done by body forces, and  $\eta^\pi \rho^\pi R^\pi$  accounts for energy exchange of a phase through phase change. This is the *macroscopic* energy balance equation for a constituent of a multiphase continuum.

Therefore, the energy balance of the total system can be written as

$$\sum_\pi \left[ \eta^\pi \rho^\pi \frac{D^\pi E^\pi}{Dt} + \eta^\pi \nabla \cdot (\rho^\pi E^\pi \mathbf{q}^\pi) - \eta^\pi \boldsymbol{\sigma}^\pi : \nabla \mathbf{v}^\pi - \eta^\pi \rho^\pi (h^\pi + \mathbf{g} \cdot \mathbf{v}^\pi) - \eta^\pi \rho^\pi R^\pi \right] = 0 \quad (3.78)$$

which physically means that the total balance of energy exchange among all the phases is zero. After introducing constitutive relationships, we will come back to refine the macroscopic energy balance equation.

### 3.7 Constitutive Equations

While the formulation of governing equations sketched so far provides a basis for the analysis of continuum phenomena of mass and heat transfer in a porous

medium, they do not contain information regarding the properties (e.g. mechanical properties of a particular continuum), which are necessary to form a determined system.

The additional information is contained in what are known as *constitutive equations*. The form of relationships between the fluxes and driving forces in the mass-, momentum- and energy-balance equations is usually taken by constitutive equations. The linear relationship between stress and strain in an elastic solid is an example of a constitutive assumption. Other examples include that the thermal flux is a linear function of the temperature gradient and the mass diffusion flux of a species in a binary mixture of an ideal gas is linearly proportional to the concentration gradient of the species.

Despite the fact that these constitutive equations are often based on *assumptions* used for defining the behavior of ideal continua to construct mathematical models, they are arrived at by physical observation and proved by experimental evidence. Therefore, our aim in this section is oriented to develop a conceptual model in which simplification is carried out to the point where the mathematical model is amenable, yet not so crude as to miss the features of the phenomena it is intended to describe.

For quantitative solution applicable to practical engineering problems, we choose constitutive equations that are based upon quantities measurable in the laboratory, and that have been extensively validated both with reference to exact solutions and to experiments. We will begin with constitutive equations that describe the material properties of the fluid phases and only briefly deal with the solid phase. Chapter 5 will deal with this subject for the solid phase in detail, where a stress

analysis of a multiphase continuum under thermal loading conditions is the primary focus.

### 3.7.1 Flow equations in porous media

Having established the equation governing fluid flows through porous media, namely, the macroscopic linear momentum balance equation, we now turn to a specific application to the momentum balance for a single fluid phase flowing through concrete. First, we start by deriving Darcy's law, the fundamental field equation for porous-media flow. Then we will extend Darcy's law to multi-fluid flows and present constitutive field equations applicable to fluid flows through concrete.

It is assumed that each fluid phase considered in this study is Newtonian (i.e., momentum transfer via shear stresses is negligible compared with momentum exchange to the solid matrix). Thus, we can write

$$\sigma^\pi = -p_\pi \mathbf{I} \quad \text{for } \pi \neq s \quad (3.79)$$

where  $p_\pi$  presents the hydrodynamic pressure of the fluid phase and  $\mathbf{I}$  stands for the identity tensor.

Second, we assume that gravity is the only body force and has the form of

$$b^\pi = g \nabla z \quad \text{for } \pi \neq s \quad (3.80)$$

where  $g$  denotes the gravitational acceleration and  $z$  measures depth below a datum level. Applying these assumptions to Eqn. (3.68), we find that the fluid's linear momentum balance can be written as

$$\eta^\pi \mathbf{v}^\pi = -\gamma^\pi (\eta^\pi \nabla p_\pi - \eta^\pi \rho^\pi g \nabla z) \quad \text{where } \pi = w, g \quad (3.81)$$

Introducing the macroscopic fluid mobility as

$$\eta^\pi \gamma^\pi = \frac{K}{\mu^\pi} \quad (3.82)$$

where  $\mu^\pi$  represents the dynamic viscosity of the fluid and has units

$[(mass)(length)^{-1}(time)^{-1}]$  and  $K$  is the intrinsic permeability  $[(length)^2]$  of the solid matrix, we can rewrite the momentum balance equation for the fluid as

$$\eta^\pi \mathbf{v}^\pi = -\frac{K}{\mu^\pi} (\nabla p_\pi - \rho^\pi g \nabla z) \quad (3.83)$$

This is *Darcy's law*, the field equation for the macroscopic averaged velocity of the fluid of a single fluid flow in a porous medium.

Despite the fact that the permeability  $K$  in Eqn. (3.83) is supposed to be an intrinsic material property of the solid matrix, fluid flows in actual field experiments show a remarkable discrepancy between the flow of air and the flow of liquid used as a means for determining permeability, which may be seen as an error in application of laminar flow theory on which Darcy's law is based.

### 3.7.2 Deviation from Darcy' law

Deviation from Darcy's law has been observed in gas flow at low pressure the flow is faster than would be predicted by Darcy's law. Darcy's equation was developed as a linear relationship between velocity of the fluid and the gradient of pressure, which is an approximation to represent the laminar flow of *Newtonian*

*liquids* through porous media. However, on the macroscopic scale of observation, Darcy's law does not accurately predict gas flow rate through a complex network of porous media such as concrete where the pore size *generally* being considered is very small.

Contrary to laminar flow theory, on which Darcy's law is based and where we assume zero velocity in the fluid at the solid-fluid interface, the layer of gas next to the surface is in motion along the solid surface. That is, if the solid has a zero velocity, the velocity of the gas layer in the immediate vicinity of the wall still has a finite value, not necessarily zero. This contributes an additional flux to the gas flowing through a porous medium that is larger than what is expected from Poiseuille's law (Klinkenberg 1941). This phenomenon is called the *slip flow effect* or *Klinkenberg's effect*.

Klinkenberg (1941) demonstrated that the slip flow phenomenon that arises during gas flow (using a glass capillary tube as a model) was found to be quite substantial for low permeability materials. He derived the following expression for the relationship between permeability of a porous medium to gas and to liquid

$$k^g = K_\ell \left( 1 + \frac{4c\lambda}{r} \right) = K_\ell \left( 1 + \frac{b}{p} \right) \quad (3.84)$$

where  $k^g$  is the permeability to the gas,  $K_\ell$  is the permeability to liquid,  $\lambda$  is the mean free path of the gas molecules under the mean pressure  $p$  at which  $k^g$  is determined,  $c$  is a proportionality factor,  $r$  is the radius of the capillary tube in Klinkenberg's model, and  $b$  is a constant for a gas-solid system that depends on the mean free path of the gas and the size of pore channels in the porous medium. Thus, a

physical interpretation of Klinkenberg's effect can be that whenever the mean free path of the gas molecules approaches the dimensions of the flow conduit, the individual gas molecules are in motion at the solid-gas interface and contribute an additional flux.

By applying Eqn. (3.84) to Eqn. (3.83), a generalized Darcy's flow equation for gas flow in porous media results in

$$\eta^g v^g = -\frac{K_\ell}{\mu^g} \left( 1 + \frac{b}{p_g} \right) (\nabla p_g - \rho^g g \nabla z) \quad (3.85)$$

### 3.7.3 Liquid permeability

In contrast, liquids usually obey no-slip boundary conditions at the liquid-solid interface. However, in the case of water permeability testing, due to the low flow rate, steady state flow can usually be achieved only after long periods of time under high pressures that may cause changes in the solid skeleton. Besides, in case of cementitious materials such as concrete, these changes include "continuing hydration and autogeneous healing, silting of fines, dissolution and transport of  $\text{Ca}(\text{OH})_2$  from cement gel, and crystallization in larger pores" (Dhir et al. 1989). This fact has been explained by swelling and hydration of cement hydrates in contact with water, which influences permeability measured using liquid water (liquid) flow measurements.

Therefore, the permeability of cementitious materials to liquid water should not be thought as being the sole intrinsic parameter of the solid matrix. To account for this phenomenon, a scale factor is introduced in relation with the intrinsic gas permeability

$$K_\ell = \zeta K_g \quad (3.86)$$

where  $K_\ell$  is a measured permeability to liquid water,  $\zeta$  is a factor that accounts for changes of permeability of the solid matrix to liquid due to a physical/chemical interaction of the solid matrix in contact with water, and  $K_g$  is the intrinsic permeability of a cementitious, porous media to gas.

Therefore we replace Klinkenberg's expression of Eqn. (3.84) by a relationship between experimentally measured permeability and the intrinsic permeability of the cementitious, porous media to gas

$$k^g = K_g \left( 1 + \frac{b}{p_g} \right) \quad (3.87)$$

where  $K_g$  is the intrinsic permeability of a porous medium to gas,  $k^g$  is the gas permeability measured in experiments,  $b$  is a constant which quantifies the slip flow effect (called Klinkenberg's constant), and  $p_g$  is the magnitude of hydrodynamic mean pressure in the gas flow.

It is desirable to express the permeability as an intrinsic permeability (also called absolute permeability) for use in numerical simulations. Neither gas permeability nor liquid permeability can be considered to be the *single* absolute measure of the intrinsic permeability of the solid skeleton. This implies that the macroscopic permeability of a material is a function of both the solid matrix and the particular fluid used to experimentally measure the permeability.



For a complete description, fluid flows in concrete will be characterized by *two* permeability parameters intrinsic gas permeability  $K_g$ , and liquid permeability  $K_\ell$ , as well as the Klinkenberg's constant  $b$  which characterizes gas slip flow effects. These three parameters taken in conjunction can be used to fully characterize the single-phase flow of either liquid or gas through concrete. The quantification of these parameters in concrete will be presented in Chapter 4 when numerical modeling of gas and liquid flow through heated concrete is discussed.

### 3.7.4 Multi-fluid flow equation

While the discussion presented so far is useful for modeling in single-fluid flows in porous media, the flows that occur in a partially saturated porous medium exposed to nonisothermal conditions (e.g. high temperatures) involve two distinct fluid phases (e.g. liquid water and gaseous steam) flowing simultaneously. In this subsection, we illustrate the extension of the single-fluid flow to multi-fluid flows by considering a three-phase porous medium whose constituents are the solid ( $s$ ), the liquid water ( $w$ ), and the mixture of air and vapor ( $g$ ).

Remember that a porous medium exhibits different permeabilities to different fluids. This dependence implies that the presence of the liquid phase can reduce the effective permeability of the porous medium to the gas (i.e., a mixture of air and steam) and vice versa. For example, if the pores are macroscopically one quarter occupied with liquid water (degree of water saturation  $S^w = 0.25$ ), then the material will effectively be less permeable to steam flow than if it were in a completely desaturated state (degree of liquid saturation  $S^w = 0.0$ ). Therefore we can no longer

consider  $K_g$  and  $K_\ell$  to be solely properties of the solid matrix, but also we need to consider their dependence upon the extent to which each fluid phase impedes the flow of the other.

A postulate commonly used to allow for this interaction between the two phases is that the permeabilities depend on the fluid saturations, the effective permeability of each fluid phase increases with its saturation. At a macroscopic scale we assume the resulting permeability as a product of the intrinsic permeability times the relative permeability  $k_{r\pi}$

$$\begin{aligned} k_g &= K_g \bullet k_{rg}(n, S^g) \\ k_\ell &= K_\ell \bullet k_{rw}(n, S^w) \end{aligned} \quad (3.88)$$

where  $k_\pi$  stands for the *effective permeability* of the solid matrix to a constituent  $\pi$  at the degree of fluid saturation  $S^\pi$ ,  $n$  represents the porosity of the porous medium, and the function  $k_{r\pi}(n, S^\pi)$  are called a *relative permeability function*, which obeys the bounds  $0 \leq k_{r\pi}(n, S^\pi) \leq 1$ . However, since  $S^g = 1 - S^w$ , we can define the relative permeability as a function of only the degree of liquid water saturation  $S^w$ . Thus,

$$k_{r\pi} = k_{r\pi}(n, S^w) \quad (3.89)$$

Applying the new term to both the liquid and gas flow equations, we rewrite Eqn. (3.83) and Eqn. (3.85), for the liquid, as

$$\eta^w v^w = -\frac{k_{rw} K_\ell}{\mu^w} (\nabla p_w - \rho^w g \nabla z) \quad (3.90)$$

and for the gas phase, as

$$\eta^g v^g = -\frac{k_{rg} K_g}{\mu^g} \left( 1 + \frac{b}{p_g} \right) (\nabla p_g - \rho^g g \nabla z) \quad (3.91)$$

For each particular porous medium, the relations  $k_{r\pi}(n, S^w)$  are either predicted by models based on sorption equilibrium or are experimentally determined in the laboratory. A curve of relative permeabilities of concrete to water and air is developed for this study and will be presented in Chapter 4.

### 3.7.5 Mass density of water

If we set  $\psi^\pi = v^\pi$ ,  $i^\pi = 0$ , and  $\hat{g}^\pi = 0$  in Eqn. (3.38), the mass conservation of the liquid water phase can be expressed

$$\frac{D^w(\rho^w v^w)}{Dt} = 0 \quad (3.92)$$

Assuming that  $\rho^w$  is a function of the fluid pressure and temperature,  $\rho^w = \rho^w(p_w, T)$ , we can carry out the differentiation of a product as

$$\frac{1}{\rho^w} \frac{D^w(\rho^w)}{Dt} = -\frac{1}{v^w} \frac{D^w(v^w)}{Dt} = \frac{1}{\rho^w} \left( \frac{\partial \rho^w}{\partial p_w} \frac{D^w p_w}{Dt} + \frac{\partial \rho^w}{\partial T} \frac{D^w T}{Dt} \right) \quad (3.93)$$

By defining the bulk modulus of water  $K_w$  as the inverse of compressibility coefficient  $C_w$

$$C_w = \frac{1}{\rho^w} \frac{\partial \rho^w}{\partial p_w} = \frac{1}{K_w} \quad (3.94)$$

and the thermal expansion coefficient of water  $\alpha_w$  as

$$\alpha_w = -\frac{1}{\rho^w} \frac{\partial \rho^w}{\partial T} \quad (3.95)$$

it follows that

$$\frac{1}{\rho^w} \frac{D^w(\rho^w)}{Dt} = \frac{1}{K_w} \frac{D^w p_w}{Dt} - \alpha_w \frac{D^w T}{Dt} \quad (3.96)$$

Employing the equations (3.94) and (3.95) and adopting similar approach used here, the continuity equation of the fluid phases will be derived in the later section.

### 3.7.6 The ideal gas law

Since the gas phase in this study is assumed to be a perfect mixture of two ideal gases, i.e. dry air (superscript  $ga$ ) and vapor (superscript  $gw$ ), we use the ideal gas law that relates the partial pressure  $p_\alpha$  of component  $\alpha$  of the gas phase, the mass concentration  $nS_g \rho^\alpha$  in Eqn. (3.57) and the absolute temperature  $\theta$

$$\begin{aligned} p_\alpha &= \rho^\alpha \frac{\theta R}{M_\alpha} \\ p_g &= \sum_\alpha p_\alpha \end{aligned} \quad (3.97)$$

where  $R$  represents the universal gas constant,  $M_\alpha$  is the molar mass of component  $\alpha$  and  $\alpha = ga, gw$ .

Therefore,

$$\rho^g = \frac{p_g M_g}{\theta R} \quad (3.98)$$

where the molar mass of the moist air  $M_g$  is expressed with each component's molar mass and mass density

$$M_g = \left( \frac{\rho^{gw}}{\rho^g} \cdot \frac{1}{M_{gw}} + \frac{\rho^{ga}}{\rho^g} \cdot \frac{1}{M_{ga}} \right)^{-1} \quad (3.99)$$

### 3.7.7 Fick's law for diffusion

At this point, further physical interpretation is given for the diffusive mass flux  $j_g^a$  introduced in the macroscopic mass balance law for the gas phase of Eqn. (3.57). Owing to the complicated system of interconnected passages (or channels) comprising the microstructure of porous media, variations in local velocity along tortuous flow paths result from velocity distributions within each pore (both in magnitude and direction).

This quantity incorporates several types of microscopic effects, each of which contributes to the macroscopic flow of a component (or a species) of a fluid phase but none of which is very amenable to laboratory measurement. Examples include *molecular diffusion* of spreading a solute within a fluid phase, *Taylor dispersion* of longitudinal spreading of the solute within narrow pore channels, *stream splitting* (or transverse spreading) of the solute, and the *tortuosity effects* in local velocity of the fluid particle along tortuous flow paths (Allen et al. 1988).

At a molecular scale, there is a substantial transport mechanism in molecular species dissolved in gas known as *molecular diffusion* of gas, i.e. an additional mass transport phenomenon, which occurs simultaneously with convective mass transport phenomena at the microscopic scale (i.e. *mechanical dispersion*), is caused by

*molecular diffusion* resulting from variations in concentration of a gas species within the gas phase (Bear and Bachmat 1998). Thus, the diffusive flux includes two basic transport phenomena (1) molecular diffusion and (2) mechanical dispersion,

$$\mathbf{j}_g^\alpha = \mathbf{j}_{\text{mole}} + \mathbf{j}_{\text{mech}} \quad (3.100)$$

where  $\mathbf{j}_{\text{mole}}$  and  $\mathbf{j}_{\text{mech}}$  represent the molecular diffusion and mechanical dispersion fluxes, respectively.

Actually, the separation between the two processes is rather artificial, as the transport mechanism of the gaseous phase includes both processes in an inseparable form named *hydrodynamic dispersion*. Thus, the diffusive mass flux  $\mathbf{j}_g^\alpha$  in Eqn. (3.57) can be written in a form combining the two processes

$$\mathbf{j}_g^\alpha = -nS_g \rho^g \tau D_g \text{grad} \left( \frac{\rho^\alpha}{\rho^g} \right) \quad (3.101)$$

where  $D_g$  is the effective dispersion-diffusion coefficient tensor,  $\tau$  is the tortuosity factor, and  $\alpha$  is the diffusing component in the gaseous phase. This is known as *Fick's law* of binary diffusion. However, since

$$\text{grad} \left( \frac{\rho^{ga}}{\rho^g} \right) = \text{grad} \left( \frac{\rho^g - \rho^{gw}}{\rho^g} \right) = -\text{grad} \left( \frac{\rho^{gw}}{\rho^g} \right) \quad (3.102)$$

then,

$$\mathbf{j}_g^{ga} = -\mathbf{j}_g^{gw} \quad (3.103)$$

Or, by using the ideal gas law, it can be also expressed

$$j_g^\alpha = -nS_g \rho_g \frac{M_{gw} M_{gw}}{M_g^2} D_g \text{grad} \left( \frac{p_\alpha}{p_g} \right) \quad (3.104)$$

where  $\alpha$  represents component of the gaseous phase,  $\alpha = ga, gw$ , which stands for dry air and vapor, respectively. It should be noticed that the gas diffusion is an additional mass flux due to a mass concentration contributable to the gas phase flow even in the absence of a pressure gradient.

### 3.7.8 Fourier's law

A constitutive equation used for the heat flux by conduction is the generalized Fourier's law that is

$$q = -\kappa_{eff} \text{grad} \theta \quad (3.105)$$

where  $q$  is the averaged heat flux of the multiphase medium that is the sum of the partial heat fluxes  $q_\pi$  in a phase  $\pi$ , and  $\kappa_{eff}$  is the effective thermal conductivity tensor for the multiphase medium

$$\kappa_{eff} = \sum_{\pi} \eta_{\pi} \kappa_{\pi} \quad \pi = s, w \text{ and } g \quad (3.106)$$

where  $s$ ,  $w$  and  $g$  represent the solid, the liquid water, and the gas phase, respectively.

### 3.7.9 Sorption isotherms

Microstructure characteristics of a porous medium have been expressed at the macroscopic level by transfer coefficients such as permeability, diffusivity and conductivity, which have direct influence on mechanical behavior. In particular,

textural parameters such as the porosity and the pore size distribution are often thought to be crucial in the movement of liquid and gaseous water in the pore network when the porous medium is exposed to natural drying conditions.

Determination of the pore size distribution and thus the porosity of the porous medium can be achieved from a laboratory test known as water vapor desorption and adsorption test (e.g. if an oven-dry porous sample is exposed to moist air, the weight of the sample increases due to the moisture adsorption on the inner surfaces of the pores). Sorption isotherms can be used to represent, (1) the actual water content under natural drying conditions which depend on the initial boundary conditions in the numerical modeling, and (2) the relative permeability that is a function of the porosity and the degree of water saturation.

The postulate of sorption isotherms can be summarized as follows (1) the capillary pressure  $p^c$  is defined as the pressure difference between the gaseous phase (a mixture of vapor and dry air) and the liquid phase (water) as

$$p^c = p_g - p_w \quad (3.107)$$

(2) a relationship between the relative humidity (RH) and the degree of water saturation  $S_w$  can be determined by water sorption isotherms (i.e. an equilibrium curve of water content versus RH) in a laboratory test, and (3) the degree of water saturation  $S_w$  are assumed to be a function of the capillary pressure and the temperature difference  $T$  above a reference temperature  $\theta_0$

$$S_w = S_w(p^c, T) \quad (3.108)$$



where  $T = \theta - \theta_0$ .

### 3.7.10 Total stress and effective stress in the solid phase

Combining the total stress tensor defined in Eqn. (3.71) and the stress tensor written in Eqn. (3.79), we rewrite the total stress tensor as

$$\sigma^{total} = \eta^s \sigma^s + \eta^w \sigma^w + \eta^g \sigma^g = (1-n)\sigma^s - n(S_w p_w \mathbf{I} + S_g p_g \mathbf{I}) \quad (3.109)$$

or

$$\sigma^{total} = \eta^s \sigma^s + \eta^w \sigma^w + \eta^g \sigma^g = (1-n)\sigma^s - n(p_s \mathbf{I}) \quad (3.110)$$

where  $\sigma^{total}$  is the total stress tensor and  $p_s \mathbf{I}$  is the mean hydrostatic pressure tensor of both the fluids surrounding the grains, that is

$$p_s = S_w p_w + S_g p_g \quad (3.111)$$

By rearranging the terms, the constitutive law of the solid phase can be expressed through the concept of Terzaghi's *effective stress*  $\sigma^{eff}$

$$\begin{aligned} \sigma^{total} &= (1-n)\sigma^s + (1-n)(p_s \mathbf{I}) - n(p_s \mathbf{I}) - (1-n)(p_s \mathbf{I}) \\ &= (1-n)(\sigma^s + p_s \mathbf{I}) - p_s \mathbf{I} \\ &= \sigma^{eff} - p_s \mathbf{I} \end{aligned} \quad (3.112)$$

Therefore the effective stress that is responsible for the deformation in the solid phase is

$$\sigma^{eff} = \sigma^{total} + p_s \mathbf{I} \quad (3.113)$$

where  $\sigma^{eff}$  is known as Terzaghi's effective stress.

### 3.8 Physical Approximations and Field Equations

Having introduced the constitutive equations, we now transform the macroscopic balance laws to obtain the field equations, which will be solved numerically in the following chapters. Although each term in the general macroscopic equations constitutes a mathematical model that describes the contribution of a certain phenomenon to the process considered herein (i.e., thermo-mechanical behavior of concrete under multi-phase coupled heat and mass transport), only a small number of phenomena may turn out to be dominant in comparison to others.

In what follows, we will discuss the key assumptions that need to be made for deletion of terms representing non-dominant effects in the considered process. This allows us to produce simplified balance equations that may be rather less complicated yet more manageable to solve in the case of non-isothermal two-phase flow in deforming porous media, with relatively little effect on its solution, i.e., within a permissible range of error.

#### 3.8.1 Continuity equation for the fluid phases

By assuming that the solid velocity is negligible in the macroscopic mass balance equations for the solid phase, Eqn. (3.45) becomes

$$\frac{(1-n)}{\rho^s} \frac{\partial \rho^s}{\partial t} - \frac{\partial n}{\partial t} = 0 \quad (3.114)$$

For the liquid water, Eqn. (3.48) can be rewritten in terms of the material derivative with respect to the solid by using the definition of material derivatives (refer to Eqn. (3.36)) and the vector identity (also see Eqn. (3.43))

$$\frac{D^s(nS_w\rho^w)}{Dt} + \mathbf{v}^{ws} \cdot \text{grad}(nS_w\rho^w) + nS_w\rho^w \text{div}(\mathbf{v}^s + \mathbf{v}^{ws}) = -\dot{m} \quad (3.115)$$

However, since  $\mathbf{v}^s = 0$ , the relative velocity of the liquid water to the solid is replaced by the phase' velocity. This leads to rewriting the mass balance equation of the liquid water in the form of

$$\frac{D^s(nS_w\rho^w)}{Dt} + \mathbf{v}^w \cdot \text{grad}(nS_w\rho^w) + nS_w\rho^w \text{div} \mathbf{v}^w = -\dot{m} \quad (3.116)$$

By applying the vector identity, it becomes

$$\frac{D^s(nS_w\rho^w)}{Dt} + \text{div}(nS_w\rho^w \mathbf{v}^w) = -\dot{m} \quad (3.117)$$

Small displacements are assumed for the solid phase. Thus, the material time derivative  $D^s(\bullet)/Dt$ , is replaced by a partial time derivative  $\partial(\bullet)/\partial t$

$$\frac{\partial(nS_w\rho^w)}{\partial t} + \text{div}(nS_w\rho^w \mathbf{v}^w) = -\dot{m} \quad (3.118)$$

Expanding and dividing both sides of the equation by  $S_w\rho^w$ , we find

$$\frac{\partial n}{\partial t} + \frac{n}{S_w} \frac{\partial S_w}{\partial t} + \frac{n}{\rho^w} \frac{\partial \rho^w}{\partial t} + \frac{1}{S_w\rho^w} \text{div}(nS_w\rho^w \mathbf{v}^w) = -\frac{\dot{m}}{S_w\rho^w} \quad (3.119)$$

Summing Eqn. (3.119) to Eqn. (3.114), we have

$$\frac{(1-n)}{\rho^s} \frac{\partial \rho^s}{\partial t} + \frac{n}{S_w} \frac{\partial S_w}{\partial t} + \frac{n}{\rho^w} \frac{\partial \rho^w}{\partial t} + \frac{1}{S_w\rho^w} \text{div}(nS_w\rho^w \mathbf{v}^w) = -\frac{\dot{m}}{\rho^w S_w} \quad (3.120)$$

This is the *continuity equation* for liquid water.

By referring to Eqn. (3.94) and Eqn. (3.95) and defining the thermal expansion coefficient of the solid skeleton  $\alpha_s$  as

$$\alpha_s = -\frac{1}{\rho^s} \frac{\partial \rho^s}{\partial T} \quad (3.121)$$

the continuity equation of liquid water can be rewritten

$$\begin{aligned} (1-n) \left( -\alpha_s \frac{\partial T}{\partial t} \right) + \frac{n}{S_w} \frac{\partial S_w}{\partial t} + n \left( \frac{1}{K_w} \frac{\partial p_w}{\partial t} - \alpha_w \frac{\partial T}{\partial t} \right) \\ + \frac{1}{S_w \rho^w} \text{div}(n S_w \rho^w \mathbf{v}^w) = -\frac{\dot{m}}{\rho^w S_w} \end{aligned} \quad (3.122)$$

Rearranging the terms and then multiplying  $S_w$  on the both sides, we have

$$S_w \left( -(1-n)\alpha_s - n\alpha_w \right) \frac{\partial T}{\partial t} + \frac{n S_w}{K_w} \frac{\partial p_w}{\partial t} + n \frac{\partial S_w}{\partial t} + \frac{1}{\rho^w} \text{div}(n S_w \rho^w \mathbf{v}^w) = -\frac{\dot{m}}{\rho^w} \quad (3.123)$$

or

$$\alpha_{sw} \frac{\partial T}{\partial t} + \frac{n S_w}{K_w} \frac{\partial p_w}{\partial t} + n \frac{\partial S_w}{\partial t} + \frac{1}{\rho^w} \text{div}(n S_w \rho^w \mathbf{v}^w) = -\frac{\dot{m}}{\rho^w} \quad (3.124)$$

where  $\alpha_{sw}$  is defined as the relative thermal expansion coefficient of the solid to the liquid water

$$\alpha_{sw} = S_w \left( -(1-n)\alpha_s - n\alpha_w \right) \quad (3.125)$$

Finally, by substituting the generalized Darcy's law from Eqn. (3.90) into the continuity equation of the liquid water, it follows that

$$\alpha_{sw} \frac{\partial T}{\partial t} + \frac{nS_w}{K_w} \frac{\partial p_w}{\partial t} + n \frac{\partial S_w}{\partial t} + \frac{1}{\rho^w} \operatorname{div} \left[ \rho^w \frac{k_{rw} K_r}{\mu^w} (-\operatorname{grad} p_w + \rho^w g \nabla z) \right] = -\frac{\dot{m}}{\rho^w} \quad (3.126)$$

Similarly, the continuity equation of the gaseous phase, i.e. moist air, can be derived in a same manner as that used to derive the mass balance of the liquid water, with the result being

$$(1-n) \left( -\alpha_s \frac{\partial T}{\partial t} \right) + \frac{n}{S_g} \frac{\partial S_g}{\partial t} + \frac{n}{\rho^g} \frac{\partial}{\partial t} \left( \frac{p_g M_g}{\theta R} \right) + \frac{1}{S_g \rho^g} \operatorname{div}(n S_g \rho^g \mathbf{v}^g) = \frac{\dot{m}}{\rho^g S_g} \quad (3.127)$$

However, since

$$\frac{\partial S_g}{\partial t} = -\frac{\partial S_w}{\partial t} \quad (3.128)$$

we have

$$(1-n) \left( -\alpha_s \frac{\partial T}{\partial t} \right) - \frac{n}{S_g} \frac{\partial S_w}{\partial t} + \frac{n}{\rho^g} \frac{\partial}{\partial t} \left( \frac{p_g M_g}{\theta R} \right) + \frac{1}{S_g \rho^g} \operatorname{div}(n S_g \rho^g \mathbf{v}^g) = \frac{\dot{m}}{\rho^g S_g} \quad (3.129)$$

This equation can also be split into two parts due to the species mass balance law defined in Eqns. (3.55) and (3.57). For dry air, Eqn. (3.129) is rewritten

$$\begin{aligned} (1-n) \left( -\alpha_s \frac{\partial T}{\partial t} \right) - \frac{n}{S_g} \frac{\partial S_w}{\partial t} + \frac{n}{\rho^{ga}} \frac{\partial}{\partial t} \left( \frac{p_{ga} M_{ga}}{\theta R} \right) \\ + \frac{1}{S_g \rho^{ga}} \left[ \operatorname{div} j_g^{ga} + \operatorname{div}(n S_g \rho^{ga} \mathbf{v}^g) \right] = 0 \end{aligned} \quad (3.130)$$

For vapor, Eqn. (3.129) is rewritten

$$\begin{aligned}
(1-n) \left( -\alpha_s \frac{\partial T}{\partial t} \right) - \frac{n}{S_g} \frac{\partial S_w}{\partial t} + \frac{n}{\rho^{g^w}} \frac{\partial}{\partial R} \left( \frac{P_{g^w} M_{g^w}}{\theta R} \right) \\
+ \frac{1}{S_g \rho^{g^w}} \left[ \text{div } j_g^{g^w} + \text{div} (n S_g \rho^{g^w} \mathbf{v}^g) \right] = \frac{\dot{m}}{\rho^{g^w} S_g}
\end{aligned} \quad (3.131)$$

Substituting Fick's law, Eqn. (3.104), and the generalized Darcy's law, Eqn. (3.85), into the last two continuity equations for the components of the gaseous phase, we have the following expressions

$$\begin{aligned}
(1-n) \left( -\alpha_s \frac{\partial T}{\partial t} \right) - \frac{n}{S_g} \frac{\partial S_w}{\partial t} + \frac{n}{\rho^{g^w}} \frac{\partial}{\partial R} \left( \frac{P_{g^w} M_{g^w}}{\theta R} \right) \\
+ \frac{1}{S_g \rho^{g^w}} \text{div} \left[ -n S_g \rho^{g^w} \frac{M_{g^w} M_{g^w}}{M_g^2} D_g \text{grad} \left( \frac{P_{g^w}}{P_g} \right) \right] \\
+ \frac{1}{S_g \rho^{g^w}} \text{div} \left[ -n S_g \rho^{g^w} \frac{k_{rg} K_g}{\mu^g} \left( 1 + \frac{b}{p_g} \right) (\nabla p_g - \rho^{g^w} g \nabla z) \right] = 0
\end{aligned} \quad (3.132)$$

and for vapor,

$$\begin{aligned}
(1-n) \left( -\alpha_s \frac{\partial T}{\partial t} \right) - \frac{n}{S_g} \frac{\partial S_w}{\partial t} + \frac{n}{\rho^{g^w}} \frac{\partial}{\partial R} \left( \frac{P_{g^w} M_{g^w}}{\theta R} \right) \\
+ \frac{1}{S_g \rho^{g^w}} \text{div} \left[ -n S_g \rho^{g^w} \frac{M_{g^w} M_{g^w}}{M_g^2} D_g \text{grad} \left( \frac{P_{g^w}}{P_g} \right) \right] \\
+ \frac{1}{S_g \rho^{g^w}} \text{div} \left[ -n S_g \rho^{g^w} \frac{k_{rg} K_g}{\mu^g} \left( 1 + \frac{b}{p_g} \right) (\nabla p_g - \rho^{g^w} g \nabla z) \right] = \frac{\dot{m}}{\rho^{g^w} S_g}
\end{aligned} \quad (3.133)$$

where, again, the first three terms on the left side account for the accumulation of the components known as the *mass concentration* in the gaseous phase, i.e. moist air, the forth term models the diffusion of each component with respect to the mean macroscopic flow of moist air in the porous medium, the last term represents advection of the components with the mean macroscopic flow velocity, and the right

side accounts for the exchange of vapor to the liquid water phase in the porous medium.

### 3.8.2 Enthalpy balance equation for the multiphase medium

Recall the macroscopic energy balance presented in Eqn. (3.76),

$$\eta^\pi \rho^\pi \frac{D^\pi E^\pi}{Dt} = \eta^\pi \rho^\pi R^\pi - \eta^\pi \nabla \cdot \mathbf{q}^\pi + \eta^\pi \sigma^\pi : \nabla \mathbf{v}^\pi + \eta^\pi \rho^\pi (h^\pi + \mathbf{g} \cdot \mathbf{v}^\pi) \quad (3.134)$$

Although the macroscopic energy balance law provides a good basis for understanding the nature of heat transfer in a porous medium, we need to develop a more manageable field equation to solve numerically.

For further development, the internal energy of a phase may be used as a state variable, that is, a variable that depends only on the state of the phase and not on any process that produced that state. Therefore, we are free to define additional state variables that are combinations of existing state variables. These new variables will often make the analysis of a system much simpler. A useful additional state variable is the *specific enthalpy* ( $H$ ) that is defined to be the sum of the specific internal energy ( $E$ ) plus the product of the pressure ( $p$ ) and the specific volume ( $1/\rho$ ). Then we express the energy balance by means of the specific enthalpy  $H$  defined as

$$H^\pi = E^\pi + \frac{p_\pi}{\rho^\pi} \quad (3.135)$$

where  $E^\pi$  is the intrinsic specific energy of a control volume of a phase  $\pi$  and  $\frac{1}{\rho^\pi}$  is the intrinsic specific volume. The differential of the specific enthalpy is then

$$dH^\pi = dE^\pi + p_\pi d\left(\frac{1}{\rho^\pi}\right) + \frac{1}{\rho^\pi} dp_\pi \quad (3.136)$$

By rearranging the terms, it follows that

$$dE^\pi = dH^\pi - p_\pi d\left(\frac{1}{\rho^\pi}\right) - \frac{1}{\rho^\pi} dp_\pi \quad (3.137)$$

Therefore, the left hand side of Eqn. (3.134) can be written

$$\eta^\pi \rho^\pi \frac{D^\pi E^\pi}{Dt} = \eta^\pi \rho^\pi \underbrace{\frac{D^\pi H^\pi}{Dt}}_{(a)} + \eta^\pi p_\pi \underbrace{\frac{1}{\rho^\pi} \frac{D^\pi \rho^\pi}{Dt}}_{(b)} - \eta^\pi \frac{D^\pi p_\pi}{Dt} \quad (3.138)$$

Let us define the terms (a) and (b) of the right hand side of the equation as the following. Since the specific enthalpy is a function of the absolute temperature and the pressure

$$H^\pi = H^\pi(\theta, p_\pi) \quad (3.139)$$

its differential can be written as

$$dH^\pi = \left(\frac{\partial H^\pi}{\partial \theta^\pi}\right)_p d\theta^\pi + \left(\frac{\partial H^\pi}{\partial p_\pi}\right)_\theta dp_\pi \quad (3.140)$$

By using the definition of the specific heat at constant pressure

$$C_p^\pi = \left(\frac{\partial H^\pi}{\partial \theta^\pi}\right)_p \quad (3.141)$$

and the following thermodynamic identity (Hudson 1996)



$$\left( \frac{\partial H^\pi}{\partial p_\pi} \right)_\theta = \frac{1}{p_\pi} \left[ 1 - \frac{\theta^\pi}{\rho^\pi} \left( \frac{\partial \rho^\pi}{\partial \theta^\pi} \right)_{p_\pi} \right] \quad (3.142)$$

Therefore the term (a) of Eqn. (3.138) becomes

$$\frac{D^\pi H^\pi}{Dt} = C_p^\pi \frac{D^\pi \theta^\pi}{Dt} + \frac{1}{\rho^\pi} \frac{D^\pi p_\pi}{Dt} - \frac{\theta^\pi}{\rho^\pi} \left( \frac{\partial \rho^\pi}{\partial \theta^\pi} \right)_{p_\pi} \frac{D^\pi p_\pi}{Dt} \quad (3.143)$$

For the material time derivative of the phase intrinsic density, we expand and divide Eqn. (3.48) by  $\eta^\pi \rho^\pi$

$$\frac{1}{\rho^\pi} \frac{D^\pi \rho^\pi}{Dt} = e^\pi - \text{div } v^\pi - \frac{1}{\eta^\pi} \frac{D^\pi \eta^\pi}{Dt} \quad (3.144)$$

Substituting Eqns. (3.143) and (3.144) into Eqn. (3.138), we have the left hand side of Eqn. (3.134) as the following

$$\begin{aligned} \eta^\pi \rho^\pi \frac{D^\pi E^\pi}{Dt} &= \eta^\pi \rho^\pi C_p^\pi \frac{D^\pi \theta^\pi}{Dt} - \eta^\pi \theta^\pi \left( \frac{\partial \rho^\pi}{\partial \theta^\pi} \right)_{p_\pi} \frac{D^\pi p_\pi}{Dt} \\ &\quad - \eta^\pi p_\pi e^\pi - \eta^\pi p_\pi \text{div } v^\pi - p_\pi \frac{D^\pi \eta^\pi}{Dt} \end{aligned} \quad (3.145)$$

Next, we consider the mechanical energy term  $\sigma^\pi : \nabla v^\pi$  of Eqn. (3.134) as the sum of the deviatoric part and the hydrostatic part

$$\sigma^\pi : \nabla v^\pi = \tau^\pi : \nabla v^\pi - p_\pi \nabla \cdot v^\pi \quad (3.146)$$

If we set the exchange of internal energy (e.g. latent heat) between phases due to phase change  $\rho^\pi R^\pi$  of Eqn. (3.134) as

$$\rho^\pi R^\pi = \rho^\pi e^\pi E^\pi \quad (3.147)$$

then the latent heat  $\rho^\pi e^\pi H^\pi$  of evaporation for the fluid phases are defined by using the definition of the specific enthalpy of Eqn. (3.135) as

$$\rho^\pi e^\pi H^\pi = \rho^\pi e^\pi E^\pi + p_\pi e^\pi \quad (3.148)$$

By substituting the latent heat term and the mechanical energy term into Eqn. (3.134), the macroscopic enthalpy equation is formed

$$\begin{aligned} \underbrace{\eta^\pi \rho^\pi C_p^\pi \frac{D^\pi \theta^\pi}{Dt}}_{(a)} &= \underbrace{\eta^\pi \rho^\pi h^\pi}_{(b)} - \underbrace{\eta^\pi \nabla \cdot \mathbf{q}^\pi}_{(c)} - \underbrace{\rho^\pi e^\pi H^\pi}_{(d)} \\ &+ \underbrace{\eta^\pi p_\pi \frac{D^\pi \eta^\pi}{Dt}}_{(e)} + \underbrace{\eta^\pi \rho^\pi \mathbf{g} \cdot \mathbf{v}^\pi}_{(f)} + \underbrace{\eta^\pi \boldsymbol{\tau}^\pi : \nabla \mathbf{v}^\pi}_{(g)} \\ &+ \underbrace{\eta^\pi \theta^\pi \left( \frac{\partial \rho^\pi}{\partial \theta^\pi} \right)_{p_\pi} \frac{D^\pi p_\pi}{Dt}}_{(h)} \end{aligned} \quad (3.149)$$

where (a) represents the rate of change of heat stored in the phase, (b) is the heat source, (c) represents the internal heat flux in the phase, (d) accounts for the latent heat of evaporation or condensation for the fluid phases, (e) mechanical work by volume fraction change, (f) represents external work done by body forces, (g) is viscous dissipation by the deviatoric stresses, and (h) accounts for mechanical work due to density variation caused by temperature changes.

For further development, we assume that a state of local thermodynamic equilibrium in all the phases exists. This means that the temperatures of the phases are equal at each point (or REV) in the multi-phase system

$$\theta^s = \theta^w = \theta^g \quad (3.150)$$

Also, the terms related to viscous dissipation and mechanical work done by the density variation and the volume fraction change are assumed to be negligible.

Recalling Fourier's law and the definition of material time derivative, we find the macroscopic enthalpy equation

$$\begin{aligned} (\rho C_p)_{eff} \frac{\partial T}{\partial t} + (nS_w \rho^w C_p^w v^w + nS_g \rho^g C_p^g v^g) \cdot \text{grad } T \\ - \text{div} (\kappa_{eff} \text{ grad } T) = -\dot{m} \Delta H_{vapor} \end{aligned} \quad (3.151)$$

where

$$\begin{aligned} (\rho C_p)_{eff} &= (1-n) \rho^s C_p^s + nS_w \rho^w C_p^w + nS_g \rho^g C_p^g \\ \kappa_{eff} &= (1-n) \kappa_p^s + nS_w \kappa_p^w + nS_g \kappa_p^g \\ \Delta H_{vapor} &= H^{g^w} - H^w \end{aligned} \quad (3.152)$$

The temperature difference,  $T = \theta - \theta_0$ , is substituted for the absolute temperature  $\theta$  in all derivatives where the reference temperature  $\theta_0$  is fixed.

A physical interpretation of Eqn. (3.151) can be given that the first term on the left represents rate change of heat stored in the multiphase medium, the second term accounts for heat flow by convection, the third term represents the internal heat flux by conduction, and the term on the right hand side represents the enthalpy change due to evaporation of the liquid water.

### 3.9 Initial and Boundary Conditions

The initial and boundary conditions for a partially saturated porous medium subjected to high temperature are now considered. The initial conditions describe the

field variables, i.e. displacements, water pressures, gas pressures, degrees of water saturation (or degrees of gas saturation), and temperatures at time zero

$$u = u_0 \quad p_w = p_w^0 \quad p_g = p_g^0 \quad S_w = S_w^0 \quad T = T_0 \quad \text{in } \Omega \text{ and on } \partial\Omega \quad (3.153)$$

where heat and mass transfer coupled with mechanical displacements occurs in a partially saturated porous material occupying the volume  $\Omega$  with a closed surface boundary  $\partial\Omega$  over a time interval  $I = [0, T]$

We introduce the Dirichlet type of boundary conditions, i.e.

$$\begin{aligned} u &= \hat{u} \quad \text{on } \partial\Omega_u^1 \\ p_w &= \hat{p}_w \quad \text{on } \partial\Omega_w^1 \\ p_g &= \hat{p}_g \quad \text{on } \partial\Omega_g^1 \\ T &= \hat{T} \quad \text{on } \partial\Omega_T^1 \end{aligned} \quad (3.154)$$

For the Neumann type, first the traction  $\bar{T}$  boundary condition for the mechanical stresses  $\sigma_m$  can be written

$$\sigma_m \cdot \mathbf{n} = \bar{T} \quad \text{on } \partial\Omega_u^2 \quad (3.155)$$

where  $\mathbf{n}$  is a unit normal vector to the boundary surface and the respective flux boundary conditions of each phase, i.e. for the water flux

$$\left[ \begin{aligned} &\rho^w \frac{k_{rw} K_t}{\mu^w} (-\nabla p_w) + \rho^{gw} \frac{k_{rg} K_g}{\mu^g} \left( 1 + \frac{b}{p_g} \right) (-\nabla p_g) \\ &+ \rho^{gw} \frac{M_{ga} M^{gw}}{M_g^2} D_g \operatorname{grad} \left( \frac{p_{gw}}{p_g} \right) \end{aligned} \right] \cdot \mathbf{n} = q^w + q^{gw} \quad \text{on } \partial\Omega_w^2 \quad (3.156)$$

for the gas flux

$$\left[ \rho^{ga} \frac{k_g K_g}{\mu^g} \left( 1 + \frac{b}{p_g} \right) (-\nabla p_g) - \rho^{ga} \frac{M_{ga} M_{gw}}{M_g^2} D_g \text{grad} \left( \frac{p_{ga}}{p_g} \right) \right] \cdot \mathbf{n} = q^{ga} \text{ on } \partial\Omega_g^2 \quad (3.157)$$

and for the heat flux

$$(-\kappa_{eff} \text{grad } T) \cdot \mathbf{n} = q^T \text{ on } \partial\Omega_T^2 \quad (3.158)$$

where  $\partial\Omega = \overline{\partial\Omega^1} + \partial\Omega^2$  and  $q$  is the imposed mass (or heat) flux normal to the boundary. These equations are the natural boundary conditions for the macroscopic balance equations, the solution to which is obtained via a ‘weak’ formulation (e.g. using the weighted residual methods) of the problem as is done in Chapter 6.

In heat flux boundary conditions, three basic mechanisms are involved in heat transfer between boundaries from one body to another: conductive, convective, and radiant heating. If we attach a metal plate to another hot plate, we eventually notice that the attached plate becomes warmer. This form of heat transfer is called *conduction*. In a warm fluid flowing in a pipe, heat of the fluid is transferred by the mechanism called *convection* to the pipe. In contrast to the mechanisms of conduction and convection, where heat transfer through a medium is involved, heat may also be transferred by electromagnetic waves that are propagated as a result of a temperature difference. This is called *radiation*.

Radiation is a significant mode of heat transfer in building fire environments, it is particularly important to modeling enclosure fires. Besides, radiation tends to dominate the other two modes of heat transfer in room environments where high temperatures are attained with fires or hot smoke layers. Therefore, modeling of

radiation boundary conditions between a heat source and a body is of particular interest.

In a building fire scenario, the conductive heat flux boundary condition is considered in the mathematical expression of heat flux boundary condition in Eqn. (3.158). Two basic numerical approaches can be considered for modeling the radiant boundary conditions (Consolazio et al. 1998) (1) computing heat fluxes in boundary elements directly from the heat source, and (2) converting the radiant heat fluxes on the boundaries into a conductive boundary condition. The latter approach is adopted in this research. Thus, in the mathematical expression, only conductive boundary condition is included hereby. Additional details describing the second approach for computing radiative heat transfer between the bounding surfaces of concrete and point source fires are obtained from Patankar (1980).

## CHAPTER 4

### NUMERICAL MODELING OF TRANSPORT PHENOMENA IN REINFORCED CONCRETE EXPOSED TO ELEVATED TEMPERATURES

The objective of this chapter is to develop a finite difference model that simulates coupled heat and mass transport phenomena in reinforced concrete exposed to rapid heating conditions such as fires. A mathematical and computational model to simulate the multi-dimensional thermo-hydrological response of reinforced concrete structural elements is presented. Key parameters that describe thermo-hydrological material behavior of concrete are also presented. Effects of steel reinforcements on coupled heat and mass transfer, which can be potentially associated with concrete spalling, are discussed. The domain and time history distributions of temperature, pore pressure, and degree of saturation are illustrated as predicted under various thermal-loading conditions.

#### 4.1 Overview

The lower permeability of HSC limits moisture movement in the heated concrete and results in the development of large internal pore pressures (Kodur 1997, Consolazio et al. 1998, Kodur 1999). In addition, material properties (e.g., material strength and thermal expansivity) and mechanical behavior (e.g., stress and strain fields) can be significantly influenced by the thermodynamic state—as characterized by variables such as pore-pressure, temperature, and saturation—of reinforced concrete elements.

Thus, the goal in this chapter is to quantify thermodynamic state variables for concrete under a variety of different heating conditions. By quantifying state

variables, greater insight into the causes of phenomena such as explosive spalling can be obtained. Focus in this chapter is placed primarily on transient heat and mass transfer occurring inside heated concrete rather than on prediction of resulting stresses—the topic of later chapters. In addition to insight into flow characteristics of HSC, the effects of steel reinforcement on hydro-thermal behavior of concrete are also investigated in order to quantitatively identify the influence of heterogeneity on the thermodynamic state of the system. For example, steel reinforcement can create impermeable regions that alter the migration of moisture and water vapor through the heated concrete matrix. An analytical model including key flow parameters for high-strength concrete that simulates transient fluids (i.e., water vapor and liquid water) and heat flow is therefore developed in this chapter.

Formulating realistic mathematical representations of dominant physical phenomena is a primary component of the model development process described here. The TOUGH2 (Pruess 1991) code—a general purpose finite difference numerical simulator for multi-phase fluid and heat flow—is used as the basis for numerical modeling. The mathematical formulation implemented in TOUGH2 consists of mass and thermal energy balance equations that are used to solve for three primary variables pore pressure, degree of gas saturation, and temperature. However, in this study modifications are made to the code so that important flow characteristics specific to concrete behavior are properly taken into consideration. For example, *relative permeability functions* and *slip flow relationships* are developed specifically for cement-based materials and are implemented into TOUGH2. Implementation of these new features is necessary in order to properly describe the flow of the various



fluid phases that migrate inside heated concrete. The proposed model is capable of accounting for the simultaneous movement of both the gaseous and liquid phases, their transport of heat, and phase transitions between liquid water and gaseous water vapor.

## 4.2 Governing Equations

Having introduced the mass- and energy balance equations in generic form in Chapter 3, we now review the governing equations of coupled heat and mass transport to be solved for three primary variables pressure, temperature, and saturation. The mass- and energy-balance equations can be expressed in the integral form of

$$\underbrace{\frac{d}{dt} \int_U M^{(\gamma)} d\Omega}_{(a)} - \underbrace{\oint_{\partial U} F^{(\gamma)} \cdot \mathbf{n} d\Gamma}_{(b)} - \underbrace{\int_U q^{(\gamma)} d\Omega}_{(c)} = 0 \quad (4.1)$$

( $\gamma = 1$ : water;  $\gamma = 2$ : air;  $\gamma = 3$ : heat)

where part-*a* represents the rate of change of mass accumulation for fluid phases (if  $\gamma=1$  or 2) or the rate of change of heat accumulation for the multiphase continuum ( $\gamma = 3$ ), part-*b* represents the mass flux of a fluid phase ( $\gamma=1$  or 2) or the heat flux ( $\gamma = 3$ ) into  $U$  through surface area  $\partial U$ , and part-*c* represents the external supply of energy attributable to gravitational effects.

More specifically, the mass accumulation term  $M^{(\gamma)}$  in Eqn. (4.1) can be expressed

$$M^{(\gamma)} = n \sum_{\pi=w,g} S_{\pi} \rho^{\pi} X_{\pi}^{(\gamma)} \quad (4.2)$$

where the water specie can be written in terms of liquid and gas phases as

$$M^{(1)} = n \sum_{\pi=w,g} S_{\pi} \rho^{\pi} X_{\pi}^{(1)} = \underbrace{n S_w \rho^w X_w^{(1)}}_{(a)} + \underbrace{n S_g \rho^g X_g^{(1)}}_{(b)} \quad (4.3)$$

That is, the mass accumulation of water species is equal to the sum of masses of liquid water and water vapor. For the air specie,

$$M^{(2)} = n \sum_{\pi=w,g} S_{\pi} \rho^{\pi} X_{\pi}^{(2)} = n S_g \rho^g X_g^{(2)} \quad (4.4)$$

where  $n$  is the total porosity,  $S_{\pi}$  is the degree of saturation in each phase,  $\rho^{\pi}$  is the intrinsic phase density, and  $X_{\pi}^{(\gamma)}$  represents the mass fraction of component  $\gamma$  in phase  $\pi$ , which can be written

$$X_{\pi}^{(\gamma)} = \frac{\rho^{\gamma}}{\rho^{\pi}} \quad (4.5)$$

The heat accumulation term accounts for thermal energy stored in the multiphase continuum,

$$M^{(3)} = (1-n) \rho^s C_p^s T + n \sum_{\pi=w,g} S_{\pi} \rho^{\pi} E_{\pi} \quad (4.6)$$

where  $C_p^s$  is the specific heat of the porous matrix and  $E_{\pi}$  represents the specific internal energy of each water phase  $\pi$  ( $\pi = w, g$ )

The mass flux term,  $F^{(\gamma)}$ , in Eqn. (4.1) is a sum of the mass fluxes summed over each phase

$$F^{(r)} = \sum_{\pi=w,g} F_{\pi}^{(r)} \quad (4.7)$$

Based on a generalized Darcy's law modified for multi-fluid flow and slip flow, the mass flux of water species ( $\gamma = 1$ ) can be expressed as

$$\begin{aligned} F^{(1)} &= F_w^{(1)} + F_g^{(1)} \\ &= -K \frac{k_{rw}}{\mu^w} \rho^w X_w^{(1)} (\nabla p_w - \rho^w g \nabla z) - K \frac{k_{rg}}{\mu^g} \rho^g X_g^{(1)} \left( 1 + \frac{b}{p_g} \right) (\nabla p_g - \rho^g g \nabla z) \end{aligned} \quad (4.8)$$

and the mass flux of dry air ( $\gamma = 2$ ) can be written in the form

$$F^{(2)} = -K \frac{k_{rg}}{\mu^g} \rho^g X_g^{(2)} \left( 1 + \frac{b}{p_g} \right) (\nabla p_g - \rho^g g \nabla z) - \rho^g \tau D_g \text{grad} (X_g^{(2)}) \quad (4.9)$$

where  $K$  is the intrinsic permeability,  $k_{r\pi}$  is the relative permeability to phase  $\pi$ ,  $\mu^\pi$  is the dynamic viscosity,  $\tau$  is the tortuosity factor, and  $D_g$  is the effective dispersion-diffusion coefficient for diffusing dry air in the gaseous water phase (i.e., *Fick's law of binary diffusion*).

The total heat flux term,  $F^{(3)}$ , in Eqn. (4.1) also consists of two parts, heat conduction through the multiphase continuum as a whole and heat convection by mass fluxes of the fluid phases (liquid water and moist air)

$$F^{(3)} = -\kappa_{avg} \text{grad} T + \sum_{\substack{\gamma=1,2 \\ \pi=1,2}} H_{\pi}^{(\gamma)} F_{\pi}^{(\gamma)} \quad (4.10)$$

where  $H_{\pi}^{(\gamma)}$  represents the specific enthalpy of component  $\gamma$  in phase  $\pi$ ,  $\kappa_{avg}$  is the volume-averaged thermal conductivity tensor for the multiphase medium

$$\kappa_{avg} = \sum_{\pi} \eta_{\pi} \kappa_{\pi} \quad \pi = s, w \text{ and } g \quad (4.11)$$

where  $\eta^{\pi}$  is the *volume fraction* of phase  $\pi$ , and  $\kappa_{\pi}$  is the thermal conductivity tensor of phase  $\pi$ .

### 4.3 Discretization of Integrated Finite Difference Method

The integral mass- and energy-balance equations in Eqn. (4.1) are solved directly from the integral formulation known as the ‘*integrated finite difference method*’ (IFDM) (Narasimhan and Witherspoon 1976). Consider two volume elements  $V_l$  and  $V_m$  with the interface surface segment  $A_{lm}$  where the distances between the centroids of the volumes and the interface are denoted by  $D_l$  and  $D_m$ , shown as Figure 4-1.

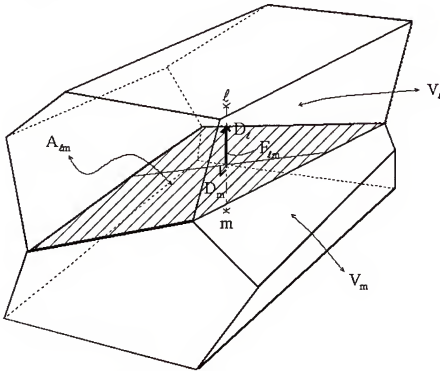


Figure 4-1 A schematic sketch of spatial discretization

The mass flux of the water components ( $\gamma = 1$ ) can be expressed in discretized form as

$$\begin{aligned} F_{\ell m}^{(1)} = & -K_{w,\ell m}^e \left( \frac{k_{rw} \rho^w X_w^{(1)}}{\mu^w} \right)_{\ell m} \left[ \frac{P_{w,\ell} - P_{w,m}}{D_{\ell m}} \right] \\ & - K_{g,\ell m}^e \left( \frac{k_{rg} \rho^g X_g^{(1)}}{\mu^g} \right)_{\ell m} \left[ \frac{P_{g,\ell} - P_{g,m}}{D_{\ell m}} \right] \end{aligned} \quad (4.12)$$

where the subscripts ( $\ell m$ ) indicate the averaged value at the interface between volume elements  $V_\ell$  and  $V_m$  and is based on the macroscopically *volume-averaged* quantities within  $V_\ell$  and  $V_m$ ,  $K_{\pi,\ell m}^e$  represents the weighted value of the intrinsic permeability to phase  $\pi$  when the two volume elements are composed of different materials or composed of the same material but which are partially saturated to different degrees for phase  $\pi$ ,  $p_{\pi,\ell}$  represents the average pressure of phase  $\pi$  in volume element  $V_\ell$ , and  $D_{\ell m}$  represents the distance between the centroids of volume elements  $V_\ell$  and  $V_m$ . Gravitational effects are omitted because the focus here is on localized behavior (e.g. spalling) and gravitational effects are not of significant importance in such situations.

The *effective* permeability to water  $K_{w,\ell m}^e$  at the interface between volume elements  $V_\ell$  and  $V_m$  is defined as (Narasimhan and Witherspoon 1976)

$$K_{w,\ell m}^e \equiv \frac{K_{w,\ell} K_{w,m} (D_\ell + D_m)}{K_{w,\ell} D_m + K_{w,m} D_\ell} \quad (4.13)$$

whereas the *effective* permeability to moist air is defined as

$$K_{g,\ell m}^e \equiv \frac{K_{g,\ell} K_{g,m} (D_\ell + D_m)}{K_{g,\ell} D_m + K_{g,m} D_\ell} \quad (4.14)$$

where gas permeability within each volume element, including Klinkenberg's effect, is

$$\begin{aligned} K_{g,\ell} &= K_g \left( 1 + \frac{b}{p_{g,\ell}} \right) \\ K_{g,m} &= K_g \left( 1 + \frac{b}{p_{g,m}} \right) \end{aligned} \quad (4.15)$$

Mass flux of the dry air can be expressed in discretized form as

$$F_{\ell m}^{(2)} = -K_{g,\ell m} \left( \frac{k_{rg} \rho_g^g X_g^{(2)}}{\mu^g} \right)_{\ell m} \left[ \frac{p_{g,\ell} - p_{g,m}}{D_{\ell m}} \right] - \rho_{\ell m}^g \tau_{\ell m} D_{g,\ell m} \left( \frac{X_{g,\ell}^{(2)} - X_{g,m}^{(2)}}{D_{\ell m}} \right) \quad (4.16)$$

where  $\rho_{\ell m}^g$  is an averaged mass density of the gaseous phase in volume elements  $V_\ell$  and  $V_m$ ,  $\tau_{\ell m}$  is an average value of the tortuosity factor,  $D_{g,\ell m}$  is an average value of the effective dispersion-diffusion coefficient, and  $X_{\pi,\ell}^{(\gamma)}$  represents the mass fraction of component  $\gamma$  in phase  $\pi$  within volume element  $V_\ell$ .

Similarly, for the heat flux term  $F^{(3)}$  in Eqn. (4.1), the heat flux can be discretized as

$$F_{\ell m}^{(3)} = -\kappa_{avg,\ell m}^e \left[ \frac{T_\ell - T_m}{D_{\ell m}} \right] + \sum_{\pi=1,2} H_{\pi,\ell m} F_{\pi,\ell m} \quad (4.17)$$

where  $\kappa_{avg,\ell m}^e$  is the harmonic mean (Patankar 1980) of conductivity coefficients

$\kappa_{avg,\ell}$  and  $\kappa_{avg,m}$ , and is denoted the “effective” conductivity,  $T_\ell$  and  $T_m$  are

temperatures in volume elements  $V_\ell$  and  $V_m$  at a local thermodynamic equilibrium state, and  $H_{\pi,lm}$  represents an averaged value of the sum of specific enthalpies of all the components (or species)  $\gamma$  in phase  $\pi$ .

#### 4.4 Key Parameters of Fluid and Heat Flow in Concrete

In modeling simultaneous flow of heat and fluids through concrete, the effects of moisture movement on key flow parameters such as permeability and conductivity must be included. For example, permeability to moist air in the transport process is affected by presence of liquid water in pores. Also, thermal conductivity of the concrete is affected by degree of water saturation during the transient hydro-thermal process. While TOUGH2 (Preuss 1991) is an excellent tool for the numerical analysis of the continuum phenomena of mass and heat transfer in concrete, reliable data for key parameters used in the constitutive models (e.g. flow properties of a particular phase) are still needed to make valid predictions by simulation. This study makes use of hydro-thermal properties collected from field tests reported in literature.

##### 4.4.1 Relative permeability of concrete

The model presented here accounts for the involvement of fluid phases in heat transfer that includes, (1) flow of both liquid and gas being accompanied by heat convection, and (2) evaporation of free water content associated with latent heat. Temperature data obtained from analyses including these effects are thought to be more accurate than similar data predicted by traditional thermal analysis models which often do not account for the changes of heat conductivity introduced by changes in degrees of water saturation.

We define the permeability as an intrinsic permeability (also called absolute permeability) for use in numerical simulations. Although rigorous experiments by many researchers have been conducted to measure the permeability of concrete to either gas or liquid (Loughborough 1966, Hope and Malhotra 1984, Nagataki et al. 1985, McVay and Rish 1995, Reinhardt and Dinku 1996, Sugiyama et al. 1996), only a limited number of studies (Bamforth 1987a and b, Whiting 1988, Dhir et al. 1989) were found to provide data for both liquid and gas permeability tested with the same concrete mixtures. Additionally, consistency in preparing the samples (in particular, curing procedures and periods of time are important in air permeability measurement that is substantially reduced by moisture content (Reinhardt and Dinku 1996, Nagataki et al. 1985, Hope and Malhotra 1984)) with a similar composition of the mixture including  $W/(C+P)$  and  $Agg/(C+P)$  was the primary consideration in collecting data for the key parameters. Therefore, the parameters used in this study may not characterize all possible concrete types, but they can be considered to be representative of normal-weight HSC often found in practice.

Because the macroscopic permeability of concrete is a function of both the solid matrix *and* the particular fluid used to experimentally measure the permeability (Klinkenberg 1941, Nagataki et al. 1985, Dhir et al. 1989, McVay and Rish 1995), neither gas permeability nor liquid permeability is believed to be the *single* absolute measure of the intrinsic permeability of the solid skeleton of concrete. Thus, for a complete description, fluid flows in concrete will be characterized by *three* parameters the intrinsic gas permeability  $K_g$ , the intrinsic water permeability  $K_w$ , and the Klinkenberg's constant  $b$ . These three parameters taken in conjunction can



be used to fully characterize the single-phase flow of either liquid or gas through concrete. Consequently, fluid flow rates computed by using these three intrinsic flow parameters of concrete are significantly different from those predicted by using a single-valued permeability in a transient heat and mass transfer analysis. Pore pressure development (in locations and time) has been found to be affected and determined mainly by the assessment of the fluid flow rates.

The flows that occur in a partially saturated concrete exposed to nonisothermal conditions involve two distinct fluid phases (e.g. liquid water and gaseous steam) permeating simultaneously through the porous network. Since the presence of the liquid phase can reduce the permeability of the concrete to the gas phase and vice versa, we employ a postulate commonly used to allow for this interaction as

$$\begin{aligned} k_{rg} &= RP_g(n, S_g) \\ k_{rw} &= RP_w(n, S_w) \end{aligned} \quad (4.18)$$

where  $k_{r\pi}$  stands for the *relative permeability* (RP) of the concrete to phase  $\pi$  at the degree of fluid saturation  $S_\pi$ ,  $n$  represents the porosity, and the functions  $RP_\pi(n, S_\pi)$  are called *relative permeability functions* (RPF), which obey the bounds  $0 \leq RP_\pi(n, S_\pi) \leq 1$ .

Using the relationship  $S_g = 1 - S_w$ , a RP of concrete to gas has been developed as a function of the degree of liquid water saturation ( $S_w$ ) and an empirical parameter ( $\lambda$ ) determined by the porosity  $n$  of concrete. Experimental data (Whiting 1988, Cabrera and Ghoddoussi 1994, Baroghel-Bouny and Chaussadent 1996) and sorption

isotherm concept (Hansen 1989) were used by the author to develop the following relative permeability function

$$RP_g(S_w, \lambda) = 10^{S_w^\lambda} - 10^\lambda S_w \quad (4.19)$$

where

$$\lambda = 0.05 - 22.5n \quad (4.20)$$

Similarly, for a RPF of concrete to liquid water, the ratio of the water permeability to the gas permeability has been combined with an assumed mirror image of the RPF for gas to obtain

$$RP_w(S_w) = \alpha RP_g(1 - S_w) \quad (4.21)$$

where

$$\alpha = \frac{K_w}{K_g} \quad (4.22)$$

Due to the considerable difficulties involved in performing and interpreting two-phase (water-air) RP, very little data is available to construct the RP of concrete to water. However, a remarkable resemblance in the RP-saturation relations in two-phase (air-water) and three-phase (air-water-oil) systems of soils is found in both shape and variation with respect to water saturation (Lenhard and Parker 1987, Burdine 1953, Parker et al. 1987). Experimental data from the literature (Burdine 1953, Parker et al. 1987) also indicate that the proposed trend found between porosity

and sensitivity of  $RP$  to  $S_w$  is consistent with that found in pore size distribution varying with concrete types (Figure 4-2).

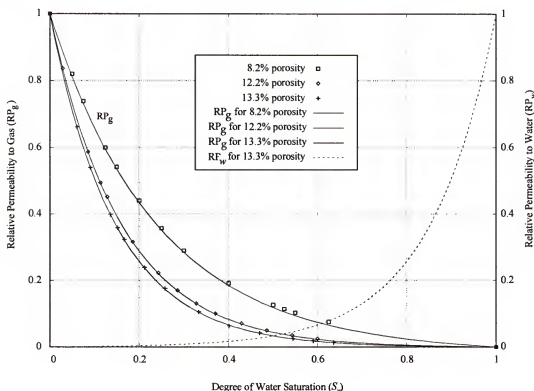


Figure 4-2 Relative permeability functions for the gas phase

Concrete as a porous medium is assumed to have a similar  $RP$ -saturation relation to that of soils. Based on this assumption, the shape of the curve of  $RP$  to gas can be mirrored to construct that for water. However, the author recognizes limitation of the proposed  $RP_w$  (1) while the decrease in relative air permeability is more pronounced, relative water permeability may mildly increase in concrete with water saturation, and (2) the residual degree of saturation is not considered in the proposed  $RP_w$  whereas relative water permeability of soil, experimentally measured, becomes zero if  $S_w$  becomes lower than the residual degree of saturation.

The relative gas permeability curves generated by the  $RP_g$  function above are plotted for various values of porosity in Figure 4-2 along with the data points used in the development. Figure 4-3 presents a comparison between Eqn. (4.19) and experimental results presented by Jacobs (1998).

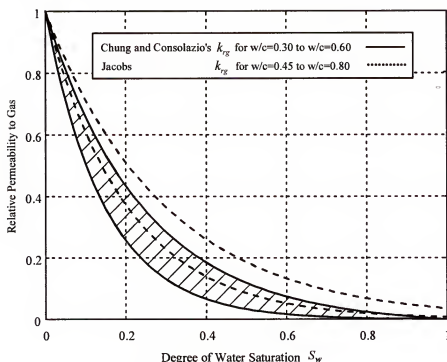


Figure 4-3 Comparison of RP functions for gas flow

By conducting gas permeability tests on concrete specimens at various states of partial liquid saturation, Jacobs determined RP values for gas flow (i.e. values of  $RP_g$  as a function of  $S_w$ ). Upper and lower bound curves for Jacob's results for concrete specimens that had W/C ranging approximately from 0.45 to 0.8, are shown in Figure 4-3. For comparison, the range of values predicted by Eqn. (4.19) for concrete mixes having  $W/(C+P)$  ranging approximately from 0.3 to 0.6, is also shown as a hatched region in Figure 4-3. While the two sets of curves are not identical, their general form

is in good agreement. Since Eqn. (4.19) has been developed using experimental data sources other than Jacobs' results, the agreement shown in Figure 4-3 suggests a degree of validity in the relationships presented both herein and by Jacobs (1998).

#### 4.4.2 Slip flow constant of concrete

In very low permeability materials such as HSC, the slip flow phenomenon known as *Klinkenberg's effect*, can be dominant. As Eqn. (4.15) indicates, permeability of concrete to gas flow can be much larger than the *intrinsic* gas permeability  $K_g$  if a material constant  $b$  (i.e., *Klinkenberg's constant*) is significant.

A functional relationship between  $b$  and the gas permeability  $K_g$  of the concrete in Eqn. (4.15) as shown in Figure 4-4 has been developed based on (1) permeability test data published by Whiting (1988) and Klinkenberg (1941) and (2) based on relationships between the gas permeability and the water permeability for concrete presented by Dhir et al. (1989)

$$b = e^{(-0.5818 \ln(K_g) - 19.1213)} \quad (4.23)$$

where  $K_g$  is in units of  $\text{m}^2$  and  $b$  is in units of atmospheres.

Dhir's data were measured from cover layers of concrete, which might not be capable of characterizing bulk concrete. However, the primary concern in this dissertation is on pressure and temperature profiles near the surface of the concrete where thermal spalling occurs. Thus, Dhir's relationship may not be universally used for characterizing concrete at all depths of structural elements, but it is well suited for the situations considered here.

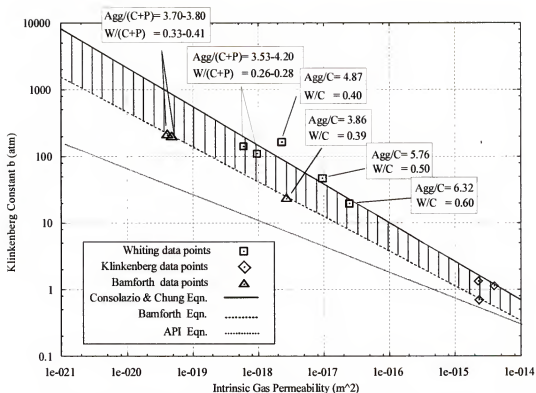


Figure 4-4 Slip flow constant vs. the gas permeability of concrete

For comparison, the slip flow values predicted by Bamforth's equation (Bamforth 1987) with data only for normal weight concrete mixes having  $W/(C+P)$  ranging approximately from 0.33 to 0.41 and  $Agg/C$  ranging approximately from 0.37 to 0.40 are also shown in Figure 4-4. One can see favorable agreement in the range of a concrete mixture having both a low  $W/C$  and a high  $W/C$ . For modeling purposes, an approximate range of slip flow constants (shown as a hatched region in Figure 4-4) is proposed

$$b = (1.635E-8) \cdot (K_g)^{-0.5227} \quad (4.24)$$

where Eqn. (4.24) was developed by Bamforth (1987) and used as the lower bound in Figure 4-4. For comparison, an equation for soils given by the American Petroleum Institute (1952) is also plotted.

#### 4.4.3 Volume-averaged quantities for thermal properties of concrete

Thermal conductivity and diffusivity of concrete are generally affected by changes in the type and quantity of aggregates. The concrete considered in this study is assumed to be made of siliceous type of aggregates such as quartzite or sand stone with  $\text{Agg}/(\text{C}+\text{P}) = 3.7$  to  $6.2$  and  $\text{W}/(\text{C}+\text{P}) = 0.26$  to  $0.6$ .

Based on a spatial volume averaging theory, the volume-averaged thermal conductivity used in Eqn. (4.11), which corresponds to real laboratory measurable quantities, are assumed to be a linear function of the degree of water saturation only (Pruess 1991)

$$\kappa_{avg}(S_w) = \kappa_{avg}(S_w = 0) + S_w \{ \kappa_{avg}(S_w = 1) - \kappa_{avg}(S_w = 0) \} \quad (4.25)$$

where  $\kappa_{avg}(S_w)$  represents the volume-averaged thermal conductivity. Thermal conductivity of concrete is assumed to be a relatively weak function of temperature, but may be affected significantly by moisture content.

However, the author recognizes that temperature significantly influences other properties of concrete (Bažant and Kaplan 1996). Particularly, an increase in porosity and the extent of dehydration are mainly responsible for a sudden jump in magnitude of permeability and a noticeable decrease in conductivity of concrete at elevated temperatures. Bažant (1997) explained that at elevated temperatures, the micropores such as gel pores of molecular dimensions that are inaccessible in an ambient

condition become accessible to the fluids. Rapid increase of the permeability (by an order or two of magnitude increase) can be observed without noticeable change of the porosity. Also, microcracks initiated by differential thermal expansion occurring at the interfaces between cement paste (which shrinks as it is heated) and aggregates expanding during fire will cause opening of more continuous channels for fluid flow, which can result in a substantial increase of the porosity. These phenomena can also contribute to a significant increase in the permeability of concrete to both moist air and liquid water (Samaha and Hover 1992).

More importantly, the effects of moisture movement on the permeability and conductivity of concrete are considered in modeling simultaneous flow of heat and fluids. For example, relative permeability to moist air in the hydro-thermal processes involved in the formation of pressure driven moisture layers known as “*moisture clog formation*” (Harmathy 1964), is coupled with thermal conductivity of concrete between quasi-saturated and de-saturated zones.

Thus, the presented model can predict the fluid phases’ involvement with heat transfer that includes (1) the fluids (moist air and liquid water) being driven through concrete by pressure gradient and being accompanied by heat convection and (2) evaporation of free water content associated with latent heat of water. Hydro-thermal properties used here for structural steel and two types of concrete are obtained from the field test data reported in literature (Dhir et al. 1989, Burg and Ost 1994, Scanlon and McDonald 1994) and are given in Table 4-1. Ongoing experimental research in measuring concrete permeability will be used to extend Eqn. (4.19) to include the temperature dependency of the RP. In addition, numerical implementation of thermal



conductivity of concrete as a function of temperature should be included in the future research.

Table 4-1 Material properties of concrete and steel used in numeric simulations

Material Property	Structural Steel	Concrete I	Concrete II
Porosity	N/A	13.3%	8.2%
Conductivity (wet)	52.0 W/m-C	2.9 W/m-C	2.6 W/m-C
Conductivity (dried)	52.0 W/m-C	1.7 W/m-C	2.0 W/m-C
Expansivity	12.0E-6 1/C	6.5E-6 1/C	8.5E-6 1/C
Emissivity	N/A	0.8	0.88
Saturated unit weight	7850 kg/ m <sup>3</sup>	2200 kg/ m <sup>3</sup>	2400 kg/ m <sup>3</sup>
Specific heat	209 J/kg-C	921 J/kg-C	921 J/kg-C
Intrinsic gas permeability	N/A	2.24E-17 m <sup>2</sup>	6.34E-19 m <sup>2</sup>
Intrinsic liquid permeability	N/A	8.49E-19 m <sup>2</sup>	4.82E-21 m <sup>2</sup>
Klinkenberg's Constant	N/A	2.44 MPa (24.1 atm.)	19.45 MPa (192.0 atm.)
28 Day Compressive Strength	N/A	60 MPa	90 MPa

By having established the key material parameters and constitutive equations used in the governing flow equations, several example simulations will be presented to study thermodynamic states developed in concrete exposed to fire. In the following sections, we will first investigate initial degree of saturation of concrete that plays a critical role in prediction of pore pressure and temperature at high temperatures. Then we will validate the numerical model developed in this study by experimental test results reported by Consolazio et al. (1998) before presenting example simulation results.

#### 4.5 Calculation of Initial Conditions

Initial conditions for example problems presented in this study are assumed to be uniform conditions of pressure, temperature, and saturation throughout the entire

flow domain at the initial state. Initial pressure and temperature inside the flow domain is assumed to be equal to the atmospheric pressure and a temperature of 20 °C, respectively.

Variability of environmental conditions affecting concrete in situ and a variety of concrete mixtures are taken into consideration to determine the initial conditions of concrete at ambient conditions. Initial degrees of saturation were evaluated for two types of concrete (Table 4-1) concrete I with  $W/C=0.5-0.6$  and  $Agg/C=5.0-6.0$  and concrete II with  $W/(C+P)=0.28-0.3$  and  $Agg/(C+P)=3.8-4.2$ , in an ambient condition of 60 % RH at a temperature of 20 °C.

The moisture content in a partially saturated concrete can be computed using sorption isotherms of concrete as a percentage of the free moisture content. Using the porosity,  $W/(C+P)$ ,  $Agg/(C+P)$ , and a saturated unit weight of the concrete, the water content of the *saturated concrete* is computed and subsequently converted into a “water content by mass of dried hardened cement paste (HCP)” (Baroghel-Bouny and Chaussadent 1996). This step of converting the “normal” mass water content into one that is referenced with respect to only the portion of the concrete mass attributable to the cement paste was performed so that the concrete isotherms of Baroghel-Bouny and Chaussadent (1996) could be used.

Taking saturated concrete having  $S_w = 1.0$  and oven-dried (until less than 3% change in weight is observed) concrete having  $S_w = 0.0$ , an intermediate value of degree of saturation can be computed as a percentage of the saturated moisture content by using the weight differences between the saturated and dry concrete

$$S_w = \frac{w_{rh;hcp}}{w_{sat;hcp}} \times 100 \quad (4.26)$$

where  $S_w$  represents the degree of saturation,  $w_{sat;hcp}$  = water content (by mass of HCP) of concrete in a saturated condition, and  $w_{rh;hcp}$  = water content when the concrete is air-dried at a particular RH level at the temperature of 20 °C.

For example, consider a concrete sample made of concrete I in Table 4-1 having a porosity of 0.133 (13.3%), a  $W/(C+P)=0.5$ , an  $Agg/(C+P)=5.8$ , and a fully saturated water content of  $w_{sat;hcp} = 0.1989$  (19.89%). Assume that the concrete member has reached hydro-thermal equilibrium at approximately 60~65% relative humidity at the temperature of 20 °C. Isotherm data from experiments by Baroghel-Bouny and Chaussadent (1996) can be used to find that the water content is approximately 0.334 (33.4%) by mass of HCP. Using Eqn. (4.26) and the concrete isotherms, a degree of initial saturation for the NSC is approximated as  $S_w = 0.4$  in a range of 60-65% RH. Similarly, for a concrete sample having a porosity of 0.082 (8.2%), a  $W/(C+P)=0.28$ , an  $Agg/(C+P)=3.8$ , and a fully saturated water content of  $w_{sat;hcp} = 0.10$  (10%), a degree of initial saturation for the higher porosity concrete is approximated as  $S_w = 0.6$  in a range of 60-65% RH.

#### 4.6 Comparison of Numerical Results with Experimental Data

Before conducting simulations by the proposed modeling techniques, validation against published data for saturated, but unreinforced, mortar exposed to severe heating are performed. A 2-D simulation is performed and results are compared to the

experimental data reported by Consolazio et al. (1998). The original 2-D TOUGH mesh used by Consolazio et al. (1998) in numerical simulations was acquired and lightly modified for TOUGH2 simulations presented here. Three new features are included, (1) an “*effective*” conductive boundary approach, a modeling technique used for a radiation boundary condition between a specimen and a radiant heat source, (2) the proposed *relative permeability function*, and (3) the relationship between the permeability and slip flow constant.

Because water permeability of the cement mortar specimen considered by Consolazio et al. was not available, a logarithmic relationship between the intrinsic gas permeability data and the intrinsic water permeability data of concrete from experimental data of Dhir et al. (1989) is used to approximate the water permeability of a cement mortar whose intrinsic gas permeability is  $8.3424\text{E-}16 \text{ m}^2$

$$K_g = \exp(-9.626 + 0.69 \ln(K_w)) \quad (4.27)$$

However, concern over possible deviation of the approximated value from the actual water permeability due to the type of aggregates used and the Agg/(C+P) were believed to significantly affect the water permeability. Therefore, upper and lower bounds of the ratio  $\alpha$  (i.e., the ratio of the intrinsic water permeability to the intrinsic gas permeability of a concrete) are used for simulations as

$$0.038 \leq \alpha \leq 0.068 \quad (4.28)$$

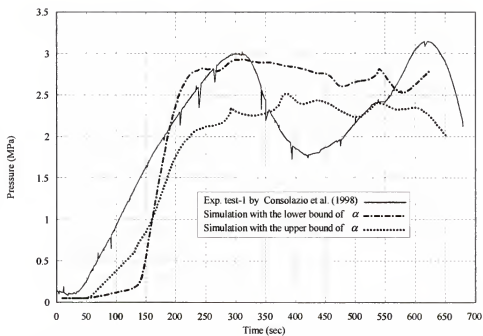
The upper bound of the ratio  $\alpha$  was computed by Eqn. (4.27) whereas the lower bound value was extrapolated for a concrete having a 14.5 % porosity from the data available for concrete having porosity in a range between 7.5% and 13.3% in

Whiting's experiments (1988). The results of simulating the conditions considered by Consolazio et al. (1998) are shown in Figure 4-5.

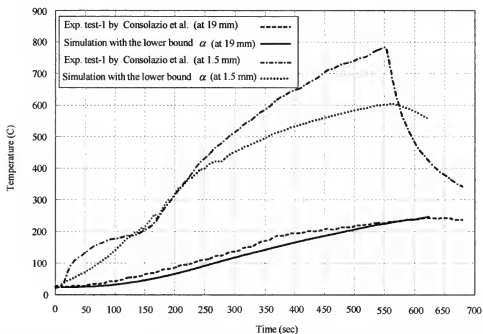
As illustrated in Figure 4-5a, pore pressures occurring at a position approximately 19 mm from the heated surface of the model are compared to experimental data measured at the same location. The pore pressure dip for the experimental case was reported as attributable to voids created by the placement of pore pressure transducers in testing, "*the dip is a product only of the specific instrument setup and not a phenomenon that would normally occur in a non-instrumented specimen*" (Consolazio et al. 1998), and thus is not of great concern in terms of validating the numeric model. More importantly, the initial peaks for the simulated and experimental curves match in magnitude and location (time).

One may note that the peak pore pressures predicted by the numerical simulation with the lower bound ratio very closely match the actual pore pressure measured experimentally. Despite the same volume fraction of voids (porosity), a cement *mortar* specimen can have a denser pore-size distribution than *concrete*. This is believed to result in lowering the water permeability of the cement mortar compared to a concrete having the same porosity. Thus, the model with the lower bound value of  $\alpha$  seems to be better matched with pore pressure data measured by Consolazio et al. (1998).

Temperature data at 19 mm depth as predicted by the simulation (Figure 4-5b) shows an overall match with the experimental curve although the simulated temperature curve at 1.5 mm depth diverges significantly from the experimental data



(a) Pore pressures measured experimentally and predicted using a 2-D simulation model



(b) Temperatures measured experimentally and predicted using a 2-D simulation model

Figure 4-5 Comparison of numerical prediction to experimental measurement

This indicates that conductive and convective heat transfer through the specimen is well predicted yet the temperature changes at locations nearer to the surface exposed to the heat source may have been involved with errors in modeling the radiant boundary condition and in the assumed location of the thermocouples as reported in the literature.

#### 4.7 Finite Difference Simulation

Having validated the modeling proposed techniques, focus will now be turned to studying the effects of reinforcing steel on moisture movement in heated R/C columns. 2-D simulation models are constructed for a longitudinally R/C column made of concrete I (Table 4-1) with a 0.38 x 0.38 m square cross section exposed to a radiant fire as shown in Figure 4-6a. Due to symmetry of the geometry and the thermal loading conditions, partial symmetry models were used, which are shown in Figure 4-6b and 4-6c for each heating condition simulated.

##### 4.7.1 Modeling boundary conditions

One-half and one-quarter of the cross section were discretized by symmetry. Along the symmetric boundaries, zero flux (no flux of mass or heat) boundary conditions were specified whereas the surfaces exposed to the heat source were modeled as a radiant heat flux boundary condition. For the radiant heat flux boundary denoted by  $\Gamma_q$ , heat source is modeled using ASTM E119

$$-\kappa_{bound}^e \frac{\partial T}{\partial n} = T(t) \quad \text{on } \Gamma_q \quad (4.29)$$

where  $\kappa_{bound}^e$  represents the effective conductivity on the boundary between the radiant heat source and the exposed surface. Particularly for the case of one-side

thermal loading condition (Figure 4-6 a), the boundaries on ambient air are modeled as a Dirichlet boundary, i.e. a constant pressure and a constant temperature condition, by using elements that are very permeable and have very large volume relative to the surface elements so as to ensure the constant thermodynamic state in ambient air

$$\begin{aligned} T(x, y, t) &= T_0(x, y) = T_{amb} \text{ on } \Gamma_T \\ P(x, y, t) &= P_0(x, y) = P_{atm} \text{ on } \Gamma_P \end{aligned} \quad (4.30)$$

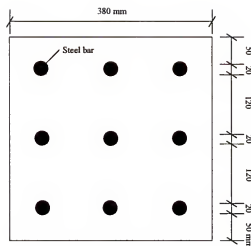
where  $T_{amb}$  represents ambient temperatures at the initial state on the temperature boundary  $\Gamma_T$  and  $P_{atm}$  is the atmospheric pressure that is constant on the pressure boundary  $\Gamma_P$  throughout the time domain.

#### 4.7.2 2-D simulation results

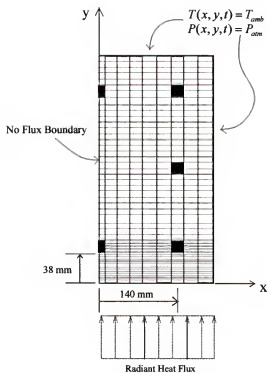
From a 2-D simulation with one-side heating boundary condition, variation in build-up of pore pressure along the heat flux direction is observed along with discontinuity in development of thermal gradients due to presence of the longitudinal bars (Figure 4-7).

A time history of the pore pressure build-up is plotted in Figure 4-7a, which is sampled at a location of  $x = 140$  mm (Figure 4-6b). For a better resolution, it is plotted for only the first 120 mm along the y-coordinate. A quasi-saturated zone is developed in front of the steel bars much earlier than that occurring at the adjacent concrete domain at  $x = 140$  mm (Figure 4-7b). This early moisture clog formation affects the distributions of pore pressure and temperature. Most notably, the peak pore pressure in the front region of the steel bar ( $y = 38$  mm) reaches up to 4.35 MPa after

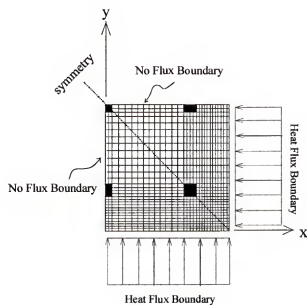




(a) 2-D geometric dimensions

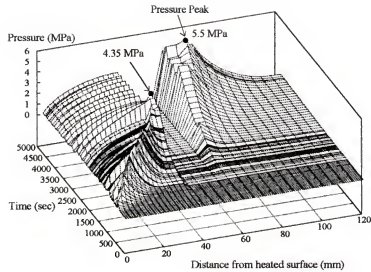


(b) A 2-D discretized mesh with an one-side heating condition

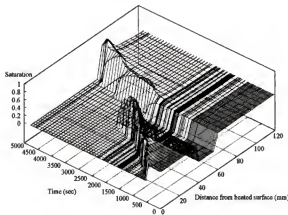


(c) A 2-D discretized mesh with a four-side heating condition

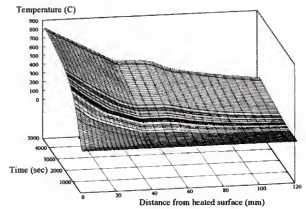
Figure 4-6 2-D simulation models



(a) Pore pressure



(b) Degree of saturation



(c) Temperature

Figure 4-7 Thermodynamic state variables determined by a 2-D simulation

after 30 minutes of heating and the peak of pore pressure at a point

( $x = 100$ ,  $y = 38$  mm) is predicted as less than 3.5 MPa.

A discontinuity in the temperature field occurs at the front region of the steel reinforcing bar (Figure 4-7c). Because of the early formed moisture clog caused by the impermeable steel, heat carried by the moisture flow in the surface concrete is

accumulated whereas heat can transfer quickly through the steel bar, thermal diffusivity of steel is greater than that of concrete. Therefore, a steeper thermal gradient is observed in the concrete region in front of the steel whereas almost no thermal gradient is developed within the steel layer. Consequently, the slope of temperature field (thermal gradients) noticeably changes as a quasi-saturated zone forms and affects the thermally driven moisture flow.

Figure 4-7b also indicates that a quasi-saturation zone is formed behind the steel reinforcement whereas the degree of saturation at the front decreases. The build-up of pore pressure in the front of the steel becomes large enough to force the clogged moisture to permeate through the concrete area around the steel. Also, the degree of saturation in front of the steel decreases as evaporation of the water content in the clogged region begins. The more temperature and pressure fields rise, the more evaporation occurs in the region. Eventually the pressure build-up dissipates when the region is desaturated. Apparent permeability of concrete to gas is thought to be the reason for quick dissipation because the intrinsic permeability to moist air is higher than that to liquid water due to the slip flow phenomenon. Thus, peak of pore pressure build-up is found to be in the moisture-clogged regions rather than the desaturated zones. Therefore, presence of the steel reinforcement impedes moisture movement through the concrete area. This clogging results accumulation of moisture in front of the steel.

#### **4.7.3 Comparison of 2-D simulations modeled by various fire conditions**

In this section, three different fire conditions are simulated. Although it is known that a higher rate of heating rapidly induces a steeper thermal gradient and

larger pore-pressure build-up compared to a slow rate of heating, qualitative computation of pore pressure and its time history were of interest here. For example, the relationship between the intensity of the heating rate and time histories of moisture-clog formation and temperature distribution in the presence of steel reinforcement need to be adequately addressed for a better understanding fire resistance of high-strength concrete.

A 2-D simulation of all four sides of the reinforced column exposed to fire is performed. The data of pore pressure and saturation are plotted in Figure 4-8 along the line of symmetry as indicated in Figure 4-6c. Comparing to a 2-D simulation with one-side heating boundary condition, earlier formation of moisture clogging in the four side heating simulation is observed at  $t=1500$  sec. (25 minutes) and pore pressure at  $x=100$  mm and  $y=38$  mm is predicted as 6.0 MPa. The more heat comes into the system, the more rapid formation of moisture clog is induced and the greater pore pressure builds up. Therefore, the influence of moisture movement in pore pressure build-up is more noticeable in the simulation of four side heating condition.

Next, a 2-D simulation for the case of all four sides of the column exposed to a hydrocarbon pool fire (modeled by ASTM E1529) is performed. At a geometric location ( $y'=38$  mm, see Figure 4-9), the pore pressure, saturation, and temperature data are plotted and compared with other simulation results predicted under different fire conditions as shown in Figure 4-9. The case of ASTM E1529 heating shows the most pronounced influence of movement of the saturation front in pore pressure because the hydrocarbon fire has a much steeper temperature rise in the first ten minutes.

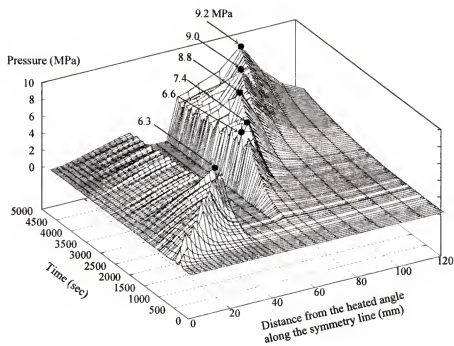
Therefore, the rate of heating and boundary heating condition significantly affects development of thermodynamic states of concrete, the pressure and temperature profiles, particularly during the first twenty minutes of simulation time. The presence of steel reinforcement produces more influence in pressure and temperature fields in concrete when exposed to high rate of heating than when exposed to low rate of heating.

#### **4.7.4 3-D simulation results**

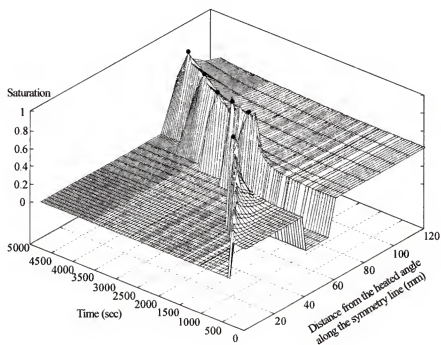
Effects of steel reinforcement on heat and mass transfer in the concrete domain have been found to be severe, particularly in high rate heating. Even a larger build-up of pore pressure and a significant change in temperature distribution (development of steeper temperature gradients) are predicted by simulating reinforced steel in concrete structural elements exposed to fire.

A 2-D simulation model including shear reinforcement would not be appropriate simply because shear reinforcement would completely prevent the moisture flow from reaching a deeper region beyond the impermeable layer of steel (Figure 4-10a and Figure 4-10b). Instead, a 3-D simulation model is constructed that is capable of simulating three-dimensional fluid flow through concrete surrounding reinforcing steel bars including both longitudinal and shear reinforcement.

Due to symmetry of the geometry and the thermal loading condition (modeled using ASTM E1529), only one-eighth of the actual column segment is discretized with no flux boundary conditions at all the symmetric surfaces (Figure 4-10c). A large rise of pore pressure is observed (Figure 4-11a) at a depth of  $z' = 5$  mm along



(a) Pore pressure



(b) Degree of saturation

Figure 4-8 Variation of pore pressures and degrees of saturation

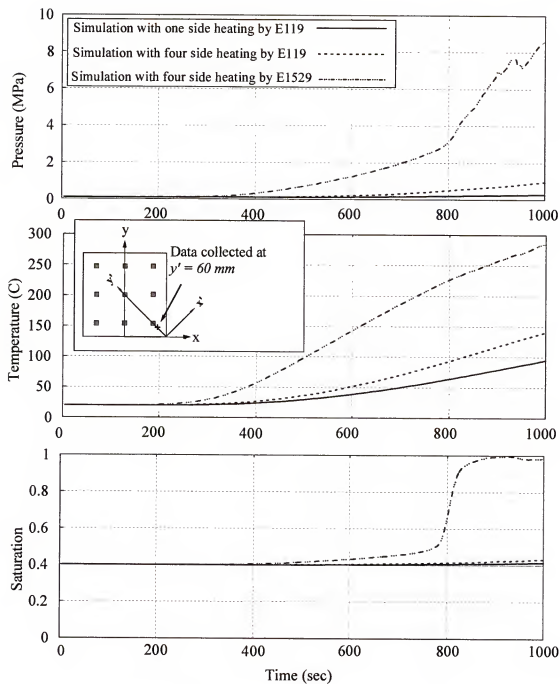
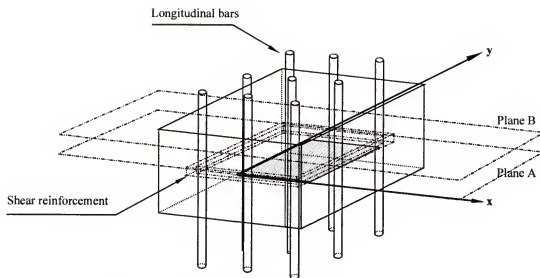
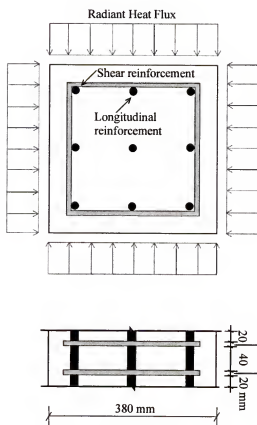


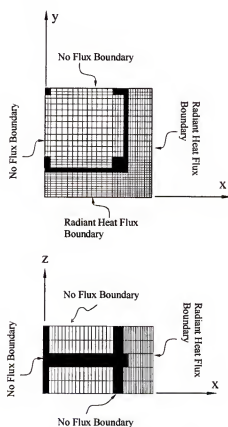
Figure 4-9 Comparison of 2-D simulation results



(a) A schematic sketch of a reinforced concrete column segment



(b) Geometric dimensions



(c) A discretized mesh

Figure 4-10 Geometry of a 3-D simulation mesh and a thermal loading boundary



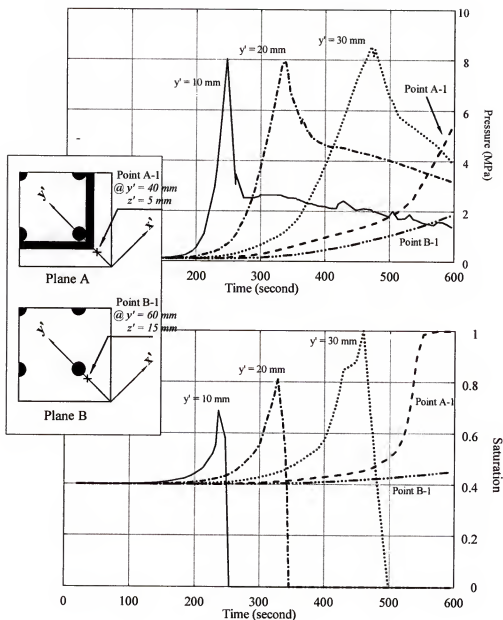


Figure 4-11 Variations of pore pressures and degrees of saturation

the  $y'$ -axis. A quasi-saturated zone (Figure 4-11b) is rapidly developed in concrete regions, occurring at locations adjacent to  $y' = 20$  mm after 5 minutes of heating. This rapid formation of a moisture clog induces the peak pore pressure ( $y' = 30$  mm) that exceeds 8 MPa after 7 minutes of heating. In particular, a larger pressure build-up

(5.5 MPa) was predicted in the 3-D simulation along the boundaries between the concrete regions and the shear steel at Point A-1 in Figure 4-11 whereas pressure less than 1.5 MPa was predicted (  $y' = 60$  mm ,  $z' = 15$  mm ) in the 2-D simulation after 10 minutes. The simulation results indicate that impermeable steel reinforcing bars alter moisture flow in the concrete matrix. Consequently, the temperature distribution changes and very high pore-pressure develops in the concrete.

Two important causes for explosive thermal spalling of concrete, i.e., thermal gradients and pore pressures, are found to be significantly altered by the presence of steel reinforcement in heated high-strength concrete structural members. From the simulation results, very high pressure build-up can be developed in reinforced concrete structures made of very low permeable concrete such as concrete with a 28 day compressive strength of more than 60 MPa with a low W/C ratio.

In the following chapter, the discussion will be expanded to include predictions not only of pore pressure and temperature, but more importantly the stresses produced by these effects. The effects of steel reinforcement in the coupled moisture and heat transfer phenomena will be addressed in Chapter 6.

## CHAPTER 5

### FINITE ELEMENT STRESS ANALYSIS OF A REINFORCED HIGH-STRENGTH CONCRETE COLUMN IN SEVERE FIRES

The objective of this chapter is to develop finite element stress analysis models, which can predict stress states developed in a reinforced concrete structural element exposed to rapid heating. Obtained from finite difference models of simulating coupled heat and mass transport phenomena in heated reinforced concrete elements, transient temperature profiles are used as prescribed boundary conditions for subsequent finite element thermoelastic stress analysis. Thus, a computational methodology is presented to analyze stress states associated with coupled hydro-thermal behavior of concrete exposed to severe fire conditions. Multidimensional finite element models that characterize structural response of reinforced concrete columns exposed to radiant heating conditions are developed. The principle of superposition and a *volume-averaging* theory are used to compute thermally induced effective stresses that are potentially associated with thermal spalling of high-strength concrete. Effects of steel reinforcements on coupled heat and moisture transport phenomena are also considered.

#### 5.1 Goals and Scope

In the past, explosive spalling of concrete structures has been investigated by making use of numerical models that analyze mass and heat transfer phenomena in plain concrete exposed to fire. Kodur (1999) reported that thermal spalling of intensively heated concrete would result from pore pressure and thermal stress development in

concrete structural elements. In particular, high strength concrete (HSC) exposed to rapid heating has a greater tendency to explosively spalling than does normal strength concrete (NSC) (Phan and Carino 1998, Sullivan 2001). Previous studies by Kodur (1997) and Kalifa et al. (2000) have theorized that the lower permeability of HSC—compared to that of NSC—is responsible for the higher susceptibility of HSC to violent spalling.

In past published articles (Ymazaki et al. 1995, Moyne et al. 2000), no major efforts in modeling of a coupling between thermo-mechanical stress and pore pressure have been found. Only a limited number of computational analyses that focused on hydro-thermal behavior of concrete at high temperatures have been recently reported (Gawin et al. 1999, Tenchev et al. 2001). Consequently, very few simulation codes, which are capable of simulating the coupled hydro-thermal and structural behavior of concrete structures, have been developed in this research field. The needs for the development of a *new numerical tool* capable of simulating such coupled processes are thus evident (Phan and Carino 2000). The numeric tool developed here will assist researchers in gaining insight into the thermo-mechanical behavior of concrete structures during a transient process of coupled heat and mass transfer. Implementation of the new analytical model is accomplished by adding new thermal modeling features to the existing PLASFEM nonlinear finite element code developed by Dr. Michael McVay of the University of Florida, Department of Civil and Coastal Engineering, Geotechnical Engineering group.

This chapter also focuses on qualitatively understanding the development of stress states in concrete exposed to coupled heating and moisture migration processes.

To conduct the study, a three-dimensional combined finite difference (TOUGH2) and finite element model (PLASFEM) has been developed that is capable of analyzing the transient heat conduction in partially saturated concrete and predicting states of effective stress. An existing commercial program, ADINA (ADINA 2002) is employed to model a 2-D axisymmetric thermoelastic problem and to validate the present 3-D finite element model. The coupling effects of moisture flow on the development of the thermodynamic temperature field are studied in consideration of the following important characteristics of heat and mass transfer through concrete

1. Strong coupling of pore pressure, temperature, and moisture content.
2. Multi-phase mass transfer (liquid and gaseous phases).
3. Nonlinear characteristics of key material parameters such as permeability, conductivity, density, and porosity and their dependency on pressure, and degree of saturation.

## 5.2 Governing Differential Equations for the Mass and Energy Balance

The balance laws used in this study treat concrete as a multiphase continuum analogous to that of a simple continuum. Global balances apply to the multiphase continuum as a whole via an averaging process, i.e., *volume averaging*, which is used for a framework to construct mathematical formulations of governing field equations at the macroscopic level. the first, the mass balance law is reviewed for a multi- phase mixture, which is a collection of overlapping continua called phase,

$$\frac{\partial \rho}{\partial t} + \text{div } \rho \mathbf{v} = 0 \quad (5.1)$$

where each phase  $\pi$  occupies a fraction of the overall mixture volume defined by a volume fraction  $\eta^\pi(x, t)$  and has the volume-averaged mass density  $\rho$  with the mean velocity  $v(x, t)$  defined in Chapter 4. The first term on the left side accounts for the accumulation of phases and is known as the *mass concentration* in the fluid phases (water and water vapor) and the second term models the advection and diffusion of the fluid phases with the mean macroscopic flow velocity.

For the energy balance, we have a governing equation describing the macroscopic energy balance

$$\rho \frac{\partial E}{\partial t} + \nabla \cdot \mathbf{q} - \sigma : \nabla \mathbf{v} - \rho h = 0 \quad (5.2)$$

where the terms have the following physical interpretations  $\rho \frac{\partial E}{\partial t}$  is the rate of change of internal energy,  $\nabla \cdot \mathbf{q}$  is the rate of heat flow,  $-\sigma : \nabla \mathbf{v}$  represents heating caused by compression and dissipative momentum transfer (e.g., elastic and plastic deformation), and  $-\rho h$  is the rate of heating by external supplies.

### 5.3 The Coupled Heat Conduction Equation

Based on the Helmholtz free energy and the Fourier law of heat conduction, a coupled heat conduction equation that describes the energy balance of Eqn. (5.2) in a concrete member can be expressed at the macroscopic level (Hsu 1986)

$$\rho C_p \frac{\partial T}{\partial t} = (k T_{,i})_{,i} + Q + T \frac{\partial \sigma_{ij}}{\partial T} \dot{\epsilon}_{ij} \quad (5.3)$$

where  $C_p$  represents a volume-averaged specific heat at a constant pressure, the absolute temperature of a *representative element volume* (REV) (Lewis and Schrefler 2000) of concrete is denoted by  $T$ ,  $k$  represents a volume-averaged thermal conductivity that is assumed to be a function of temperature and degree of liquid water saturation,  $Q$  represents heat source term in the REV,  $T \frac{\partial \sigma_{ij}}{\partial T} \dot{\epsilon}_{ij}$  represents a volume-averaged thermo-elastic coupling factor. In this conceptual formulation of thermal-energy associated with mechanical strain energy, only a strictly reversible energy balance is considered in this study.

In regard specifically to the mass and energy balance framework equations described above, the following assumptions are made 1) the concrete material can be characterized as a continuum via a volume averaging process such that all physical quantities (e.g., mechanical deformation, temperature) must follow continuous functions, 2) changes in material temperature due to mechanical strain are negligibly small and can therefore be neglected (i.e., within the scope of conducting the heat and moisture flow analyses in this study, the quantity  $T \frac{\partial \sigma_{ij}}{\partial T} \dot{\epsilon}_{ij}$  in Eqn (5.3) is neglected).

#### 5.4 The Principle of Stress Superposition

To analyze the combined effects of moisture movement and temperature gradient development in the computation of thermally induced stresses, the principle of superposition is used in solving the linear momentum balance equation with mixed boundary conditions. Discussion regarding stress states in heated concrete shall be made at a macroscopic level where continuous distributions of the phases are

assumed. This means that, at every particle, all phases are present at the same time in proportion to their volume fractions.

To integrate microscopic level stresses into the macroscopic level of interest of continuum mechanics, we apply the *volume-averaging* process to compute stress components of a total stress state at a thermodynamic equilibrium state. In the following, total stress at the macroscopic level is defined as the sum of averaged quantities of stress components through summation of all the momentum balance equations written for the solid and fluid phases

$$\nabla \cdot (\eta^s \sigma^s + \eta^f \sigma^f) + (\eta^s \rho^s + \eta^f \rho^f) g = 0 \quad (5.4)$$

where continuity of the stress field across the solid-fluid interface is assumed to be valid so that the linear momentum balance equation for the multi-phase concrete medium is obtained.

Therefore, averaging the microscopic stress quantity over the REV, we have

$$\bar{\sigma} = \frac{1}{dV_{REV}} \int_{dV_{REV}} \sigma_m dV_m \quad (5.5)$$

where  $\bar{\sigma}$  is the total stress tensor macroscopically averaged over the REV  $dV_{REV}$ .

The total stress tensor consists of two distinct components

$$\bar{\sigma} = \frac{1}{dV_{REV}} \left[ \int_{dV^s} \sigma_m dV_m + \int_{dV^f} \sigma_m dV_m \right] \quad (5.6)$$

where  $dV^s$  and  $dV^f$  represents the volumes of the solid phase and the fluid phase, respectively. We can further decompose the stress tensor of the fluid phases into two parts such that



$$\underline{\sigma} = \frac{1}{dV_{REV}} \left[ \int_{dV^S} \underline{\sigma} dV_m + \int_{dV^f} \left( \frac{1}{dV^f} \int_{dV^w} \underline{\sigma} dV_m + \frac{1}{dV^f} \int_{dV^g} \underline{\sigma} dV_m \right) dV_m \right] \quad (5.7)$$

where  $dV^w$  and  $dV^g$  are the volume of liquid water and the volume of the mixture of air and water vapor, respectively.

$$\underline{\sigma} = \frac{dV^S}{dV_{REV}} \underline{\sigma}_S + \frac{dV^f}{dV_{REV}} \left( \frac{dV^w}{dV^f} \underline{\sigma}_w + \frac{dV^g}{dV^f} \underline{\sigma}_g \right) \quad (5.8)$$

Using the *volume fraction* term  $\eta_\pi$  ( $\pi = s, w, g$  solid, liquid water, and gas respectively), Eqn.(5.8) can be expressed in terms of the porosity  $n$  and the degree of saturation  $S_\pi$  to a particular fluid phase  $\pi$  in a partially saturated concrete

$$\underline{\sigma} = (1-n) \cdot \underline{\sigma}_S + n \cdot (S_w \underline{\sigma}_w + S_g \underline{\sigma}_g) \quad (5.9)$$

where  $\underline{\sigma}_\pi$  represents the stress tensor in phase  $\pi$  of concrete. If shear stresses in fluid phases (liquid water and the air—water vapor mixture) are assumed to be negligible, then the stress tensors of the fluid phases may be written in terms of hydrodynamic pressure  $p_\pi$ . We can write

$$\underline{\sigma} = (1-n) \cdot \underline{\sigma}_S - n \cdot (S_w p_w \mathbf{I} + S_g p_g \mathbf{I}) \quad (5.10)$$

Assuming that local thermodynamic equilibrium exists, then  $p_w = p_g = p$  where  $p$  is the internal pore pressure (the same quantity obtained from TOUGH2 analyses), and the total stress tensor is may be expressed as

$$\underline{\sigma} = (1-n) \cdot \underline{\sigma}_S - n \cdot p \mathbf{I} \quad (5.11)$$

Thus, the effective stress is written

$$(1-n) \cdot \underline{\sigma}_s = \underline{\sigma} + n \cdot p \underline{I} = \underline{\sigma} + p_{avg} \underline{I} \quad (5.12)$$

where  $p_{avg} \underline{I}$  represents the volume-averaged hydrostatic stress tensor at a thermodynamic equilibrium state. The volume-averaged total stress tensor  $\underline{\sigma}$  then consists of mechanically induced stress and dilatation-induced thermal stress

$$\underline{\sigma}_s^* = \underline{\sigma} + n P \underline{I} \quad (5.13)$$

where  $\underline{\sigma}_s^*$  is the effective stress acting on the solid skeleton. The quantity  $\underline{\sigma}_s^*$  represents the stress carried solely by the solid skeleton and therefore may be used in assessing the potential for fracture related material failure. However, in evaluating effective stress, alternative porosity parameters may be used to more accurately reflect the failure surface involved. Bažant and Kaplan (1996) note that *boundary porosity*,  $n_p$ , may be more appropriate in computing effective stresses developed in the concrete solid skeleton. They define  $n_p$  as the porosity of the “macroscopically planar but microscopically tortuous weakest section through the materials” and note that  $n_p \cong 0.9$  is a reasonably representative value for concrete. Thus, in the present study, the linear momentum balance of the concrete system is expressed in term of the effective stress

$$\nabla \cdot \underline{\sigma}_s^* = 0 \quad (5.14)$$

Using a generalized Hooke’s law (Malvern 1969), the total stress tensor can be expressed

$$\begin{aligned}
\sigma_{ij} &= C_{ijkl} \{ \varepsilon_{kl} - \chi_{kl}(\Delta T) \} \\
&= (K - \frac{2}{3}G) \varepsilon_{kk} \delta_{ij} + 2G \varepsilon'_{ij} - 3K\alpha(\Delta T) \delta_{ij}
\end{aligned} \tag{5.15}$$

where  $\chi_{kl}$  represents a volume-expansion coefficient tensor,  $K$  is the bulk modulus,  $G$  is the shear modulus,  $\varepsilon_{kk}$  is the volumetric strain,  $\delta$  is the Kronecker delta,  $\varepsilon'_{ij}$  are the deviatoric strain components,  $\alpha$  represents a linear expansion coefficient, and  $\Delta T$  represents the change of temperature in the concrete. Substituting the linear elastic stress-strain relationship in to the linear momentum balance equation, we have

$$\text{div} \left[ \left( K - \frac{2}{3}G \right) \varepsilon_{kk} \delta_{ij} + 2G \varepsilon'_{ij} - 3K\alpha(\Delta T) \delta_{ij} + p_{avg} \delta_{ij} \right] = 0 \tag{5.16}$$

## 5.5 2-D Axisymmetric Finite Element Stress Analysis

Computation of effective stresses using the principle of superposition described above requires that pore pressures be combined with stresses are induced by thermal dilation and boundary condition restraint. Here, finite element based thermo-mechanical analysis—using the ADINA finite element code (ADINA 2002)—is used for the purpose of computing these thermally induced stresses inside a circular concrete column exposed to a fire modeled using ASTM E119 (ASTM 1995).

### 5.5.1 Initial and boundary conditions

The initial conditions needed to solve for the coupled thermo-mechanical equation of a concrete structural system are specified as the absolute temperature field  $T$  at an initial time  $t = 0$  in the domain  $\Omega$  and of boundary condition on the surface  $\Gamma$ . The initial temperature field is then specified as

$$T(x, y, z, S_w, t) \Big|_{t=0} = T_0(x, y, z) \quad \text{in } \Omega \quad (5.17)$$

where the initial temperature field  $T_0(x, y, z)$  is a function of the spatial coordinates only. The initial temperature distribution  $T_0(x, y, z)$  in Eqn. (5.17) is assigned with a constant value for the uniform temperature, e.g., an ambient temperature of 20 °C.

The values of temperature at the boundary  $\Gamma_T$  are specified to vary with time, i.e.,

$$T = T(x, y, z, t) \quad \text{on } \Gamma_T \quad (5.18)$$

The thermo-mechanical stress analyses conducted here are considered to be one-directionally coupled because, as was noted earlier, temperature changes are assumed to induce thermal-dilational deformation but mechanical deformations are assumed to produce no change in system temperature. This assumption permits us to compute the time-varying temperature field separately, and then to apply that temperature field to finite element thermal stress models to evaluate time-varying thermal stresses.

### 5.5.2 Axisymmetric finite element modeling

2-D axisymmetric simulation models are constructed for a 0.3 m diameter circular concrete column made of a high-strength concrete that is exposed to an axially symmetric radiant fire as shown in Figure 5-1. TOUGH2 and the newly proposed fluid-flow constitutive laws discussed in Chapter 4 are used to solve the coupled heat and moisture flow equations and yield a complete time-varying description of the temperature field throughout radial direction of the column. A one-

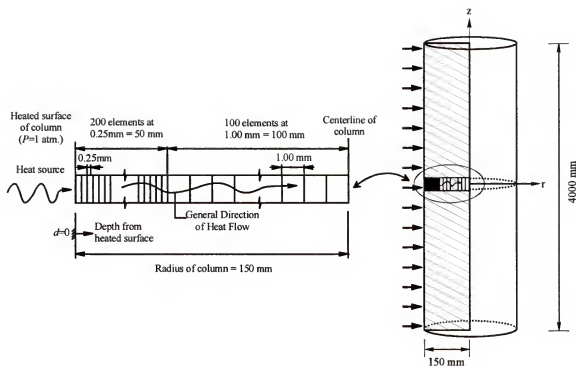
dimensional TOUGH2 model shown in Figure 5-1 represents a typical radial slice of the example circular column.

Computations are carried out using the thermo-mechanical material properties presented in Table 5-1. Material parameters of high-strength concrete under static loading were approximated using the assumptions, 1) the compressive strength of plain concrete is approximately 55.0 Mpa (  $f'_c \approx 8000 \text{ psi}$  ), 2) modulus of elasticity considered is for static loading rather than dynamic rates of loading, 3) for normal-weight concrete with a density of  $2200 \text{ Kg/m}^3$  (  $\approx 135 \text{ lb/ft}^3$  ), the initial modulus of elasticity can be evaluated as  $E = 57000\sqrt{f'_c}$ .

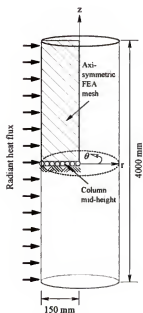
Table 5-1 Thermo-mechanical material properties

Material parameter and description	Concrete	Steel	Units
$E$ (modulus of elasticity)	35000.0	206850.0	MPa
$\rho$ (mass density)	2200.0	7850.0	$\text{Kg/m}^3$
$\nu$ (Poisson's ratio)	0.19	0.29	-
$k$ (heat conductivity)	2.9	46.0	$\text{Watt}/(\text{m} \cdot \text{C}^\circ)$
$C_p$ (heat capacity)	921	419	$\text{Joule}/(\text{kg} \cdot \text{C}^\circ)$
$\alpha$ (linear expansion coeff.)	11.0 E-6	12.0 E-6	$1/\text{C}^\circ$

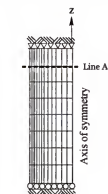
Temperature data from the one-dimensional TOUGH2 models are then mapped onto nodes located along radial lines in the axisymmetric finite element thermal stress models. For each finite element model nodal point, a complete time-history of temperature is extracted from the TOUGH2 simulation results and is then applied to the finite element model as a time-varying prescribed nodal temperature.



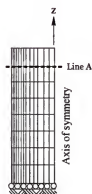
a) One dimensional TOUGH2 model



b) Complete column



c) Fixed boundary condition at top of column



d) Free boundary condition at top of column

Figure 5-1 A one dimensional TOUGH2 model and axisymmetric finite element models of concrete column

Time-varying thermal stress analyses are then performed to compute time-histories of thermal stresses throughout the two-dimensional axisymmetric meshes. Thus, the axisymmetric radiant heat flux boundary condition is modeled as prescribed nodal temperature boundary conditions. The mass- and energy-balance equations have been simultaneously solved using a finite difference model that simulates coupled one-dimensional mass and heat transport phenomena. Thus, using the time history of temperature distributions obtained from the finite difference simulations, temporal nodal temperatures of the finite element model are prescribed.

Due to axial symmetry of the geometry and the thermal loading conditions, partial symmetry finite element models were used. In order to investigate the effects of boundary restraint on dilatation-induced thermal stress in the concrete column, two different mechanical boundary conditions are considered. The finite element model shown in Figure 5-1c shows axial constraint imposed on the both ends of the column and, along the top boundary, displacement in the radial direction is constrained as well. However, no constraint along the radial direction is imposed on the model shown in Figure 5-1d.

### 5.5.3 Simulation results

Figure 5-2 shows maximum principal stress variations sampled along Line A as shown in Figure 5-1b and Figure 5-1c. Dilatation-induced thermal stresses developed in both models increase as heating continues from time=300 seconds to time=600 seconds. More noticeably, the magnitude of the maximum principal stresses significantly increases when coupling effects of moisture and heat transfer are *not* included. Stress data computed with consideration of moisture effects are generally

much less severe than corresponding data computed without consideration of moisture effects.

A significant amount of thermal energy is consumed by latent heat during evaporation of liquid water in concrete pores. Phase-transition and migration of moisture during exposure to fire reduce the temperature increase inside partially saturated concrete. Alternatively, where less severe thermal gradients develop, lesser thermal gradient stresses are induced. Both migration and phase-transition of moisture are found to alter the temperature gradients developed particularly in near-surface zones of the concrete column.

Secondly, comparison of the stress variation between Figure 5-2a and Figure 5-2b reveals that development of the maximum principal stresses can change noticeably in response to the constraints imposed on the boundaries of the structural system. More severe tensile stresses, normal stresses to the axis of symmetry in the near surface zone of the column are developed when the top boundary of the column model is fully constrained.

Shown in Figure 5-3, moisture in concrete pores involved in heat transport is once again indicated by noticeable changes in the minimum principal stresses. It is found that large hoop compressive stresses in near surface regions of the column are developed. The hoop stress component mainly contributes to significant development of the minimum principal stresses. That is, maximum compressive stress develops in the  $\theta$ -direction of the circular column. Furthermore, the values of the minimum principal stress developed in the desaturated concrete model are much larger than those developed in the partially saturated concrete model (see Figure 5-3).

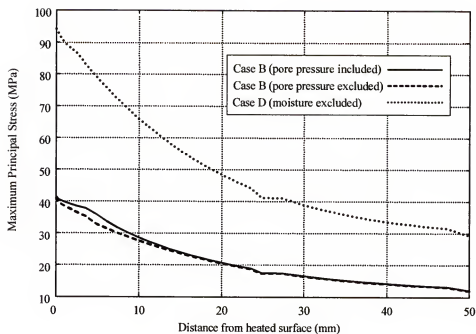


Constraint imposed on the top boundary of the column is found to have minimal effects on the development of compressive stresses in near surface regions of the column. In contrast, this boundary condition has more prominent influence in the development of tensile stresses. Temperature gradients developed in the radial direction in the desaturated model are larger and thus, more compressive thermal stress is induced in  $\theta$ -direction. It is also noted that the contributions of pore pressure to the effective tensile stresses are nearly negligible.

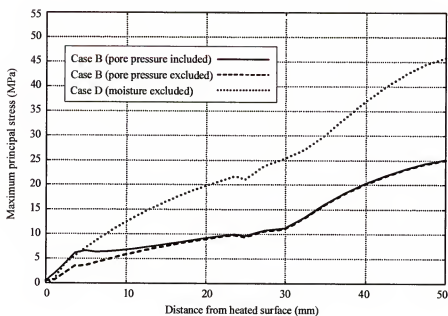
Large tensile radial-stress in the  $r$ -direction of the outer region are developed and found amplified when the top boundary is restrained against vertical displacement. Interestingly, larger compressive hoop-stresses in the  $\theta$ -direction of the inner region where a uniform temperature rise occurs are developed regardless of whether the boundary constraint is imposed on the top boundary of the column model. The outer shell of the column thermally expands much more than the cooler inner core inducing bending in the column.

### **5.6 3-D Finite Displacement/Temperature Mixed Formulations**

As discussed in Chapter 4, the fire resistance of structural concrete elements such as beams and columns can be significantly influenced by thermodynamic states in the system during transient coupled moisture and heat transfer phenomena. Thus, focus was placed primarily on quantifying thermodynamic state variables such as pore-pressure, temperature, and saturation that characterize the hydro-thermal behavior of concrete under a thermal loading condition. In addition, the effects of steel reinforcement of the structural concrete elements on hydro-thermal behavior of

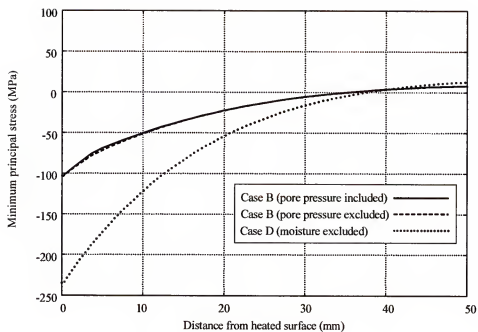


a) Maximum principal stresses (fixed boundary)

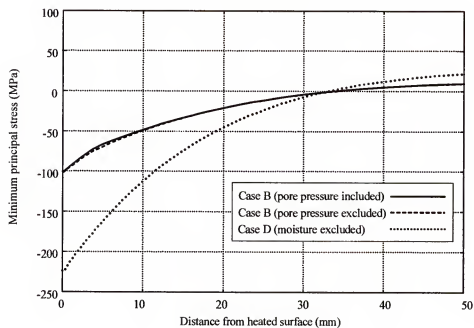


b) Maximum principal stresses (free boundary)

Figure 5-2 Comparison of maximum principal stresses at  $t = 600$  sec.



a) Minimum principal stresses (fixed boundary)



a) Minimum principal stresses (free boundary)

Figure 5-3 Comparison of minimum principal stress variations with respect to initial and boundary conditions

concrete under a thermal loading condition. In addition, the effects of steel reinforcement of the structural concrete elements on hydro-thermal behavior of concrete were investigated and quantitatively identified for the influence of heterogeneity of the system in the development of thermodynamic states.

In subsequent sections, a three-dimensional finite element with temperature degree of freedom will be developed. Transient temperature profiles that were obtained from three-dimensional finite difference model of simulating hydro-thermal behavior of reinforced high-strength concrete column exposed to a hydrocarbon pool fire in Chapter 4 is then mapped into the finite element domain to perform thermal stress analysis.

Recall the volume-averaged linear momentum balance equation, Eqn. (5.16). For simplicity in the following derivation, the gravitational effects term is neglected. To solve the equation, employ a weighted residual method by introducing residual  $R_\Omega$  due to the error in the approximation

$$R_\Omega = \tilde{\sigma}_{ij,j} \quad (5.19)$$

Introducing a weak formulation by using a *weighting function*  $w_i = w_i(\underline{x})$ , we can express the weighted residual as

$$\int_\Omega w_i R_\Omega d\Omega = 0 \quad (5.20)$$

Thus, we have

$$\int_\Omega w_i \tilde{\sigma}_{ij,j} d\Omega = 0 \quad (5.21)$$

Using integration by parts, the weighted residual equation becomes

$$\int_V (w_i \tilde{\sigma}_{ij})_{,j} d\Omega - \int_V w_{i,j} \tilde{\sigma}_{ij} d\Omega = 0 \quad (5.22)$$

By applying the divergence theorem to the above equation, it is rewritten

$$\int_V w_i \tilde{f}_i dA - \int_V w_{i,j} \tilde{\sigma}_{ij} d\Omega = 0 \quad (5.23)$$

or

$$\int_V w_i \tilde{f}_i dA - \int_V w_{i,j} C_{ijkl} \tilde{\epsilon}_{kl} d\Omega - \int_V w_{i,j} (-3K\alpha) \delta_{ij} (\Delta \tilde{T}) d\Omega = 0 \quad (5.24)$$

where  $\tilde{\epsilon}$  and  $\tilde{T}$  are trial functions that satisfy the essential boundary conditions on the boundary of the system, the stress vector is denoted by  $\tilde{t}_i = \tilde{\sigma}_{ij} n_j$ ,  $n_j$  is a surface normal to the boundary surface  $\Gamma$ ,  $K$  represents the bulk modulus, and a thermal expansion coefficient is denoted by  $\alpha$ . This is a weak form of the linear momentum balance equation for a coupled thermo-elastic problem.

Discretization of the above equation is performed by using the approximated solution  $u^h$  as the same weighting function  $w$

$$w \equiv u^h \quad (5.25)$$

that must satisfy the essential boundary conditions. The approximated solution  $u^h$  can then be represented in terms of nodal displacements  $d_i$  and nodal temperatures  $T_i$  as

$$\begin{aligned} u_m^h &= \sum_j N_j d_j \\ u_t^h &= \sum_j \hat{N}_j T_j \end{aligned} \quad (5.26)$$

where  $N$  and  $\hat{N}$  are mapping functions for nodal displacements and temperatures, respectively. Therefore,  $\partial w_i / \partial x_j$  in Eqn. (5.23) can be expressed as

$$w_{i,j} = \frac{\partial x_j}{\partial x_i} w_i = \frac{\partial x_j}{\partial x_i} u_m = \frac{\partial x_j}{\partial} [N] \{d\} = [B] \{d\} \quad (5.27)$$

and

$$w_{i,j} = \frac{\partial x_j}{\partial x_i} w_i = \frac{\partial x_j}{\partial x_i} u'_m = \frac{\partial x_j}{\partial} [\hat{N}] \{T\} = [\hat{B}] \{T\} \quad (5.28)$$

where  $\{d\}$  and  $\{T\}$  denote nodal displacements and temperatures in a vector form.

Therefore, Eqn. (5.23) can be formulated in matrix forms

$$\{d\}_T^T [B]^T [C] [B] d\Omega \{d\} + \{d\}_T^T [B]^T [\hat{N}] \{T\} d\Omega \{T\} = \{d\}_T^T [N]^T \{f\} d\Omega \quad (5.29)$$

where  $[B]$  is the strain-displacement matrix,  $[C]$  is a elasticity-coefficient matrix,

$[\hat{N}]$  is the mapping function matrix, and the thermo-mechanical coupling matrix  $\{B\}$

is defined as

$$\{B\} = -3K\alpha \cdot \{b\} = -3K\alpha \cdot \{1 \ 1 \ 1 \ 0 \ 0 \ 0\}_T^T \quad (5.30)$$

Defining the surface area and the volume of the REV,

$$d\Gamma = d\Gamma_x + d\Gamma_y + d\Gamma_z = dydz + dx dz + dx dy d\Omega \quad (5.31)$$

we perform numerical integration using *Gauss quadrature* over the element volume in the natural coordinate system, i.e., using local axes  $r$ ,  $s$ , and  $t$ , which results in

$$[K_u]\{d\} + [M_T]\{T_a\} = \{F_{ext}\} \quad (5.32)$$

where  $[K_u]$  is the mechanical stiffness matrix,  $\{d\}$  denotes the global mechanical displacement vector,  $[M_T]$  represents the thermo-mechanical coupling matrix,  $\{T_a\}$  denotes the global nodal temperature vector, and  $\{F_{external}\}$  represents the surface force vector. More explicitly, numerical integration is used to evaluate the multi-dimensional integrals in Eqn. (5.32) as follows

$$\begin{aligned} [K_u] &= \sum_{e=1}^{NT} \int_{\Omega_e} [B]^T [C] [B] d\Omega \\ &= \sum_{e=1}^{NT} \int_{-1}^{+1} \int_{-1}^{+1} \int_{-1}^{+1} \det J \cdot [B]^T [C] [B] dr ds dt \\ &= \sum_{e=1}^{NT} \left[ \sum_{\Omega_e}^{i=1,int} \sum_{\Omega_e}^{j=1,int} \sum_{\Omega_e}^{k=1,int} \left( B^T(r_i, s_j, t_k) \cdot C \cdot B(r_i, s_j, t_k) \cdot \det J \cdot W_i \cdot W_j \cdot W_k \right) \right] \end{aligned} \quad (5.33)$$

$$\begin{aligned} [M_T] &= \sum_{e=1}^{NT} \int_{\Omega_e} [B]^T \{\beta\} [\hat{N}] d\Omega_e \\ &= \sum_{e=1}^{NT} \int_{-1}^{+1} \int_{-1}^{+1} \int_{-1}^{+1} \det J \cdot [B]^T \{\beta\} [\hat{N}] dr ds dt \\ &= \sum_{e=1}^{NT} \left[ \sum_{\Omega_e}^{i=1,int} \sum_{\Omega_e}^{j=1,int} \sum_{\Omega_e}^{k=1,int} \left( B^T(r_i, s_j, t_k) \cdot \beta \cdot \hat{N}(r_i, s_j, t_k) \det J \cdot W_i \cdot W_j \cdot W_k \right) \right] \end{aligned} \quad (5.34)$$

where  $NT$  represents the total number of elements, “ $\det J$ ” is the determinant of the Jacobian matrix transforming global to natural coordinates (Bathe 1996), the number of integration sampling points in each element is denoted by “int”, and the  $W$ ’s represent the *weights* corresponding to the *Gauss Quadrature* sampling points. The surface force vector  $\{F_{external}\}$  consists of the following three parts

$$\begin{aligned}
\{F_x\} &= \sum_{e=1}^{NT} \int_{\Gamma_x} [N]^T \{t\} d\Gamma_x \\
&= \sum_{e=1}^{NT} \int_{-1}^{+1} \int_{-1}^{+1} \det J_x [N]^T \{t\} ds dt \\
&= \sum_{e=1}^{NT} \left( \sum_{\Gamma_x}^{j=1, \text{int}} \sum_{\Gamma_x}^{k=1, \text{int}} \left[ N^T(r, s_j, t_k) \cdot \underline{t} \cdot \det J_x \cdot W_j \cdot W_k \right] \right) \bigg|_{\text{at } r=\pm 1}
\end{aligned} \tag{5.35}$$

$$\begin{aligned}
\{F_y\} &= \sum_{e=1}^{NT} \int_{\Gamma_y} [N]^T \{t\} d\Gamma_y \\
&= \sum_{e=1}^{NT} \int_{-1}^{+1} \int_{-1}^{+1} \det J_y [N]^T \{t\} dr dt \\
&= \sum_{e=1}^{NT} \left( \sum_{\Gamma_y}^{i=1, \text{int}} \sum_{\Gamma_y}^{k=1, \text{int}} \left[ N^T(r_i, s, t_k) \cdot \underline{t} \cdot \det J_y \cdot W_i \cdot W_k \right] \right) \bigg|_{\text{at } s=\pm 1}
\end{aligned} \tag{5.36}$$

and

$$\begin{aligned}
\{F_z\} &= \sum_{e=1}^{NT} \int_{\Gamma_z} [N]^T \{t\} d\Gamma_z \\
&= \sum_{e=1}^{NT} \int_{-1}^{+1} \int_{-1}^{+1} \det J_z [N]^T \{t\} dr ds \\
&= \sum_{e=1}^{NT} \left( \sum_{\Gamma_z}^{i=1, \text{int}} \sum_{\Gamma_z}^{j=1, \text{int}} \left[ N^T(r_i, s_j, t) \cdot \underline{t} \cdot \det J_z \cdot W_i \cdot W_j \right] \right) \bigg|_{\text{at } t=\pm 1}
\end{aligned} \tag{5.37}$$

where  $NT$  represents the total number of elements,  $\det J_\gamma$  is the determinant of the 2-D Jacobian matrix transforming global to natural coordinates on element boundaries  $\Gamma_\gamma$  ( $\gamma = x, y, z$ ) (Bathe 1996).

### 5.7 Discretization of the Transient Heat Conduction Equation

Having established the Galerkin form of the weighted residual method when applied to the linear momentum balance equation, we now employ the same method of weighted residuals to form a weak formulation of the volume-averaged transient



heat conduction equation given in Eqn. (5.3). However, in order to solve the partial differential equation of heat conduction, we need the specification of the initial condition at time  $t = t_0$  in initial domain  $\Omega$  and the specification of the boundary condition on the surface  $\Gamma$  for the proposed problem. The initial temperature field considered in this study is specified as

$$T(x, y, z, 0) = T_0(x, y, z) = 0 \quad \text{in } \Omega \quad (5.38)$$

Also, the values of temperature at the boundary  $\Gamma_T$  are specified, which may be constant or may be allowed to vary with time

$$T = T(x, y, t) \quad \text{in } \Gamma_T \quad (5.39)$$

and which are known as a Dirichlet or essential boundary condition. In the other condition, the values of the heat flow in the direction  $n$  normal to the boundary  $\Gamma_q$  are prescribed as  $q_B(x, y, z, t)$

$$q_B = -k \delta_{ij} \frac{\partial T}{\partial n} \quad \text{on } \Gamma_q \quad (5.40)$$

which is called a Neumann or natural boundary condition.

The problem of heat transfer in a concrete structure exposed to fire—where the temperature field at various points in the domain varies with time—is considered to be a *transient* problem. For such problems a temporal discretization for the time derivative of the transient heat conduction is required in addition to the spatial discretization. In the following section, temporal discretization methods are presented for the finite element analysis of transient heat conduction problems.

The residual for the energy balance equation is defined as

$$R_{\Omega} = (k \tilde{T}_{,i})_{,i} + Q + T \frac{\partial \tilde{\sigma}_{ij}}{\partial T} \dot{\varepsilon}_{ij} - \rho C_p \frac{\partial \tilde{T}}{\partial t} \quad (5.41)$$

Prior to a further development of temporal discretization, it is once again noted that the concrete structure considered in this study can be reasonably analyzed without

having to consider the coupling factor  $T \frac{\partial \tilde{\sigma}_{ij}}{\partial T} \dot{\varepsilon}_{ij}$  in the residual for the energy

balance equation. Thus, we have

$$R_{\Omega} = (k \tilde{T}_{,i})_{,i} + Q - \rho C_p \frac{\partial \tilde{T}}{\partial t} \quad (5.42)$$

The subsequent steps of the derivation to obtain the Galerkin form of weighted residual expression remain same as outlined in the previous section. The only exception in the weak form of the transient heat conduction is the temporal derivative term. As defined in Eqn. (5.26), a set of linear independent functions  $[\hat{N}]$  is used as finite element basis functions in the strategy of dividing the solution domain into finite elements and using the element shape functions to define the solution within the element that is based on the nodal values of temperature. In this case, however, the shape functions are also applied to the temporal derivative, i.e.,

$$\frac{\partial \tilde{T}^e}{\partial t}(x, y, z) = \sum_{i=1, NP} \frac{\partial \tilde{T}_i^e}{\partial t} \hat{N}_i^e(x, y, z) \quad (5.43)$$

where  $NP$  represents the number of nodes in each element and  $\tilde{T}^e$  represents temperature residual in each element occupying an element domain  $\Omega_e$ . This results in the following Galerkin finite element form of the discretized equations

$$\int_{\Omega} [\hat{B}]^T [k] [\hat{B}] d\Omega \{T_a\} + \int_{\Omega} [\hat{N}]^T \rho C_p [\hat{N}] d\Omega \{\dot{T}_a\} = \int_{\Gamma_q} [\hat{N}]^T \{q_B\} d\Gamma \quad (5.44)$$

where  $[k]$  represent the thermal conductivity coefficient matrix,  $[\hat{B}]$ , the gradients of the basis functions as defined in Eqn. (5.28), and the heat flux on the surface boundary  $\Gamma$  is defined using the surface normal  $n$  as

$$q_B = -k \delta_{ij} \frac{\partial T}{\partial n} \quad \text{on } \Gamma_q \quad (5.45)$$

Equation (5.44) represents the spatially discretized finite element form of the transient heat conduction equation. Thus, in a more compact form, we rewrite Eqn. (5.44)

$$[C_H] \{\dot{T}_a\} + [K_T] \{T_a\} = \{H_{ext}\} \quad (5.46)$$

where  $[C_H]$  represents the global heat capacity matrix,  $[K_T]$  is the global heat conductivity matrix, and  $\{H_{ext}\}$  represents the global thermal-loading vector after the multi-dimensional integrals are numerically evaluated as

$$\begin{aligned} [C_H] &= \sum_{e=1}^{NT} \int_{\Omega_e} [\hat{N}]^T \rho C_p [\hat{N}] d\Omega \\ &= \sum_{e=1}^{NT} \int_{-1}^{+1} \int_{-1}^{+1} \int_{-1}^{+1} \det J \cdot [\hat{N}]^T \rho C_p [\hat{N}] dr ds dt \\ &= \sum_{e=1}^{NT} \left[ \sum_{\Omega_r}^{i=1, \text{int}} \sum_{\Omega_s}^{j=1, \text{int}} \sum_{\Omega_t}^{k=1, \text{int}} \left( \hat{N}^T(r_i, s_j, t_k) \cdot \rho C_p \cdot \hat{N}(r_i, s_j, t_k) \cdot \det J \cdot W_i \cdot W_j \cdot W_k \right) \right] \end{aligned} \quad (5.47)$$

and

$$\begin{aligned}
 [K_T] &= \sum_{e=1}^{NT} \int_{\Omega_e} [\hat{B}]^T [k] [\hat{B}] d\Omega \\
 &= \sum_{e=1}^{NT} \int_{-1}^1 \int_{-1}^1 \int_{-1}^1 \det J \cdot [\hat{B}]^T [k] [\hat{B}] dr ds dt \\
 &= \sum_{e=1}^{NT} \left[ \sum_{\Omega_e}^{i=1, \text{int}} \sum_{\Omega_e}^{j=1, \text{int}} \sum_{\Omega_e}^{k=1, \text{int}} \left( \hat{B}^T(r_i, s_j, t_k) \cdot k \cdot \hat{B}(r_i, s_j, t_k) \cdot \det J \cdot W_i \cdot W_j \cdot W_k \right) \right]
 \end{aligned} \tag{5.48}$$

The global thermal-load matrix  $\{H_{ext}\}$  consists of the following three parts

$$\begin{aligned}
 \{H_x\} &= \sum_{e=1}^{NT} \int_{\Gamma_x} [\hat{N}]^T \{q_B\} d\Gamma_x \\
 &= \sum_{e=1}^{NT} \int_{-1}^1 \int_{-1}^1 [\hat{N}]^T \{q_B\} ds dt \\
 &= \sum_{e=1}^{NT} \left( \sum_{\Gamma_x}^{j=1, \text{int}} \sum_{\Gamma_x}^{k=1, \text{int}} \left[ \hat{N}^T(r, s_j, t_k) \cdot \underline{q} \cdot \det J_x \cdot W_j \cdot W_k \right] \right) \Bigg|_{at \ r=\pm 1}
 \end{aligned} \tag{5.49}$$

$$\begin{aligned}
 \{H_y\} &= \sum_{e=1}^{NT} \int_{\Gamma_y} [\hat{N}]^T \{q_B\} d\Gamma_y \\
 &= \sum_{e=1}^{NT} \int_{-1}^1 \int_{-1}^1 [\hat{N}]^T \{q_B\} dz dx \\
 &= \sum_{e=1}^{NT} \left( \sum_{\Gamma_y}^{i=1, \text{int}} \sum_{\Gamma_y}^{k=1, \text{int}} \left[ \hat{N}^T(r_i, s, t_k) \cdot \underline{q} \cdot \det J_y \cdot W_i \cdot W_k \right] \right) \Bigg|_{at \ s=\pm 1}
 \end{aligned} \tag{5.50}$$

and

$$\begin{aligned}
 \{H_z\} &= \sum_{e=1}^{NT} \int_{\Gamma_z} [\hat{N}]^T \{q_B\} d\Gamma_z = \iint [\hat{N}]^T \{q_B\} dy dx \\
 &= \sum_{e=1}^{NT} \int_{-1}^1 \int_{-1}^1 [\hat{N}]^T \{q_B\} dy dx \\
 &= \sum_{e=1}^{NT} \left( \sum_{\Gamma_z}^{i=1, \text{int}} \sum_{\Gamma_z}^{j=1, \text{int}} \left[ \hat{N}^T(r_i, s_j, t) \cdot \underline{q} \cdot \det J_z \cdot W_i \cdot W_j \right] \right) \Bigg|_{at \ t=\pm 1}
 \end{aligned} \tag{5.51}$$

The mapping functions  $[\hat{N}]$  used in this study for the nodal temperature degrees of freedom are first order polynomial functions. Two-point Gauss quadrature is then used to integrate the element heat capacity matrix  $[C_H]$  and the element heat conductivity matrix  $[K_T]$ .

### 5.8 27/8 Finite Element

As was mentioned earlier, lower-order temperature interpolations, i.e., first order polynomial functions, have been used as the finite basis functions for nodal temperature degrees of freedom, but higher-order displacement interpolations, i.e., second order polynomial functions, have been used for nodal displacement degrees of freedom. Discussion of appropriate temperature and displacement interpolations that should be used in order to develop an effective element follows.

Assume, for instance, that we use 27 nodes to interpolate the displacements in a three-dimensional element and we assume linear variations of the temperature field by using only 8-node temperature interpolation within the same element. Such an element is referred to as a “27/8 element”. In this formulation, the element temperature is defined by nodal temperature variables that pertain to adjacent elements in the assemblage. Thus, continuity of temperature between elements is always contained in the solution. Then, the temperature prediction could be of higher order and could therefore hypothetically be more accurate.

However, studies have shown (e.g., Bathe 1996) that when a mixed finite discretization such as the u/p-c formulation is used, then a field variable (e.g., pore pressure, temperature) coupled with mechanical displacement should not be interpolated at too high a degree because *locking* could be introduced into the finite

element. Thus, higher-order interpolation for the field variable associated with *coupling* of the mechanical displacement field would have a negative effect on finite element prediction of the mechanical displacement field.

Secondly, the thermo-mechanical coupling matrix  $[M]$  that is numerically integrated for the product of temperature and mechanical displacement interpolation functions would be overly stiffened when Gauss points of a higher-order rule are used to increase the accuracy of a finite element analysis. The number of Gauss points has a lower limit because element volume has to be integrated exactly in the limit of mesh refinement. Thus, when exact integration is used, then small change in the temperature field combined with a higher-order integrated coupling matrix can numerically induce large internal force. As a result, despite the use of an *exact integration scheme* to form the thermo-mechanical coupling matrix  $[M]$ , the finite element solution of the coupled thermo-mechanical stress field may not be reliable. This can occur if over-estimation of the mechanical displacement field results in a large internal force computation (Cook et al. 1989).

Therefore, we want to use the highest degree of temperature interpolation that neither introduces locking into the element nor causes poor quality of the temperature prediction. The 27/8 element shown as Figure 5-4 is most suitable for this purpose because (1) its mixed finite element discretization yields a reliable solution, i.e., it is stable and convergent (Bathe 1996) and (2) the rate of convergence of the temperature field (and thus thermally induced stresses) as the mesh is refined is of order  $O(h^2)$  (Huang and Usmani 1994).

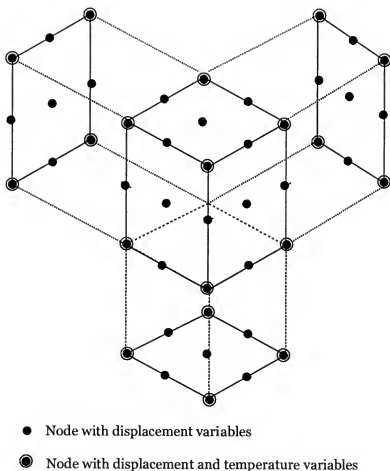


Figure 5-4 A schematic sketch of effective 27/8 element

### 5.9 Solution Approach

In this section, the spatially discretized finite element formulation of the transient heat conduction equation—a first order system of ordinary differential equations with respect to time—will be also discretized in the time domain. The finite difference discretization scheme in which the time domain is divided into small time increments is used to solve the equation step by step in the given space domain. The objective is to develop an algorithm where both the space and time domains are discretized in a piecewise manner. Thus, the unknown values  $d_{n+1}$  and  $T_{n+1}$  in Eqns.

(5.32) and (5.44) at time  $t_{n+1}$  will be determined where the values  $T_n$  are known at time  $t_n$  and so is  $H_{ext}$  in the time interval  $\Delta t$ .

First, we combine Eqn. (5.32) with Eqn. (5.44) in matrix form

$$\begin{bmatrix} \overbrace{\begin{bmatrix} 0 \\ 81 \times 81 \end{bmatrix}}^{89 \times 89} & \overbrace{\begin{bmatrix} 0 \\ 8 \times 8 \end{bmatrix}}^{89 \times 1} \\ \overbrace{\begin{bmatrix} 0 \\ 8 \times 81 \end{bmatrix}}^{89 \times 81} & \overbrace{\begin{bmatrix} C_H \\ 8 \times 8 \end{bmatrix}}^{89 \times 1} \end{bmatrix} \begin{bmatrix} \{ \dot{d} \} \\ \{ \dot{T}_a \} \end{bmatrix} + \begin{bmatrix} \overbrace{\begin{bmatrix} K_u \\ 81 \times 81 \end{bmatrix}}^{89 \times 89} & \overbrace{\begin{bmatrix} M_T \\ 8 \times 8 \end{bmatrix}}^{89 \times 1} \\ \overbrace{\begin{bmatrix} 0 \\ 8 \times 81 \end{bmatrix}}^{89 \times 81} & \overbrace{\begin{bmatrix} K_T \\ 8 \times 8 \end{bmatrix}}^{89 \times 1} \end{bmatrix} \begin{bmatrix} \{ d \} \\ \{ T_a \} \end{bmatrix} = \begin{bmatrix} \{ F_{ext} \} \\ \{ H_{ext} \} \end{bmatrix} \quad (5.52)$$

where three displacement degrees of freedom are allowed at all 27 nodes of the 27/8 finite element (shown in Figure 5-4), but only 8 corner nodes have temperature degree of freedom. In alternate form, this may be expressed as

$$\begin{bmatrix} 0 & 0 \\ 0 & [C_H] \end{bmatrix} \begin{bmatrix} \{ \dot{d} \} \\ \{ \dot{T}_a \} \end{bmatrix} + \begin{bmatrix} [K_u]\{d\} + [M_T]\{T_a\} \\ [K_T]\{T_a\} \end{bmatrix} = \begin{bmatrix} \{ F_{ext} \} \\ \{ H_{ext} \} \end{bmatrix} \quad (5.53)$$

In subsequent discussions, it is convenient to condense Eqn. (5.53) into the following form

$$A \dot{d} + g(d) = h(t) \quad (5.54)$$

where

$$A = \begin{bmatrix} 0 & 0 \\ 0 & [C_H] \end{bmatrix} \quad d = \begin{bmatrix} \{ d \} \\ \{ T_a \} \end{bmatrix} \quad \dot{d} = \begin{bmatrix} \{ \dot{d} \} \\ \{ \dot{T}_a \} \end{bmatrix} \quad (5.55)$$

and

$$g(d) = \begin{bmatrix} [K_u]\{d\} + [M_T]\{T_a\} \\ [K_T]\{T_a\} \end{bmatrix} \quad h(t) = \begin{bmatrix} \{ F_{ext} \} \\ \{ H_{ext} \} \end{bmatrix} \quad (5.56)$$



Therefore, it becomes a first order ordinary differential equation (ODE) and we now determine the solution of an initial value problem. Given  $d_0 = d(0)$ , find  $d = d(t)$ , such that  $A\dot{d} + g(d) = h(t)$ . Eqn. (5.54) is a system of first order ODEs that can be numerically solved by discretizing the time domain into finite time intervals,  $\Delta t_k = t_{k+1} - t_k$ , where the temporal solutions are approximated as  $d_{k+1} \approx d(t_{k+1})$  and  $v_{k+1} \approx \dot{d}(t_{k+1})$ .

Defining

$$\begin{aligned} d^* &= Ad, \quad \dot{d}^* = A\dot{d}, \\ \text{and} \\ f^* &= Af(d, t) = h(t) - g(d) \end{aligned} \quad (5.57)$$

we transform Eqn. (5.54) into

$$\dot{d}^* = f^*(d, t) \quad (5.58)$$

Introducing the general linear k-step method (Borja 1991) that approximates the solution of ODEs of the first order

$$\sum_{m=0}^k \left( \alpha_m \dot{d}_{n+1-m}^* + \Delta t \beta_m f_{n+1-m}^* \right) = 0 \quad (5.59)$$

where  $\alpha_m$  and  $\beta_m$  are unknown coefficients. Therefore, substituting Eqn. (5.57)

back into the above equation gives

$$A \sum_{m=0}^k (\alpha_m d_{n+1-m}^*) + \sum_{m=0}^k \Delta t \beta_m (h_{n+1-m} - g_{n+1-m}) = 0 \quad (5.60)$$

which is equivalent to the following matrix form

$$\begin{bmatrix} 0 & 0 \\ 0 & [C_H] \end{bmatrix} \sum_{m=0}^k \alpha_m \begin{bmatrix} \{d\} \\ \{T_a\} \end{bmatrix}_{n+1-m} + \sum_{m=0}^k \Delta t \beta_m \begin{bmatrix} \{F_{ext}\} - [K_u] \{d\} - [M_T] \{T_a\} \\ \{H_{ext}\} - [K_T] \{T_a\} \end{bmatrix}_{n+1-m} = 0 \quad (5.61)$$

Also, in component form, Eqn. (5.60) is equivalent to

$$[K_u] \{d\}_{n+1-m} + [M_T] \{T_a\}_{n+1-m} = \{F_{ext}\}_{n+1-m} \quad (5.62)$$

and letting  $\alpha_0 = -1$  and  $\beta_0 = \beta_1 = \beta_2 = \dots = \beta_k$  and  $\beta_0 \neq 0$ , we have

$$[C_H] \left( \{T_a\}_{n+1} - \sum_{m=1}^k \alpha_m \{T_a\}_{n+1-m} \right) + \Delta t \beta_0 [K_T] \{T_a\}_{n+1} = \Delta t \beta_0 \{H_{ext}\}_{n+1} \quad (5.63)$$

Because the equilibrium components of  $(h_{n+1-m} - g_{n+1-m})$  for  $m = 1, 2, \dots, k$  vanish

from the previous time step  $t_n$ , the linear momentum and the energy balance must be ensured at  $\{d\}_{n+1}$  such that

$$f(d_{n+1}) = \begin{bmatrix} \{F_{ext}\}_{n+1} - [K_u] \{d\}_{n+1} - [M_T] \{T_a\}_{n+1} \\ \Delta t \beta_0 \{H_{ext}\}_{n+1} - \Delta t \beta_0 [K_T] \{T_a\}_{n+1} - \beta_0 [C_H] \psi(\{T_a\}_{n+1}) \end{bmatrix} = 0 \quad (5.64)$$

where  $\psi(\{T_a\}_{n+1}) = \frac{1}{\beta_0} \left( \{T_a\}_{n+1} - \sum_{m=1}^k \alpha_m \{T_a\}_{n+1-m} \right)$ . Eqn. (5.64) is then solved by

using the Newton-Raphson method, linearizing Eqn. (5.64) to solve for  $d_{n+1}^{j+1}$  of the  $j+1$ -th iteration yields

$$f(d_{n+1}^{j+1}) = f(d_{n+1}^j) + \frac{\partial f(d_{n+1}^j)}{\partial d_{n+1}} \overline{\Delta d_{n+1}} + O(h^2) \quad (5.65)$$

When it converges, that is,  $f(d_{n+1}^{j+1}) \approx 0$ , the formula becomes

$$\Delta d_{n+1} = - \left( \frac{\partial f(d_{n+1}^j)}{\partial d_{n+1}} \right)^{-1} f(d_{n+1}^j) \quad (5.66)$$

Or,

$$[K^{**}]\{\Delta d'_{n+1}\} = \{r'_{n+1}\} \quad (5.67)$$

where  $[K^{**}]$  represents a global stiffness matrix that contains

$$[K^{**}] = \left( \frac{\partial f(d'_{n+1})}{\partial d_{n+1}} \right) = \begin{bmatrix} [K_u] & [M_T] \\ [0] & \Delta t \beta_0 [K_T] + [C_H] \end{bmatrix} \quad (5.68)$$

and the residual force vector  $\{r\}$  is defined as

$$\{r'_{n+1}\} = \{f(d'_{n+1})\} = \begin{bmatrix} \{F_{ext}\}_{n+1} - [K_u]\{d\}_{n+1}^j - [M_T]\{T_a\}_{n+1}^j \\ \Delta t \beta_0 \{H_{ext}\}_{n+1} - \Delta t \beta_0 [K_T]\{T_a\}_{n+1}^j - \beta_0 [C_H]\psi(\{T_a\}_{n+1}^j) \end{bmatrix} \quad (5.69)$$

Thus, if  $\{d'_{n+1}\}$  at the current  $j$ -th iteration does not satisfy the equilibrium, e.g.,

$\{r'_{n+1}\} \neq 0$  or  $\{r'_{n+1}\} > tolerance$ , then it will be updated as  $\{d'^{j+1}_{n+1}\} = \{d'^j_{n+1}\} + \{\Delta d'_{n+1}\}$  in

subsequent iteration until convergence is reached.

### 5.10 3-D Finite Element Thermoelastic Stress Analysis

In this section, transient thermo-mechanical stress analysis is performed using a three-dimensional (3-D) finite element, i.e., the 27/8 element shown in Figure 5-4, which has been developed and coded in the PLASFEM. In the following, a reinforced concrete column exposed to fire will be modeled using this 3-D finite element.

#### 5.10.1 Model description

A square cross-section (380x380 mm) reinforced concrete column exposed to a radiant fire condition shown in Figure 5-5 (see also Chapter 4) is modeled. The size of longitudinal bars is a no. 6 bar and ties of no. 3 bars are provided and served as shear reinforcement for the reinforced concrete column. The vertical spacing of ties

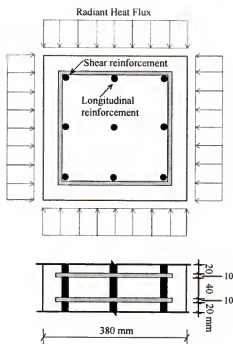


Figure 5-5 A reinforced concrete column exposed to radiant heat

used in the model is 40 mm. The ends of the ties are lap sliced with corner hooks that are idealized as perfectly anchored by a sharp 90° bend around a bar. Confining effects in the concrete core and interface between the longitudinal bars and the ties are not considered in the finite element analysis. More importantly, the effects of steel reinforcement on hydro-thermal behavior of concrete are considered in order to quantitatively identify the influence of heterogeneity of reinforced concrete structural elements on the thermodynamic state of the system and thus, the influence on the development of thermally induced stress field.

Secondly, because of the symmetry of the geometry and the thermal loading conditions, a partial symmetry model of the actual column segment is developed (illustrated in Figure 5-6) as a single quadrant mesh symmetric in both the  $xz$ - and the  $xy$ -plane. Figures 5-6a and 5-6c illustrate the finite element mesh layout in a plane view at two different  $y$ -coordinates, i.e.,  $y=2.5$  mm and  $y=20.0$  mm, respectively. In

subsequent discussion, the plane view shown in Figure 5-6a is referred as Plane A while the one shown in Figure 5-6b is referred as Plane B.

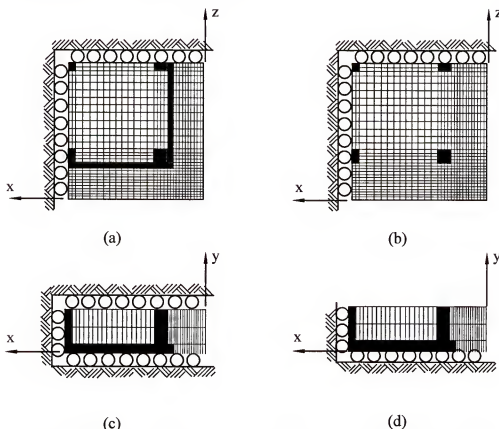


Figure 5-6 3-D finite element models of the concrete column segment

As discussed earlier in this chapter, the degree of constraint provided by the boundaries of the column segment will affect the thermal-dilation related stresses that are computed. Once again, two different sets of boundary conditions that bracket realistic field conditions (e.g., material constraint) are considered. In the first case (Figure 5-6c), vertical expansion is completely restrained, while in the second (Figure 5-6d), the top of the column segment is free to expand. At a plane of geometric symmetry, mechanical displacement boundary conditions for the symmetric thermal loading are modeled such that no translational motion is allowed perpendicular to a plane of geometric symmetry (Figure 5-6).

### 5.10.2 Modeling of the transient thermal loading condition

Using TOUGH2 to solve the coupled heat and moisture flow equations yields a complete time-varying description of the temperature field throughout three-dimensional directions of the column. Temperature data from the three-dimensional TOUGH2 model (refer to Chapter 4) is then mapped onto nodes located in the finite element thermal stress models. For each finite element model nodal point, a complete time-history of temperature is extracted from the TOUGH2 simulation results and is then applied to the finite element model as a time-varying prescribed nodal temperature  $\{T_a^{prescribed}\}$ . Time-varying thermal stress analyses are then performed for each boundary condition model to compute time-histories of thermal stresses throughout the three-dimensional meshes. At each time step, the following system equation is solved

$$[K_u]\{d\}_{n+1} = \{F_T\}_{n+1} \quad (5.70)$$

where

$$\{F_T\}_{n+1} = \int_v [B]^T \{\beta\} [\hat{N}] d\Omega \cdot \{T_a^{prescribed}\}_{n+1} \quad (5.71)$$

Therefore, we compute thermal stresses at time  $t_{n+1}$  through the relationships

$$\{\sigma\}_{n+1} = [C]\{\varepsilon\}_n - \{\beta\} \Delta T_{n+1} \quad (5.72)$$

where  $\{\varepsilon\}_n = [B]\{d\}_n$  and  $\Delta T_{n+1}$ , temperature change at a point of interest in the natural coordinate system at time  $t_{n+1}$ , is computed

$$\Delta T_{n+1}(r, s, t) = \sum_{i=1}^8 \hat{N}_i(r_i, s_i, t_i) \cdot \left( (T_i^{prescribed})_{n+1} - (T_i^{prescribed})_n \right) \quad (5.73)$$

### 5.10.3 Simulation results

As demonstrated earlier in the case of 2-D axisymmetric finite element stress analysis, computation of effective stresses using the principle of superposition described by Eqn. (5.12) requires that pore pressures be combined with stresses that are induced by thermal dilatation and boundary condition restraint. First, the thermal-dilatation total stress computed by finite element analysis is taken as  $\sigma$  since it represents the macroscopically averaged effect of thermal dilation and boundary constraint. Then, Eqn. (5.12) is used to combine (or superimpose) thermal stresses with pore pressures separately computed using the 3-D finite difference model described in Chapter 4. Thus, in the subsequent discussion, both maximum and minimum principal stresses represent principal values of the effective stress tensor  $\sigma''$ .

Figure 5-7 and Figure 5-8 show maximum principal stresses  $\sigma_1$  developed in the case of a fully constrained boundary condition imposed on y-direction displacements shown in Figures 5-6c. This case will be referred as the fixed boundary condition case. Maximum principal stresses  $\sigma_1$  computed in both Plane A (Figure 5-6a) and Plane B (Figure 5-6b) vary in a range from 40 MPa to 80 MPa. at time  $t=200$  sec. after all the four sides of the column initially exposed to a fire. Owing to large effective tensile stresses acting normal to the xz-plane, i.e.,  $\sigma''_{yy}$ , the severe maximum principal stresses acting on the principal xz-plane are developed in the concrete cover zone of the column segment. One particularly noteworthy feature of the thermally-induced stress field is severe development of effective tensile stress  $\sigma''_{yy}$  in the near-

surface regions along the surface of the column segment and in the near-corner regions.

Figures 5-9 and 5-10 show maximum principal stresses  $\sigma_1$  developed in the case of no constraint imposed on the top boundary of the column segment as shown in Figures 5-6d. In contrast to the fixed boundary condition case, maximum tensile stress components of the effective stress tensor computed in the near-surface regions are  $\sigma_{xx}''$  and  $\sigma_{zz}''$  rather than  $\sigma_{yy}''$ . Thus, large effective tensile stresses are developed perpendicular to the yz-plane, i.e.,  $\sigma_{xx}''$ , and mainly contribute to the maximum principal stress in the surface region along the x-coordinate. However, acting perpendicular to the xy-plane,  $\sigma_{zz}''$  is found to be the dominant tensile stress component along the z-coordinate. This reveals that characteristics of the stress field developed in the free boundary condition case, the development of dominant tensile stress component is direction-dependent, but results in the development of large maximum principal stresses in the surface regions. It is noted that the peak value of maximum principal stress in the corner region is only one-quarter the magnitude of what is computed in the fixed boundary condition case. Thus, in the fixed boundary condition case, more severe tensile effective stresses  $\sigma_{yy}''$  is thermally induced in the y-direction perpendicular to the symmetric xz-plane near the corner region of the column segment.

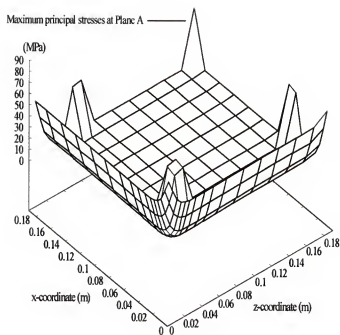
Comparing these maximum principal stresses within the first 10 mm of depth in both boundary condition cases, significant changes in magnitude and trend are found in the stress field. It appears that less severe thermal stresses develop in the free boundary condition case. No significant tensile stress was developed in regions near



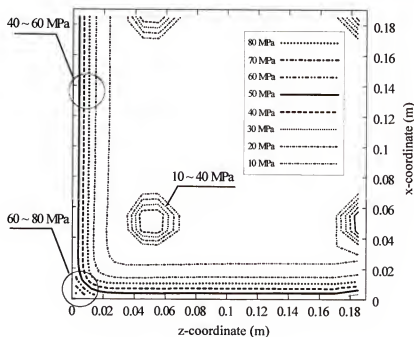
the locations of the longitudinal bars in the free boundary condition case due to free expansion (e.g., Figure 5-8 vs. Figure 5-10). One noteworthy feature of thermally-induced stress fields computed for both the boundary condition cases is that the maximum principal values of the stresses would exceed the ultimate tensile strength of a typical high-strength concrete—not accounted for in the linear elastic analyses conducted here—and failure would thus occur before these stress levels could be reached.

The influence of non-uniform temperature field on the development of compressive stress is discussed. As already seen in the 2-D axisymmetric study, the general trends of stress contour of the minimum principal stress  $\bar{\sigma}_3$  at time  $t=200$  sec. are found to be quite similar in both the fixed (Figures 5-11 and 5-12) and the free (Figures 5-13 and 5-14) boundary condition cases. The magnitudes of compressive normal stresses  $\sigma_{xx}''$  and  $\sigma_{zz}''$  computed in the concrete region in the vicinity of shear reinforcement (steel shear ties) are not significantly different in the two cases. With steep temperature gradients, the outer-surface regions expand and such an expansion cannot proceed freely in the relatively cooler regions, the inward thermal expansion of the outer surface region is suppressed in the  $xz$ -plane by the cooler inner concrete. This results in significant development of compressive stresses  $\sigma_{xx}''$  and  $\sigma_{zz}''$  in the concrete in the vicinity of shear reinforcement, which are acting normal to the surface exposed to fire.

However,  $\sigma_{yy}''$  that is developed in the same region of the fixed boundary condition case is the dominant tensile stress component of the effective stress tensor, which contributes to the development of large maximum principal stresses  $\sigma_1$  shown

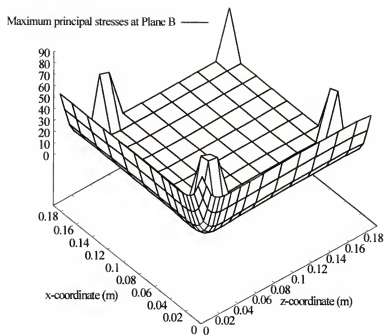


(a) Maximum principal stresses in Plane A of the fixed boundary case

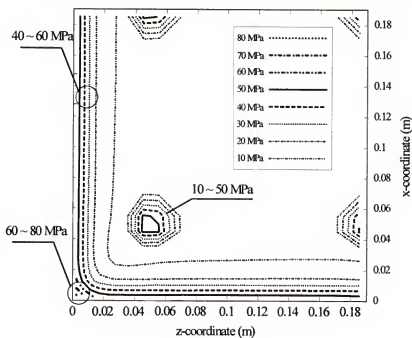


(b) Stress contour in the Plane A

Figure 5-7 Maximum principal stresses at  $t=200$  sec. (fixed boundary)

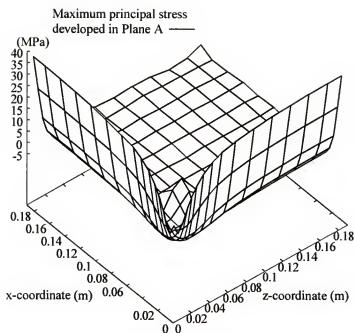


(a) Maximum principal stresses in Plane B of the fixed boundary case

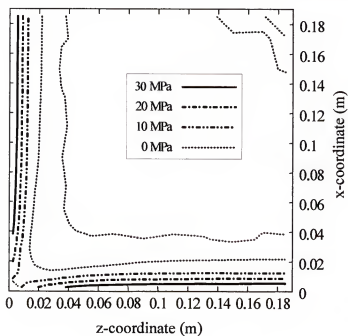


(b) Stress contour in the Plane B

Figure 5-8 Maximum principal stresses at  $t=200$  sec. (fixed boundary)

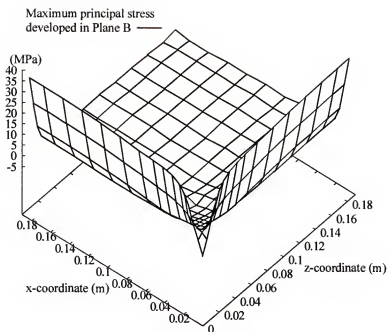


(a) Maximum principal stresses in Plane A of the free boundary case

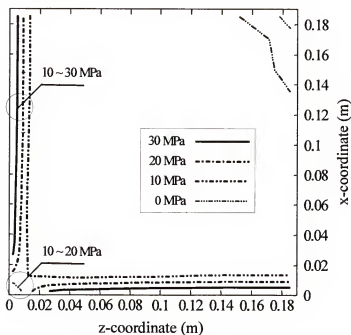


(b) Stress contour in the Plane A

Figure 5-9 Maximum principal stresses at  $t=200$  sec. (free boundary)



(a) Maximum principal stresses in Plane B of the free boundary case



(b) Stress contour in the Plane B

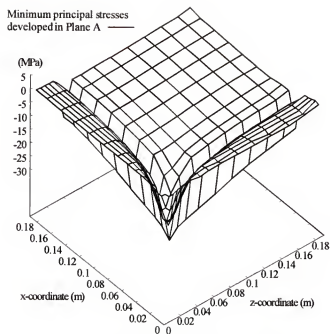
Figure 5-10 Maximum principal stresses at  $t=200$  sec. (free boundary)

in Figure 5-8. Thus, a state of stress where  $\sigma_1$  and  $\sigma_3$  have opposite signs is developed particularly in the concrete regions adjacent to shear reinforcement. Subsequently, the shear stress component  $\sigma_{xz}''$ , having a magnitude as significant as tensile normal stress component  $\sigma_{yy}''$  is observed in the effective stress tensor developed in that region.

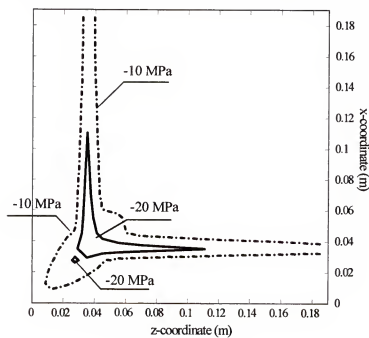
For the free boundary condition case, tensile  $\sigma_{yy}''$  is almost negligible in the near-surface region where the dominant tensile stresses are rather  $\sigma_{xx}''$  and  $\sigma_{zz}''$ . Small compressive  $\sigma_{yy}''$  is developed in the corner region where  $\sigma_{xx}''$  and  $\sigma_{zz}''$  also become compressive. Since three normal stress components are compressive in the corner region, a state of stress is developed where maximum principal stress  $\tilde{\sigma}_1$  and minimum principal stress  $\tilde{\sigma}_3$  have same negative signs. Thus, there is a small region of the inner corner where the pure compression occurs in the free boundary condition case.

#### 5.10.4 Summary

The boundary constraint imposed on the y-direction displacement of the column segment is found to be very influential in development of a state of thermal-dilatation stresses in the 3-D model. The minimal differences in magnitude and the similarity in trends between the results of minimum principal stresses are found while significant differences in development of tensile stresses are noticed by observation in the distributions of the maximum principal stresses. Examination of the effective stress distributions at various spatial-temporal locations in Plane B in both the fixed and free boundary conditions case reveals the effects of the boundary condition on the

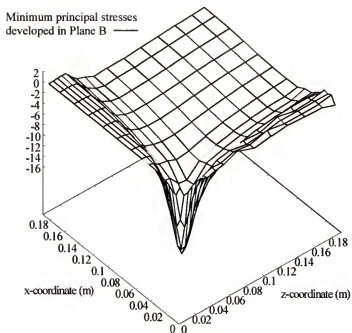


(a) Minimum principal stresses in Plane A of the fixed boundary case

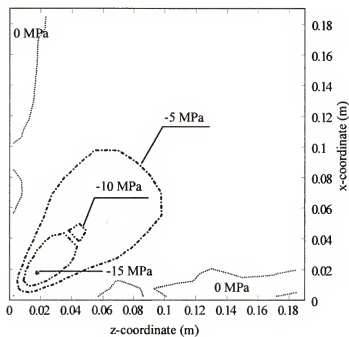


(b) Stress contour in the Plane A

Figure 5-11 Minimum principal stresses at  $t=200$  sec. (fixed boundary)



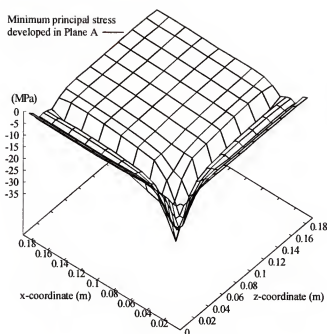
(a) Minimum principal stresses in Plane B of the fixed boundary case



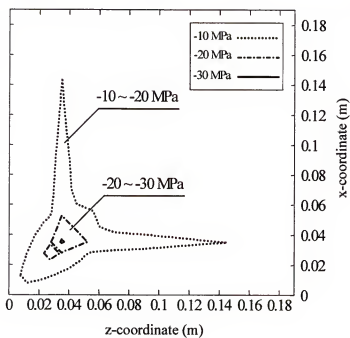
(b) Stress contour in the Plane B

Figure 5-12 Minimum principal stresses at  $t=200$  sec. (fixed boundary)



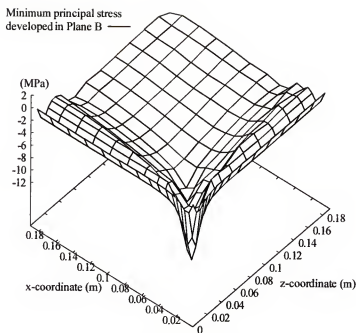


(a) Minimum principal stresses in Plane A of the free boundary case

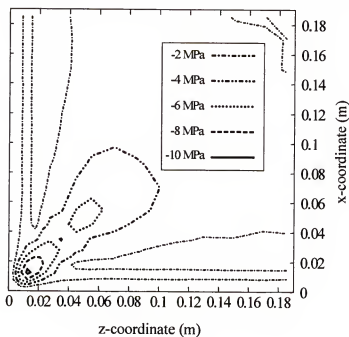


(b) Stress contour in the Plane A

Figure 5-13 Minimum principal stresses at  $t=200$  sec. (free boundary)



(a) Minimum principal stresses in Plane B of the free boundary case



(b) Stress contour in the Plane B

Figure 5-14 Minimum principal stresses at  $t=200$  sec. (free boundary)

development of the effective stresses, particularly two effective stress components, i.e.,  $\sigma''_{yy}$  and  $\sigma''_{xz}$ .

First, the stress component  $\sigma''_{yy}$  in the effective stress tensor is noticeably affected by the boundary constraint. Steep temperature gradient induced by a high rate of heating combined with the boundary restraint and internal pore-pressure buildup, the effective stress component  $\sigma''_{yy}$ , which is acting parallel to the surfaces of fire exposure, is found to exceed a typical tensile strength of high-strength concrete at early stages during fire exposure. In addition,  $\sigma''_{yy}$  is the dominant tensile stress component in the development of maximum principal stress than any other stress components in the fixed boundary condition case.

Secondly, the same normal stress component  $\tilde{\sigma}_{yy}$  in the free boundary condition case is rather insignificant compared to the other normal stress components in the development of thermal effective stresses. In planes parallel to the surfaces exposed to fire,  $\sigma''_{xx}$  acting on the yz-plane and  $\sigma''_{zz}$  acting on the xy-plane are the dominant tensile stress components that mainly contribute to the maximum principal stresses in the near-surface regions. However, we found these normal stresses less significant in inner layers of the concrete cover. The shear stress  $\sigma''_{xz}$  increases as those normal stresses decrease in the vicinity of the shear reinforcement.

Therefore, considering the degree of restraint provided by the column boundaries, an actual state of stress field in realistic field conditions is thought to be bracketed by the thermal-dilation related stresses that are computed for two different sets of boundary conditions. Hypothetically, if brittle material failure of high-strength

concrete associated with thermally induced stress would take places in the concrete column, then it would be tensile fracture due to severe development of effective tensile stresses,  $\bar{\sigma}_{yy}$ , normal to the xz-plane where fracture planes could be formed most likely first in the near-surface corner regions of the column.

## CHAPTER 6

### CONTRIBUTION OF PORE PRESSURE AND THERMAL GRADIENT STRESS TO SPALLING

Inconsistent occurrence of explosive spalling has been observed in the past tests of high-strength concrete (Phan and Carino 2002). In regard to the thermal behavior of high-strength concrete, the effect of low permeability on transport phenomena leading to pore pressure buildup was suspected to be main cause for higher susceptibility of high-strength concrete to explosive spalling. This chapter addresses the contribution of high pore-pressure buildup and thermal gradient stress to thermal spalling of high strength concrete, based on the results obtained in this study.

#### 6.1 Factors Influencing Spalling at Early Stages of Heating

Based on the linear thermo-elastic stress results presented in Chapter 5, the pore pressure associated with moisture transport phenomena at early stages of heating (during the first five minute fire exposure) is found to have nearly negligible effects on the development of the effective stress tensor compared to the magnitude of thermal-dilatation stress components. A most significant factor of spalling at *an early stage of heating* is thermal gradient stresses that can cause fracture failure.

The effects of moisture on the temporal temperature distributions result in very significant changes of thermally induced stress field. As investigated using an axisymmetric finite element analysis in the previous chapter, the magnitudes of thermally induced stresses at  $t=200$  sec. ranging from 30 MPa (4.4 ksi) to 80 MPa (11.6 ksi) could

well exceed a typical tensile strength of high-strength concrete. Failure to include the effects of moisture in the process of determining temperature distribution results in numerical predictions of thermal gradient stresses that are nearly fifty per cent greater at early stages of thermal loading (refer to Chapter 5). This over-estimation of thermal gradient stress values becomes more exaggerated as thermal loading continues. Therefore, the influence of moisture migration and evaporation on heat transfer must be considered in order to obtain valid numerical predictions of thermal-dilatation stresses.

The effects of temperature distribution combined with boundary restraints on hydro-thermo-elastic stresses have been identified. Thermal gradient stresses increase with temperature gradient. However, the temperature prediction by a conventional transient thermal analysis is higher than by the coupled moisture and heat transport analysis. This leads to even steeper development of thermal gradients and thus causes overestimation of thermal gradient stresses. Numerically predicted and macroscopically volume-averaged pore pressure has nearly negligible effects on development of the maximum principal stress during the first five minutes of fire exposure. Although magnitudes of pore pressure buildup are much lower than those of thermal gradient stresses, one should not simply neglect the effects of moisture in thermal analysis. It has been found that moisture movement affects temperature rise and gradient development. Therefore, coupled heat and mass transfer processes are involved in the development of pore pressure establish the thermodynamic states of high-strength concrete when exposed to elevated temperatures (Chung and Consolazio 2004).

It is noted that the magnitudes of thermo-elastic gradient stresses, predicted by the present finite element stress analysis model, in the near surface of the columns may be overestimated. Young's modulus of elasticity of cover concrete decreases as temperature increases (Phan et al. 2001, Janotka and Bágel 2002). The combined effect of thermal strains that increase as temperature differentials increase and Young's modulus of elasticity of concrete that decreases at an elevated temperature needs to be investigated for more accurate assessment of thermal dilatation induced stresses. Reduction of concrete strength in both compression and tension should be considered in order to determine the locations and time of spalling. The assessment of compatibility needs to be investigated further in regard to 1) constituents of reinforced concrete and 2) the geometry of the structural members. For example, the differences in thermal expansion between cement paste and aggregate, and between mortar and steel reinforcement could cause interfacial bond failure. For a *rectangular* column, thermal expansion will be smaller along a shorter dimension of the cross-section than along the longer dimension of the cross-section. Thus, an increase in compression in the longer dimension will result whereas a decrease in compression or even tensile forces can result in the shorter direction (Usmani et al. 2001).

## **6.2 Contribution of Pore Pressure at a Later Stage of Heating**

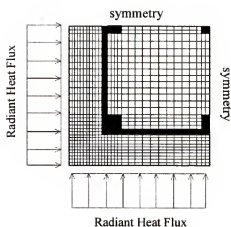
Another scenario of spalling can be drawn when pore pressures become quite substantial under a sustained thermal loading condition. Potential influence of pore pressures on spalling has been investigated under an assumption that the concrete cover remains in place until the pore pressures build up significantly.

Figures 6-1 and 6-2 illustrate the thermodynamic field variables developed in two different locations after time  $t=600\text{sec.}$  (10 minutes) when all the four sides of the square column discussed in Chapter 5 (refer to Figure 5-6) are initially exposed to a hydrocarbon pool fire modeled using ASTM E1529. In contrast to negligible values of pore pressure at an early stage of heating (i.e.,  $t=200\text{ sec.}$ ), numerically computed volume-averaged pore-pressure buildup in a plane where shear reinforcement is located (Figure 6-1a) exceeds 4 MPa (0.58 ksi) at time  $t=400\text{ sec.}$  and reaches 5.5 MPa (0.8 ksi) at time  $t=600\text{ sec.}$  (Figure 6-1b). Interestingly, the development of peak pore pressure is predicted along the interfaces between concrete and shear reinforcement parallel to the surfaces exposed to fire.

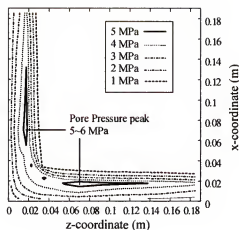
Similar trends of pore pressure are found in a plane located at 20 mm vertically above the shear reinforcement (Figure 6-2a). Occurring in the corner region of the square column, the maximum value of volume-averaged pore pressure in Plane B exceeds 6.7 MPa (0.97 ksi) at time  $t=600\text{sec.}$  (10 minutes).

Unexpectedly, as heating continues, higher pore pressure is developed in the concrete region between adjacent shear ties (Plane B) in the column than in the vicinity of the shear reinforcement (Plane A). The shear reinforcement was indeed blocking horizontal moisture flow in the  $xz$ -plane and forced the moisture to permeate vertically in the directions parallel to the column surfaces. According to experimental works by Elvery et al. (1973) and Butler (1981), the pore pressure, averaged using the *effective porosity* at tensile failure of high-permeability concrete, was measured in a range of 1.5~2.5 MPa. The pore pressure alone predicted by the present study could cause tensile failure of concrete.

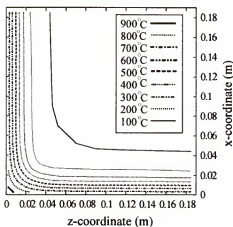




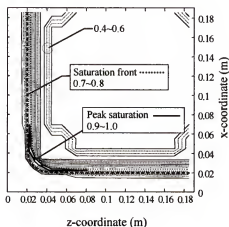
(a) Finite difference model



(b) Pore pressure



(c) Temperature



(d) Saturation

Figure 6-1 Thermodynamic states of a square column segment at  $t=600$  sec. (data plotted for Plane-A of Figure 5-6)

In addition, the pore pressure distributions with respect to formation of saturation fronts are identified in Figures 6-1d and 6-2d. It is noted that locations of maximum pore pressure buildup are found to be within a two-phase zone of finite length away from the column surface adjacent to locations where the degree of saturation maximizes (Pruess et al. 1987). Very similar temperature distributions are observed in both Plane A and Plane B (Figures 6-1b and 6-2b).

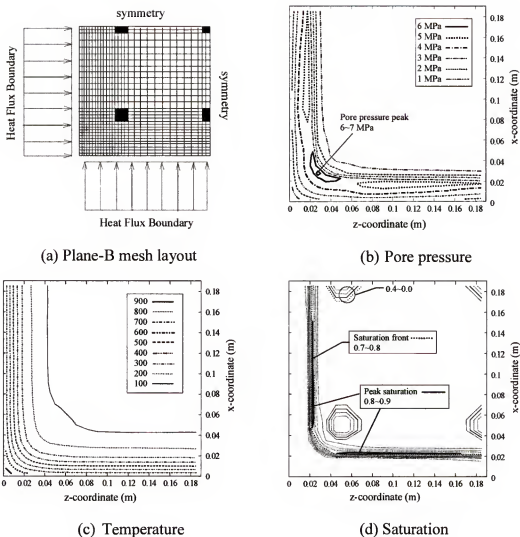


Figure 6-2 Thermodynamic states of a square column segment at  $t=600$  sec. (data plotted for Plane-B of Figure 5-6)

Comparing Figure 6-1d to Figure 6-2d, we observe more prominent development of moisture clogging near the shear reinforcement in Plane A. Note that this liquid water saturation is just barely below the maximum theoretical value of unity. A wall of moisture constituting a form of “heat sink” is formed as shown in Figure 6-3. Therefore, a large amount of thermal energy is consumed in the evaporation process of liquid water that is retained by moisture clogging and subsequently temperature rise in the moisture-clogged region is retarded. This results

in a significant reduction of thermal gradients and thus magnitudes of thermal gradient stresses whereas pore pressure continues to increase. It is concluded that at a later stage of heating when moisture clogging becomes prominent, the contribution of pore pressure to spalling is significant. Violent fracture failure (i.e., explosive spalling) of high strength concrete has been reported during the first 10–20 minutes of building fire exposure in field and laboratory tests (Kodur 1999, Chana and Price 2003). In their tests, large areas of steel reinforcement were exposed and concrete continued to spall. With decreasing severity, this explosive spalling was observed until 25 minutes after ignition. The combined effects of thermal dilatation induced stresses and pore pressure result in a continuation of explosive spalling.

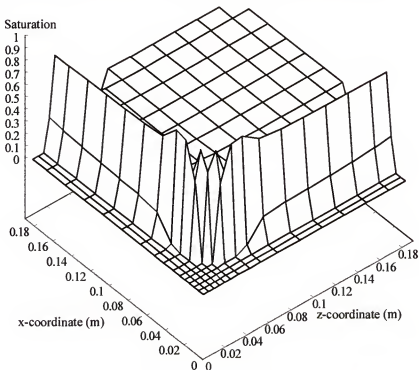


Figure 6-3 Moisture clog formed in a square column

One factor influencing pore pressure, which has not been investigated here, is the significant increase of material flow parameters such as the permeability of

concrete at high temperatures (Phan and Carino 1998, Janotka and Bágel 2002). Expansion of micropore volume and cracking induced by shrinkage (occurring on loss of moisture due to dehydration of cement gels at high temperatures) are phenomena that cause a sudden increase of the permeability of concrete. Thus, the values of the pore pressure predicted by present models may be higher than those actually occurring in high-strength concrete (Consolazio et al. 1998, Kalifa et al. 2000). Nonetheless, the material model developed in this study can be further improved when additional experimental data, particularly permeability of high-strength concrete at elevated temperatures, are available. Completely defining the role of pore pressure in initiating spalling will require additional investigation and experimental testing.

## CHAPTER 7 CONCLUSION

An improved quantitative understanding of multi-dimensional states of stress inside reinforced concrete structural elements under severe fire condition has been obtained in this study. The combined finite difference and finite element model developed in this study provided valuable insights into hydrothermal behavior of reinforced high-strength concrete structural elements. By developing thermo-elastic stress analysis techniques for concrete structural elements exposed to severe fire, this research has focused on the development of a practical computer methodology that can be used to study concrete thermal spalling. Thermal mechanisms such as thermal expansion and thermal bowing have been found to produce severe stress states (large compressive or tensile stresses) depending on the temperature distribution in the concrete member and boundary restraint conditions.

A comprehensive theoretical understanding of how elevated temperatures generated during a fire affect the thermodynamic state of concrete has been established during this research. By establishing practical models that take into account the fluid flow and thermal properties of concrete, the effects of coupled moisture and heat transport phenomena occurring in heated high-strength concrete have been studied.

Components of the research involved studies of material characteristics of concrete as a porous medium and effects of multiphase flow on magnitude of pore-pressure build up, development of thermal gradients, and evolution of degree of saturation. Also, the

effects of thermal exposure conditions such as rate of heating and thermodynamic conditions of concrete in ambient conditions (e.g., initial degrees of saturation at various levels of relative humidity) were examined.

Using thermodynamic state data obtained from the computer finite difference models, the influence of thermally induced stresses on spalling has been investigated in consideration of the location of steel reinforcement, geometrical structural shapes, and constraints on the structural element. In the following, concluding remarks of this study are stated in regard to the influence of thermally induced stress on spalling. Discussion of future research areas in relation to the numerical methodology proposed in this study is then provided.

### **7.1 Thermal Spalling of Concrete**

The effects of thermal exposure conditions such as rate of heating and initial thermodynamic conditions of concrete (e.g., saturation) have been found to be significant factors that influence moisture flow inside heated concrete. The important role of moisture has been identified by simulation results of thermal-dilatation stresses in reinforced concrete columns. Due to low conductivity and high heat capacity of partially saturated concrete, the rate of heat transfer is very low. Accumulation of thermal energy results in the development of a steep thermal gradient in the concrete cover, which can be even more intensified by rapid rate heating. A large amount of thermal energy is consumed by the evaporation process of moisture in concrete pores. Maximum temperature rise in the near-surface region is affected as is the development of the associated temperature gradient.

As detailed in earlier chapters, after a few minutes of fire exposure, moisture clogging occurs. Severe and early formation of moisture clogging is found in the case of high-strength concrete more than in the case of normal strength concrete exposed to fire. Several factors including lower permeability and higher degree of initial saturation at an ambient condition create a pseudo heat sink and impermeable boundary inside high-strength concrete. Thus, the formation of a moisture clog is closely related with, and directly affects the rate of temperature rise and pore-pressure development.

The influence of pore-pressure on thermal spalling of high-strength concrete has been examined. By means of linear thermoelastic analysis, the contribution of the pore pressure buildup to the effective stresses during the first five minutes of fire exposure has been found to be negligible compared to that of thermal dilatation stresses. Based on stress analysis results presented herein, thermally induced spalling appears to be primarily driven by thermal dilatation stresses, not by pore pressure. Development of thermal gradient stresses has been found to be significantly influenced by boundary restraint conditions. Another important factor that could affect thermal spalling of structural concrete members has also been investigated. Restraint conditions have been found to have a significant effect on the development of internal forces and the displacements. For instance, boundary constraints such as vertical restraints imposed on the 3-D column segment model and the 2-D axisymmetric column model produce large tension forces when steep thermal gradient is developed in the outer hotter region of the columns. For the source of structural restraints, it is not so clear whether sufficient restraints would remain available as temperature rises. This is an area that needs to be investigated further.

Effects of moisture on development of thermal stresses have been confirmed and considered in multi-dimensional finite element stress analyses. Thus, the effects of moisture movement on thermal stresses should be considered in determination of the effective stresses due to 1) influence in pore pressure, 2) potential association with crack growth in the fracture processes, and most importantly 3) determining the distribution of temperature.

It must be noted that within this study, any prediction of material failure involved in thermal spalling would be limited by the present linear elastic stress analysis.

Temperature dependency of the key material thermo-mechanical parameters and failure mechanisms associated with the material strength parameters should be considered in future research to quantitatively determine more accurate stress fields. In addition, in order to determine whether a structural element will be safe under a severe thermal loading, the state of stress should be computed at all critical points of the structural element, i.e., at all points where stress concentrations are likely to occur. This may be done in a number of ways by using *stress concentration factors* when the theory of elasticity is used to determine the state of stress at each critical point.

When material failure induced by macroscopic cracks is considered in a structural element, special care needs to be taken. When a crack is initiated due to an initial fracture in a thermally loaded structural element, it is necessary to determine whether the macroscopic crack will tend to propagate under the expected loading condition and cause structural failure, or whether it will remain stable. This requires a computational analysis involving the fracture energy associated with the growth of the crack and inclusion of



both stress and internal pore pressure effects. Such an analysis is beyond the scope of this text and should be carried out by the methods of fracture mechanics.

## **7.2 Future Research Work**

This research has considered key issues related to fire induced spalling of reinforced concrete structural elements in extreme fire events. A new numerical methodology is presented to analyze heat and mass transport phenomena in concrete at high temperatures that results in predictions of mechanical behavior. The computational steps associated with the development of the numerical models can be further improved by considering

1. Computer modeling of changes in mechanical properties of high-strength concrete such as modulus of elasticity, tensile and compressive strength, Poisson's ratio, linear thermal expansion coefficient, and heat capacity coefficient at elevated temperatures, should be included in future models.
2. Computer modeling of changes in thermophysical properties such as permeability, thermal conductivity, specific heat, and density at high temperatures should be considered in the transient thermal analysis.
3. The model can be extended to predict material failure at high temperatures so as to determine the fire resistance of high-strength concrete. The effects of expansion of aggregates and shrinkage of cement paste can be incorporated in the thermo-mechanical stress analysis.
4. The effects of crack opening by thermal gradient stresses should be considered with the theory of thermofracture mechanics. Genuine efforts

must be made to include the influence of the pore-pressure buildup on tension cracking in the analytical solution for the governing equations.

The integrated computer analysis tool developed in this study—integration of TOUGH2 and PLASFEM—will serve as a basis for building an analytical model capable of modeling *progressive* material failure that has been found to be a significant component of spalling phenomenon in concrete structures exposed to fire.

## LIST OF REFERENCES

- Abdel-Rahman, A.K. and Ahmed, G.N. (1996), "Computational Heat and Mass Transport in Concrete Walls Exposed to Fire," Numerical Heat Transfer, Part A, No.29, pp. 373-395.
- Achenbach, J.D. and Bažant, Z.P. (1975), "Elastodynamic Near-Tip Stress and Displacement Fields for Rapidly Propagating Cracks in Orthotropic Materials," Journal of Applied Mechanics, Transaction of the ASME, Vol. 31, pp. 183-189.
- Allen, M.B., Behie, G.A., and Trangenstein, J.A. (1988), *Multiphase Flow in Porous Media*, Springer-Verlag, Inc., New York, NY.
- Andersburg, Y. (1997), "Spalling Phenomena of HPC and OC," International Workshop on Fire Performance of High-Strength Concrete, NIST Special Publication 919, National Institute of Standards and Technology, Gaithersburg, MD, Feb. 1997, pp. 69-73.
- Anderson, T.L. (1995), *Fracture Mechanics: Fundamentals and Applications* (2nd ed.), CRC Press LLC, Boca Raton, FL.
- ADINA. (2002), *ADINA Theory and Modeling Guide.*, Report ARD 02-7, ADINA Research and Development Inc., Watertown, MA.
- API. (1952), *Recommended Practice for Determining Permeability of Porous Media* (3rd ed.), API RP-27, American Petroleum Institute, New York, NY.
- ASTM. (1993), "Standard test methods for Determining Effects of Large Hydrocarbon Pool Fires on Structural Members and Assemblies," ASTM E 1529-93, *Annual Book of ASTM Standards*, American Society for Testing and Materials, West Conshohocken, PA, pp. 688-701.
- ASTM. (1995), "Standard Test Methods for Fire Tests of Building Construction and Materials," ASTM E 119-95a, *Annual Book of ASTM Standards*, American Society for Testing and Materials, West Conshohocken, PA, pp. 441-461.
- Baggio, P., Majorana, C.E., and Schrefler, B.A. (1995), "Thermo-Hygro-Mechanical Analysis of Concrete," International Journal for Numerical Methods in Fluids, Vol. 20, pp. 573-595.
- Bamforth, P.B. (1987a), "The Properties of High Strength Lightweight Concrete," Concrete, April, pp. 8-9.
- Bamforth, P.B. (1987b), "The Relationship between Permeability Coefficients for Concrete Obtained Using Liquid and Gas," Magazine of Concrete Research, Vol. 39, No. 138, pp. 3-11.

- Baroghel-Bouny, V. and Chaussadent, T. (1996), "Texture and Moisture Characterization of Hardened Cement Pastes and Concrete from Water Vapor Sorption Measurements, NATO ASI Series, Vol. 304, *The Modeling of Microstructure and Its Potential for Studying Transport Properties and Durability*, edited by H. Jennings, J. Kropp and K. Scrivener, Kluwer Academic Publishers, Boston, MA, pp. 241-255.
- Bathe, K.J. (1996), *Finite Element Procedures*, Prentice Hall, Inc., Upper Saddle River, NJ.
- Bažant, Z.P. (1975), "Pore-pressure, Uplift, and Failure Analysis of Concrete Dams," Symposium Criteria and Assumptions for Numerical Analysis of Dams, University of Wales, National Committee on Large Dams, Swansea, UK, pp. 782-808.
- Bažant, Z.P., Chern, J.C., and Thonguthai, W. (1981), "Finite Element Program for Moisture and Heat Transfer in Heated Concrete," Nuclear Engineering and Design, Vol. 76, pp. 183-191.
- Bažant, Z.P. (1984), "Design and Analysis of Concrete Reactor Vessels: New Developments, Problem and Trends," Nuclear Engineering and Design, Vol. 80, pp. 181-202.
- Bažant, Z.P. and Kaplan, M.F. (1996), *Concrete at High Temperatures: Material Properties and Mathematical Modeling*, Longman Group Limited, Essex, UK.
- Bažant, Z.P. (1997), "Analysis of Pore Pressure, Thermal Stresses and Fracture in Rapidly Heated Concrete," International Workshop on Fire Performance of High-Strength Concrete, NIST Special Publication 919, National Institute of Standards and Technology, Gaithersburg, MD, pp. 155-164.
- Bear, J. (1972), *Dynamics of Fluids in Porous Media*, Dover Publications, Inc., New York, NY.
- Bear, J. and Bachmat, Y. (1998), *Introduction to Modeling of Transport Phenomena in Porous Media*, Kluwer Academic Publishers, Dordrecht, The Netherlands.
- Beaudoin, J.J. (1999), "Understanding the Microstructure of Concrete: Why Engineers Need Materials Science," Concrete International, August, pp. 86-89.
- Borja, R.I. (1991), "One-Step and Linear Multistep Methods for Nonlinear Consolidation," Computer Methods in Applied Mechanics and Engineering, Vol. 85, pp. 239-272.
- Burdine, N.T. (1953), "Relative Permeability Calculations from Pore-Size Distribution Data," Petroleum Transactions, AIME, Vol. 198, pp. 71-77.

- Burg, R.G. and Ost, B.W. (1994), *Engineering Properties of Commercially Available High Strength Concretes*, PCA Research and Development Bulletin RD104T, Skokie, IL.
- Butler, J.E. (1981), "The Influence of Pore Pressure upon Concrete," *Magazine of Concrete Research*, Vol. 33, No. 114, pp. 3-17.
- Cabrera, J.G. and Ghoddoussi, P. (1994), "The Influence of Fly Ash on the Resistivity and Rate of Corrosion of Reinforced Concrete," ACI SP-145, *Durability of Concrete*, edited by V.M. Malhorta, American Concrete Institute, Detroit, pp. 229-244.
- Castillo, C. and Durrani, A.J. (1999), "Effect of Transient High Temperature on High-Strength Concrete," *ACI Materials Journal*, Vol. 87, No. 1, pp. 47-53.
- Chan, S.Y.N., Peng, G.F., and Anson, M. (1999), "Fire Behavior of High-Performance Concrete Made with Silica Fume at Various Moisture Contents," *ACI Materials Journal*, Vol. 96, No. 3, pp. 405-409.
- Chana, P. and Price B. (2003), "The Cardington Fire Test," *Concrete*, January, pp. 28-33.
- Chung, J.H. and Consolazio, G.R. (2003), "Moisture Movement and Heat Flow in Reinforced Concrete Columns Subjected to Fire," *Proceedings of the Second MIT Conference on Computational Fluid and Solid Mechanics*, Boston, MA, Vol. 2, pp. 1287-1292.
- Chung, J.H. and Consolazio, G.R. (2004), "Finite Element Prediction of Spalling of High-Strength Concrete Structures Subjected to a Hydrocarbon Pool Fire," *The 2004 Structures Congress & Exposition—Building on the Past, Securing the Future*, Structural Engineering Institute, ASCE, Nashville, TN.
- Consolazio, G.R., McVay, M.C., and Rish, J.W. III. (1998), "Measurement and Prediction of Pore Pressures in Saturated Cement Mortar Subjected to Radiant Heating," *ACI Materials Journal*, Vol. 95, No. 5, pp. 525-536.
- Cook R.D., Malkus, D.S., and Plesha, M.E. (1989), *Concepts and Applications of Finite Element Analysis* (3rd ed.), John Wiley & Sons, Inc., New York, NY.
- Corey, A.T., Rathjens, C.H., Henderson, J.H., and Wyllie, M.R.J. (1956), "Three Phase Relative Permeability," *Petroleum Transactions, AIME*, Vol. 207, pp. 349-351.
- Dayan, A. and Gluekler, E.L. (1982), "Heat and Mass Transfer Within an Intensively Heated Concrete Slab," *International Journal of Heat & Mass Transfer*, Vol. 25, No. 10, pp. 1461-1467.
- Dhir, R.K., Hewlett, P.C., and Chan, Y.N. (1989), "Near Surface Characteristics of Concrete: Intrinsic Permeability," *Magazine of Concrete Research*, Vol. 41, No. 147, pp. 87-97.

- Elvery, R.H., Cox, A.T., and Butler, J.E. (1973), "Development of Apparatus to Investigate the Influence of Pore Pressure upon the Tensile Behavior of Concrete," *Magazine of Concrete Research*, Vol. 25, No. 85, pp. 231-237.
- Gagne, R., Boisvert, A., and Pigeon, M. (1996), "Effect of Superplasticizer Dosage on Mechanical Properties, Permeability, and Freeze-Thaw Durability of High Strength Concretes With and Without Silica Fume," *ACI Materials Journal*, Vol. 93, No. 2, pp. 111 fig. 7.
- Gawin, D., Majorana, C.E., and Schrefler, B.A. (1999), "Numerical Analysis of Hygro-Thermal Behavior and Damage of Concrete at High Temperature," *Mechanics of Cohesive-Frictional Materials*, Vol. 4, pp. 37-74.
- Hansen, K.K. (1989), "Sorption Isotherms: A Catalog and a Data Base," ASTM STP 1039, *Water Vapor Transmission Through Building Materials and Systems*, American Society for Testing and Materials, West Conshohocken, PA, pp. 28-32.
- Harmathy, T.Z. (1964), "Effect of Moisture on The Fire Endurance of Building Elements," ASTM STP 385, *Moisture in Materials in Relation to Fire Tests*, American Society for Testing and Materials, Chicago, IL, pp. 74-95.
- Hope, B.B. and Malhotra, V.M. (1984), "The Measurement of Concrete Permeability," *Canadian Journal of Civil Engineering*, Vol. 2, No. 3, pp. 287-292.
- Hsu, T. (1986), *The Finite Element Method of Thermomechanics*, Allen & Unwin, inc., London, UK.
- Huang, C.L.D. (1979), "Multi-phase Moisture Transfer in Porous Media Subjected to Temperature Gradient," *International Journal of Heat and Mass Transfer*, Vol. 22, pp. 1295-1307.
- Huang, C.L.D., Siang, H.H., and Best, C.H. (1979), "Heat and Moisture Transfer in Concrete Slabs," *International Journal of Heat and Mass Transfer*, Vol. 22, pp. 257-266.
- Huang, H. and Usmani, A.S. (1994), *Finite Element Analysis for Heat Transfer*, Springer-Verlag London, UK.
- Hudson, J.B. (1996), *Thermodynamics of Materials*, John Wiley & Sons, Inc., New York, NY.
- Hurst, J.P. and Ahmed, G.N. (1998), "Validation and Application of a Computer Model for Predicting the Thermal Response of Concrete Slabs Subjected to Fire," *ACI Structural Journal*, Vol. 95, No. 5, pp. 480-487.
- Jacobs, F. (1998), "Permeability to Gas of Partially Saturated Concrete," *Magazine of Concrete Research*, Vol. 50, No. 2, pp. 115-121.

- Janotka, I. and Bágel, L. (2002), "Pore Structures, Permeabilities, and Compressive Strengths of Concrete at Temperatures up to 800 °C," *ACI Materials Journal*, Vol. 99, No. 2, pp. 196-200.
- Ju, J.W. and Zhang, Y. (1998), "Axisymmetric Thermomechanical Constitutive and Damage Modeling for Airfield Concrete Pavement Under Transient High Temperature," *Mechanics of Materials*, Vol. 29, pp. 307-323.
- Kalifa, P., Menneteau, F.D., and Quenard, D. (2000), "Spalling and Pore Pressure in HPC at High Temperature," *Cement and Concrete Research*, Vol. 30, pp. 1915-1927.
- Kjellsen, K.O. and Atlasi, E.H. (1999), "Pore Structure of Cement Silica Fume Systems: Presence of Hollow-Shell Pores," *Cement and Concrete Research*, Vol. 29, pp. 133-142.
- Kodres, C.A. (1996), "Moisture Induced Pressures in Concrete Airfield Pavements," *Journal of Materials in Civil Engineering*, Vol. 8, No. 1, pp. 41-50.
- Kodur, V.K.R. (1997), "Studies on the Fire Resistance of High-Strength Concrete at the National Research Council of Canada," *International Workshop on Fire Performance of High-Strength Concrete*, NIST Special Publication 919, National Institute of Standards and Technology, Gaithersburg, MD, pp. 75-86.
- Kodur, V.K.R. (1999), "Fire Performance of High-Strength Concrete Structural Members," *Construction Technology Update* No. 31, National Research Council of Canada.
- Klinkenberg, L.J. (1941), "The Permeability of Porous Media to Liquids and Gases," *Drilling and Production Practice*, American Petroleum Institute, pp. 200-207.
- Lenhard, R.J. and Parker, J.C. (1987), "A Model for Hysteretic Constitutive Relations Governing Multiphase Flow 2. Permeability-Saturation Relations," *Water Resources Research*, Vol. 12, No. 2, pp. 2197-2206.
- Lewis, R.W. and Schrefler, B.A. (2000), *The Finite Element Method in the Static and Dynamic Deformation and Consolidation of Porous Media*, John Wiley & Sons, Inc., New York, NY.
- Li, K. and Horne, R.N. (2001), "Gas Slippage in Two-Phase Flow and the Effect of Temperature," SPE 68778, Society of Petroleum Engineers, presented at the 2001 SPE Western Region Meeting, Bakersfield, CA.
- Lie, T.T and Kodur, V.K.R. (1996), "Thermal and Mechanical Properties of Steel-Fibre-Reinforced Concrete at Elevated Temperatures," *Canadian Journal of Civil Engineering*, Vol. 23, No. 2, pp. 511-517.
- Loughborough, M.T. (1966), "Permeability of Concrete to Air," *Ontario Hydro Research Quarterly*, First Quarter, pp. 14-16.

- Luikov, A.V. (1966), *Heat and Mass Transfer in Capillary Porous Bodies*, Pergamon Press, Inc., Long Island City, NY.
- Malvern, L.E. (1969), *Introduction to the Mechanics of a Continuous Medium*, Prentice-Hall, Inc., Englewood Cliffs, NJ.
- McVay, M.C. and Geotechnical Numerical Group. (1998), *PLASFEM Version 2.4 Manual*, Department of Civil and Coastal Engineering, University of Florida, Gainesville, FL.
- McVay, M.C. and Rish, J.W. III. (1995), "Flow of Nitrogen and Superheated Steam Through Cement Mortar," *Journal of ThermoPhysics and Heat Transfer*, Vol. 9, No. 4, pp. 790-792.
- Moyne, C., Didierjean, S., Amaral Souto, H.P., and da Silveira, O.T. (2000), "Thermal Dispersion in Porous Media: One Equation Model," *International Journal of Heat and Mass Transfer*, Vol. 43, pp. 3853-3867.
- Nagataki, S., Ujike, I. and Konishi, N. (1986), "Influence of Moisture Content on Air Permeability of Concrete," *Review of 40 Meeting of Cement Association of Japan*, Tokyo, pp. 158-161.
- Narasimhan, T.N. and Witherspoon, P.A. (1976), "An Integrated Finite Difference Method for Analyzing Fluid Flow in Porous Media," *Water Resources Research*, Vol. 12, No. 1, pp. 57-64.
- Ojalvo, I.U. (1974), "Improved Thermal Stress Determination by Finite Element Methods," *AIAA Journal*, Vol. 12, No. 8, pp. 1131-1132.
- Parker, J.C., Lenhard, R.J., and Kuppusamy, T. (1987), "A Parametric Model for Constitutive Properties Governing Multiphase Flow in Porous Media," *Water Resources Research*, Vol. 23, No. 4, pp. 618-624.
- Patankar, S.V. (1980), *Numerical Heat Transfer and Fluid Flow*, Taylor & Francis, Inc., New York, NY.
- Phan, L.T. and Carino, N.J. (1998), "Review of Mechanical Properties of HSC at Elevated Temperature," *Journal of Materials in Civil Engineering*, Vol. 10, No. 1, pp. 58-64.
- Phan, L.T. and Carino, N.J. (2000), "Fire Performance of High Strength Concrete Research Needs," *Advanced Technology in Structural Engineering, ASCE/SEI Structures Congress 2000 Proceedings*, Philadelphia, PA.
- Phan, L.T., Lawson, J.R., and Davis, F.L. (2001), "Effects of Elevated Temperature Exposure on Heating Characteristics, Spalling, and Residual Properties of High Performance Concrete," *Materials and Structures*, Vol. 34, pp. 83-91.



- Phan, L.T. and Carino, N.J. (2002), "Effects of Test Conditions and Mixture Proportions on Behavior of High-Strength Concrete Exposed to High Temperatures," *ACI Materials Journal*, Vol. 99, No. 1, pp. 54-66.
- Pitt, J. and Hartl, H. (1980), "Improved Stress Evaluation under Thermal Load for Simple Finite Elements," *International Journal for Numerical Methods in Engineering*, Vol. 15, pp. 1507-1515.
- Preuss, K., Calore, C., Celati, R., and Wu, Y.S. (1987), "An Analytical Solution for Heat Transfer at a Boiling Front Moving Through a Porous Medium," *International Journal of Heat and Mass Transfer*, Vol. 30, No. 12, pp. 2595-2602.
- Preuss, K., Wang, J.S.Y., and Tsang, Y.W. (1990), "On Thermohydrologic Conditions Near High-Level Nuclear Wastes Emplaced in Partially Saturated Fractured Tuff; 1. Simulation Studies with Explicit Consideration of Fracture Effects," *Water Resources Research*, Vol. 26, No. 6, pp. 1235-1248.
- Pruess, K. (1991), *TOUGH2: A General-Purpose Numerical Simulator for Multiphase Fluid and Heat Flow*, Document LBL-29400, Earth Sciences Division, Lawrence Berkeley Laboratory, University of California, Berkeley, CA.
- Reinhardt, H.W. and Dinku, A. (1996), "Effects of Curing on the Gas Permeability of Cover Concrete," *NATO ASI Series*, Vol. 304, *The Modeling of Microstructure and Its Potential for Studying Transport Properties and Durability*, edited by H. Jennings, J. Kropp and K. Scrivener, Kluwer Academic Publishers, Boston, MA, pp. 325-337.
- Reis, M.B.C., Neves, C.I., Tadeu, A.J.B., and Rodrigues, J.P.C. (2001), "High-Temperature Compressive Strength of Steel Fiber High-Strength Concrete," *Journal of Materials in Civil Engineering*, Vol. 13, No. 3, pp. 230-234.
- Sahota, M.S. and Pagni, P.J. (1979), "Heat and Mass Transfer in Porous Media Subject to Fires," *International Journal of Heat and Mass Transfer*, Vol. 22, pp. 1069-1081.
- Samaha, H.R. and Hover, K.C. (1992), "Influence of Microcracking on the Mass Transport Properties of Concrete," *ACI Materials Journal*, Vol. 89, No. 4, pp. 416-424.
- Sanjayan, G. and Stocks, L.G. (1993), "Spalling of High-Strength Silica Fume Concrete in Fire," *ACI Materials Journal*, Vol. 90, No. 2, pp. 170-173.
- Scanlon, J.M. and McDonald, J.E. (1994), "Thermal Properties," *Significance of Tests and Properties of Concrete and Concrete-Making Materials*, ASTM STP 169C, American Society for Testing and Materials, Philadelphia, PA, pp. 233.
- Sugiyama, T., Bremner, T.W. and Holm, T.A. (1996), "Effect of Stress on Gas Permeability in Concrete," *ACI Materials Journal*, Vol. 93, No. 5, pp. 443-450.

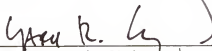
- Sullivan, P.J.E. (2001), *Deterioration and Spalling of High Strength Concrete under Fire*, Sullivan & Associates, Rickmansworth, UK.
- Tenchev, R.T., Li, L.Y., Purkiss, J.A., and Khalafallah, B.H. (2001), "Finite Element Analysis of Coupled Heat and Mass Transfer When It Is in Fire," *Magazine of Concrete Research*, Vol. 53, No. 2, pp. 117-125.
- Timoshenko, S.P. and Goodier, J.N. (1970), *Theory of Elasticity* (3rd ed.), McGraw-Hill, Inc., New York, NY.
- Ulm, F.J, Acker, P., and Levy, M. (1999a), "The "Chunnel" Fire. II: Analysis of Concrete Damage," *Journal of Engineering Mechanics*, Vol. 125, No. 3, pp. 283-289.
- Ulm, F.J, Coussy, O., and Bazant Z.P. (1999b), "The "Chunnel" Fire. I: Chemoplastic Softening in Rapidly Heated Concrete," *Journal of Engineering Mechanics*, Vol. 125, No. 3, pp. 272-282.
- Usmani, A.S., Rotter, J.M., Lamont, S., Sanad, A.M., and Gillie, M. (2001), "Fundamental Principles of Structural Behavior Under Thermal Effects," *Fire Safety Journal*, Vol. 36, pp. 721-744.
- Wang, B.X. and Yu, W.P. (1988), "A Method for Evaluation of Heat and Mass Transport Properties of Moist Porous Media," *International Journal of Heat and Mass Transfer*, Vol. 31, pp. 1005-1009.
- Whiting, D. (1988), "Permeability of Selected Concrete," *Permeability of Concrete*, ACI SP-108, edited by D. Whiting and A. Walitt, American Concrete Institute, pp. 195-222.
- Ymazaki, N., Yamazaki, M., Mochida, T., Mutoh, A., Miyashita T., Ueda, M., Hasegawa, T., Sugiyama, K., Hirakawa, K., Kikuchi, R., Hiramoto, M., and Saito, K. (1995), "Structural Behavior of Reinforced Concrete Structures at High Temperatures," *Nuclear Engineering and Design*, Vol. 156, pp. 121-138.
- Zhang, M.H. and Gjorv, O.E. (1991), "Permeability of High Strength Lightweight Concrete," *ACI Materials Journal*, Vol. 88, No. 5, pp. 463-469.

## BIOGRAPHICAL SKETCH


The author was born and raised in Korea. In 1992, he came to the United States in order to broaden his education in engineering. Two years after attending the English as a Second Language Program at Marymount Manhattan College, he was admitted to the graduate school of Rutgers University at New Brunswick, NJ. In 1998, after obtaining the Master of Science degree in civil and environmental engineering from Rutgers University, he had the opportunity to pursue the degree of Doctor of Philosophy in civil and coastal engineering at the University of Florida. This has been an extraordinary learning, teaching and research experience. The author's career goal is excellence in teaching and research, and he is looking forward to pursuing a career in the engineering research field.

At the University of Florida, he has also actively participated in extracurricular activities. He was a representative of the Department of Civil and Coastal Engineering on the Graduate Student Council during the academic years of 1999 through 2000. He also founded the first university Kendo club in Florida at the University of Florida in 2000 and has been the instructor of the club since then.


I certify that I have read this study and that in my opinion it conforms to acceptable standards of scholarly presentation and is fully adequate, in scope and quality, as a dissertation for the degree of Doctor of Philosophy.

  
\_\_\_\_\_  
Gary R. Consolazio, Chairman  
Assistant Professor of Civil and Coastal  
Engineering

I certify that I have read this study and that in my opinion it conforms to acceptable standards of scholarly presentation and is fully adequate, in scope and quality, as a dissertation for the degree of Doctor of Philosophy.

  
\_\_\_\_\_  
Kurtis R. Gurley, Cochairman  
Associate Professor of Civil and Coastal  
Engineering


I certify that I have read this study and that in my opinion it conforms to acceptable standards of scholarly presentation and is fully adequate, in scope and quality, as a dissertation for the degree of Doctor of Philosophy.

  
\_\_\_\_\_  
Michael C. McVay  
Professor of Civil and Coastal Engineering

I certify that I have read this study and that in my opinion it conforms to acceptable standards of scholarly presentation and is fully adequate, in scope and quality, as a dissertation for the degree of Doctor of Philosophy.

  
\_\_\_\_\_  
Marc Hoyt  
Professor of Civil and Coastal Engineering

I certify that I have read this study and that in my opinion it conforms to acceptable standards of scholarly presentation and is fully adequate, in scope and quality, as a dissertation for the degree of Doctor of Philosophy.



---

Loc Vu-Quoc  
Professor of Mechanical and Aerospace  
Engineering

This dissertation was submitted to the Graduate Faculty of the College of Engineering and to the Graduate School and was accepted as partial fulfillment of the requirements for the degree of Doctor of Philosophy.

August, 2003



---

Pramod P. Khargonekar  
Dean, College of Engineering

---

Winfred M. Phillips  
Dean, Graduate School